



TECHNISCHE
UNIVERSITÄT
WIEN
Vienna | Austria

Master's thesis

**Surface morphology and catalyst characterization of
bed material in dual fluidized bed biomass gasification**

carried out for the purpose of obtaining the academic degree Diplomingenieur (MSc.)
under supervision of

Univ.Prof. Dipl.-Ing. Dr.techn. Hermann Hofbauer
and
Univ.Lektor DI Dr. Matthias Kuba

Institut für Verfahrenstechnik, Umwelttechnik und techn. Biowissenschaften
E166

and co-supervision of

Prof. Dr.hab. Joanna Lojeweska
Jagiellonian University, Kraków, Poland

submitted to Technische Universität Wien

Fakultät für Technische Chemie

by

Daniel Eugen Janisch, BSc
Matr.Nr.: 01225848
Reindorfgasse 8/7
1150 Wien

Affidavit

I, Daniel E. Janisch, hereby declare

1. that I am the sole author of the present Master's thesis, "Surface morphology and catalyst characterization of bed material in dual-fluidized-bed biomass steam gasification " and that I have not used any source or tool other than those referenced or any other illicit aid or tool.
2. that I have not prior to this date submitted this Master's thesis as an examination paper in any form in Austria or abroad.
3. that the publication of this thesis needs the confirmation of the examination committee.

Vienna, July 22, 2019

Daniel E. Janisch

Abstract

Gasification of biomass provides a gas with comparably high calorific value out of renewable energy sources. The product gas can be used to produce electricity, heat or can be further processed into industrial chemicals. However, a variety of challenges are faced in particular by gasification of non-wood biomass. Most notably, undesired tars in the product gas may cause clogging and fouling of the heat exchanger pipes are currently washed out by solvent scrubbers. The employed biogenic scrubber liquid is burnt after utilization and thus increases significantly operative costs. Bed material grains in fluidized bed reactors are responsible for heat transfer and dispersion of incoming fuel. These were found to collect ash, forming layers during gasification. The formed ash layer then improves the product gas quality in terms of lower tar contents and higher concentrations of desired hydrogen gas. The ash layer composition depends on the employed fuel and its thickness primarily on the reactor residence time of the grains.

Olivine and Feldspar bed materials were studied before and after gasification processes with logging residues and chicken manure. The surface area of the grains assessed with the BET method was found to be increased after gasification. The elemental composition was measured by both bulk and surface sensitive methods indicating high calcium contents in the ash layer. Employed phase analysis measurements further offer indications about the chemical nature and suggest calcium oxide prevails as one of the main components in the ash layer. The adsorption of probe molecules on pure calcium oxide and ash layered Olivine disclose insights on the nature of catalytically active sites on the ash layer surface, providing first conclusions on the mechanism of the Water-Gas-Shift reaction.

Kurzfassung

Die Dampf-Vergasung von Biomasse liefert ein vergleichbar hochkalorisches Gas aus regenerativen Energiequellen. Das erzeugte Produktgas kann sowohl zur Strom- und Wärmeerzeugung als auch für die Herstellung wertvoller Treibstoffe und Chemikalien verwendet werden. Indessen stellt die Vergasung insbesondere von nicht-holzbasierter Biomasse den Prozess vor Herausforderungen. Teere im Produktgas sind besonders problematisch zumal diese in Wärmetauscherrohren kondensieren und ein Blockieren der Leitungen verursachen können. Die Gasreinigung stellt einen signifikanten Teil der Betriebskosten dar, da eingesetzte biogene Waschflüssigkeit nicht regeneriert werden kann und im Prozess verbrannt wird. Die Bettmaterialkörner, die in einem Wirbelschichtreaktor für Wärmeübertragung und Durchmischung verantwortlich sind, bauen während dem Betrieb Ascheschichten auf. Diese gebildeten Ascheschichten sind vorteilhaft für die Produktgasqualität, die Teeranteile verringern und erwünschte Wasserstoffkonzentrationen erhöhen. Die Zusammensetzung dieser Ascheschicht ist abhängig von dem eingesetzten Brennstoff und ihre Dicke korreliert mit der Verweilzeit im Reaktor.

Olivin und Feldspat Bettmaterialien wurden vor und nach einem Umsatz, mit Brennstoffmischungen aus Rinde und Hühnermist, im Wirbelschichtreaktor untersucht. Die Oberfläche der Körner wurde per BET Methode vermessen und zeigt eine vergrößerte Oberfläche der Körner mit Ascheschicht. Die elementare Zusammensetzung wurde sowohl mittels oberflächensensitiven als auch Partikel-durchdringenden Verfahren analysiert wobei Hinweise auf hohe Calciumkonzentrationen in der Ascheschicht gefunden wurden. Weitere eingesetzte Methoden liefern Informationen über die chemische Natur der vorkommenden Elemente, dabei deuten die Ergebnisse darauf hin, dass Calciumoxid als häufigste Verbindung in der Ascheschicht vorliegt. Beobachtete Adsorptionen von Molekülen an der Oberfläche einer Modellsubstanz und einem benutzten Bettmaterial offenbaren erste Hinweise auf die aktiven Zentren auf der Ascheschicht und den Mechanismus der Wasser-Gas-Shift Reaktion.

Résumé

La gazéification de la biomasse fournit un gaz à haute teneur calorifique à partir de sources d'énergie renouvelables. Le produit gazeux peut être utilisé pour produire de l'électricité, de la chaleur ou être transformé en produits chimiques industriels. Cependant, la gazéification de la biomasse non ligneuse est confrontée à de nombreux défis. En particulier, les goudrons indésirables contenus dans le gaz produit peuvent provoquer l'encrassement des tuyaux de l'échangeur de chaleur qui sont actuellement filtrés par des épurateurs de gaz. Le liquide de lavage biogénique employé est brûlé après l'usage et augmente considérablement les coûts de production. Les grains de matière des lits dans les réacteurs à lit fluidisé, qui sont responsables du transfert de chaleur et de la dispersion du combustible entrant, accumulent des couches de cendres pendant la gazéification. La couche de cendres formée améliore la qualité du gaz produit en termes de teneur plus faible en goudron et de concentrations plus élevées en hydrogène souhaité.

Les matériaux des lits d'olivine et de feldspath ont été étudiés avant et après les processus de gazéification avec les déchets des bois et le fumier de volaille. La surface spécifique des grains a été évaluée par la méthode BET et sa composition chimique a été mesurée par des méthodes sensibles à la surface. L'analyse des phases offre en outre des indications sur la nature chimique des éléments détectés dans la couche de cendres. L'adsorption de molécules sondes sur un composé modèle et Olivine utilisé révèle des informations sur la nature des sites catalytiquement actifs situés à la surface de la couche de cendres et fournit des premières conclusions sur le mécanisme de la réaction du gaz à l'eau sur les grains de matériau du lit.

Resumen

La gasificación por vapor de la biomasa proporciona un gas en alto valor calorífico de fuentes de energía renovables. Este gas se puede utilizar para producir electricidad, calor o se puede procesar en productos químicos industriales. Sin embargo, la gasificación de biomasa no maderera enfrenta una variedad de desafíos. En particular, los alquitranes no deseados en el gas pueden causar obstrucciones y ensuciamiento de las tuberías del intercambiador de calor. Los alquitranes son actualmente lavados por los depuradores de solventes. El líquido depurador biogénico se quema después de la utilización y aumenta significativamente los costos de producción. Se encontró que los granos de material del lecho en reactores de lecho fluidizado, que son responsables de la transferencia de calor y la dispersión del combustible, acumulan capas de ceniza durante la gasificación. La capa de ceniza formada mejora la calidad del gas en términos de menores contenidos de alquitrán y mayores concentraciones de gas de hidrógeno. La composición de la capa de ceniza depende del combustible y su espesor principalmente del tiempo de los granos en el reactor.

Los materiales de lecho de olivino y feldespato fueron estudiados antes y después de los procesos de gasificación con serrín y estiércol de gallina. El área de superficie de los granos se evaluó mediante el método BET, y la composición elemental se midió mediante métodos sensibles a la superficie. Además las mediciones de análisis de fase ofrecen indicaciones sobre la naturaleza química de los elementos detectados en la capa de ceniza. La adsorción de moléculas de sonda en un compuesto modelo y olivino usado revela información sobre la naturaleza de los sitios catalíticamente activos en la superficie de la capa de ceniza y proporciona primeras conclusiones sobre el mecanismo de la reacción de cambio de agua-gas en los granos de material del lecho.

Acknowledgments

First of all, I would like to thank Dr. Matthias Kuba to entrust me with this challenging but very exciting project. He was always exceptionally supporting and trusted me to explore my own ideas. Furthermore, he paved the way for an exciting 5 week research stay at the Jagiellonian University in Krakow, Poland. The project was realized in the research group of Bioenergy2020+ and I thank all the team members for the warm welcome, especially Katharina and Christoph who resolved numerous questions. I also thank Kouessan for brightening up intensive days of work in the laboratory and the fun moments together Krakow.

Further, I would like to thank Prof. Hofbauer for the supervision of the project. I thank both Prof. Hofbauer and Prof. Winter for the recommendation letters for a travel stipend to Poland.

Prof. Joanna Łoweska welcomed us into her research group in Krakow and I am deeply grateful for the effort and time she invested in us. I thank Dominika who helped us with measurements and experiments on a daily bases. Special thanks to Damian who went out of his way to help, not only with the experimental setup but also with the interpretation of collected data.

Moreover, Prof. Föttinger made supplemental measurements in Vienna possible and I would like to extend my gratitude to her and her team members, in particular to Gernot and Nevzat who supported me with the experiments. I also would like to thank Prof. Friedbacher and Elisabeth Eitenberger for the supervision of SEM analysis.

Special thanks also to Natalie for the thorough proofreading and to my friends abroad Andrés and Nassim who revised the spanish and french abstract.

It is doubtful whether I would have made it to the finish line without my fellow students Julian, Tobias, Joseph, Birgit, Sophia, Thomas, Anna and Charlie who became close friends during the last years. Thank you Michael for the inspirational friendship and the numerous adventures in the scientific and the real world.

I am also very grateful for the support of all my other friends who appreciate me for who I am. Thank you Antonia for standing always by my side and believing in me.

My deepest gratitude goes to my sister Sophie and my parents Eva and Christian who made sure I could lead the life I wanted and to whom I dedicate this work.

Danksagung

Zunächst möchte ich Dr. Matthias Kuba für die Möglichkeit danken diese fordernde aber sehr spannende Arbeit unter seiner Betreuung schreiben zu dürfen. Er war immer sehr bemüht und ließ mir die Freiheit auch meine eigenen Ideen zu verfolgen. Ohne seine Unterstützung wäre ein anregender Forschungsaufenthalt von fünf Wochen an der Jagiellonian University in Krakau, Polen nicht zustande gekommen. Die Arbeit wurde verwirklicht in der Forschungsgruppe Bioenergy 2020+ und ich möchte dem ganzen Team für die freundliche Aufnahme danken, insbesondere Katharina und Christoph, die so manche technische Fragezeichen auflösten. Ein großes Dankeschön an Kouessan für das Aufheitern intensiver Arbeitstage im Forschungslabor und all die spaßigen Momente in Krakau.

Weiters möchte ich Prof. Hofbauer für die erstklassige Betreuung danken sowie für das Verfassen von Empfehlungsschreiben für das Reisestipendium gemeinsam mit Prof. Winter.

Prof. Joanna Łoweska nahm uns in ihre Forschungsgruppe in Krakau auf und ich bin sehr dankbar für das Bemühen und die Zeit, die sie in uns investiert hat. Ich danke auch Dominika, die uns in alltäglichen Messversuchen unterstützt hat. Besonderen Dank auch an Damian, der keine Mühen gescheut hat uns, nicht nur im Aufbau der Experimente sondern auch bei der Auswertung der Daten geholfen hat.

Mein Dank gilt ebenfalls Prof. Föttinger und ihrem Forschungsteam, wo ich ergänzende Messungen in Wien realisieren durfte. Besonderen Dank an Gernot und Nevzat, die viele Fragen beantwortet haben und mich bei der Durchführung der Experimente unterstützt haben. Danke auch an Prof. Friedbacher und Elisabeth Eitenberger für die Betreuung während der REM Analyse.

Ein besonderes Dankeschön an Natalie für das Korrektorat der Arbeit, sowie an meine Freunde im Ausland Andres und Nassim für Korrektur der Kurzfassungen in Spanisch und Französisch.

Ohne meine Studienkollgen Julian, Tobias, Joseph, Birgit, Sophia, Thomas, Anna and Charlie wäre es vermutlich nicht zu einem positiven Studienabschluss gekommen und freue mich über die gewonnen Freundschaften. Danke Michael für die inspirierende Freundschaft und die Vielzahl an durchstandenen Abenteuer.

Ich danke auch allen Freunden und Verwandten für unzählige Zusprüche und Unterstützung. Vielen Dank Antonia, dass du immer an meiner Seite stehst und an mich glaubst.

Meine größte Dankbarkeit gilt meiner Schwester Sophie und meinen Eltern Eva und Christian, die mir meinen bisherigen Lebensweg ermöglichten und denen ich diese Arbeit widme.

Contents

1	Introduction	1
1.1	Aim	2
2	Theoretical fundamentals	3
2.1	Gasification principle	3
2.1.1	Chemical reactions during gasification	4
2.2	Design of industrial gasifiers	8
2.2.1	Dual fluidized bed reactors	9
2.2.2	Notable industrial operations	9
2.3	Challenges and motivation	12
2.4	Catalysts for biomass gasification	14
2.4.1	Beginnings and development	14
2.4.2	Principles of heterogeneous catalysis	17
2.5	Catalyst characterization	18
2.5.1	Colorimetry	18
2.5.2	Scanning electron microscopy (SEM)	19
2.5.3	Energy dispersive x-ray spectroscopy (EDXS)	19
2.5.4	Assessment of surface area (BET method)	21
2.5.5	Energy dispersive x-ray fluorescence (EDXRF)	23
2.5.6	X-ray diffraction (XRD)	24
2.5.7	X-ray photoelectron spectroscopy (XPS)	25
2.5.8	Fourier-transform infrared spectroscopy (FT-IR)	27
2.5.9	Raman spectroscopy	30
2.5.10	Method comparison	33
3	Materials and methods	34
3.1	Studied bed material	34
3.1.1	Olivine	34
3.1.2	K-Feldspar	35
3.2	Analytical equipment	36
4	Research findings	39
4.1	Surface Morphology	39
4.1.1	Colorimetry	39
4.1.2	BET surface area	40
4.1.3	SEM imaging	41
4.2	Bed material composition	46
4.2.1	Surface properties: XPS and EDX	46

4.2.2	Bulk properties: XRD and XRF	50
4.2.3	Chemical structure: Raman spectroscopy	52
4.2.4	Chemical structure: FT-IR spectroscopy	55
4.3	Adsorption of probe molecules	58
4.3.1	Methanol adsorption	58
4.3.2	Acetic acid adsorption	60
4.3.3	Carbon monoxide adsorption	61
5	Discussion of results	63
6	Conclusion and outlook	69
	Nomenclature	70
	Bibliography	76
	Appendix	76
7	Appendix	77

List of Figures

2.1	Prerequisites and conditions of thermochemical conversion processes [1] . . .	3
2.2	Potential paths of gasification [2]	4
2.3	Reaction equilibrium homogeneous WGS (left) heterogeneous WGS (right) [3]	5
2.4	Overview of main gasifier reactor types [4]	8
2.5	Power output of gasifier types [2]	8
2.6	DFB principle scheme (left) and simplified reactor layout (right) for biomass gasification developed at TU Vienna [5]	10
2.7	Flowsheet of the steam blown gasifier 8 MW CHP plant Güssing, Austria [6]	11
2.8	Backscattered SEM image of an Olivine used cross-section showing an ash layer of heavier elements [7]	15
2.9	Potential energy diagram of a gaseous reaction without catalyst that overcomes a substantial energy barrier contrasted to the same reaction with a solid catalyst [8]	17
2.10	CIE 1931 color space chromaticity diagram [9]	18
2.11	Electron interactions with matter (left) [10] and emission mechanisms (right) [11]	20
2.12	Classification of physisorption isotherms (IUPAC update 2015) [12]	22
2.13	Simplified scheme of the XRF principle based on the Bohr model of atoms [13]	24
2.14	Illustrations of x-ray scattering at an ordered lattice as a function of the angle 2θ [8]	25
2.15	Photoemission and the Auger process [8]	26
2.16	The infrared spectrum (wavenumbers in cm^{-1}) of CO in gas phase and adsorbed on an Ir/SiO_2 catalyst [8]	28
2.17	Infrared spectroscopy techniques, from left to right: transmission, attenuated total reflectance (ATR) and diffused reflectance (DR) [14]	29
2.18	Transitions between vibrational states of molecules involved in Raman and IR spectroscopy [15]	31
2.19	Vibrational modes of CO_2 , a triatomic linear molecule, and the corresponding IR/Raman activities in wavenumbers [16]	32
2.20	Visualization of analytical dimensions for principal microanalysis tools; the x-axis shows the electron or light spot size whereas the y-axis demonstrates the detection limit [17]	33
4.1	CIE 1931 color space chromaticity diagram with color points	39
4.2	SE image of Olivine fresh and surface close-up	42
4.3	SE image of Olivine used and surface close-up	42
4.4	SE image of Feldspar fresh and surface close-up	43
4.5	SE image of Feldspar CM8h and surface close-up	43

4.6	SE image of Feldspar B8h and surface close-up	44
4.7	SE image of Feldspar B32h and surface close-up	44
4.8	SE image of Feldspar Mix8h and surface close-up	45
4.9	SE image of Feldspar Mix40h and surface close-up	45
4.10	Elemental information derived by XPS measurements	46
4.11	XPS fitting for <i>Ca 2p</i> peaks of selected samples	47
4.12	Elemental information derived by EDX measurements	49
4.13	Elemental information derived by XRF measurements	50
4.14	Compilation of the XRD phase analysis	51
4.15	Raman spectra of Olivine samples	52
4.16	Raman spectra of Feldspar samples	53
4.17	Olivine used spectra obtained from ATR, DRIFTS, Transmission IR	55
4.18	Olivine fresh, Olivine used and Olivine used finely ground are compared to <i>CaO</i> and <i>MgO</i> (DRIFTS)	56
4.19	Changes in OU spectra after heating the sample up to 500°C in <i>O₂</i> atmosphere and afterwards heating up to 350°C in <i>H₂</i> atmosphere (Transmission IR)	57
4.20	Feldspar samples compared to <i>SiO₂</i> (DRIFTS)	57
4.21	MeOH adsorption on CaO (DRIFTS): (a) Subtraction result CaO after MeOH adsorption 40 °C, (b) 100 °C, (c) 200 °C, (d) 300 °C, (e) 400 °C, (f) 500 °C	58
4.22	HAc adsorption on CaO (DRIFTS): (a) Subtraction result CaO after HAc adsorption 40 °C, (b) 100 °C, (c) 200 °C, (d) 300 °C, (e) 400 °C, (f) 500 °C	60
4.23	<i>CO</i> adsorption on <i>CaO</i> (Transmission mode): (a) Subtraction result <i>CaO</i> during <i>CO</i> adsorption 500 mbar ambient temperature, (b) after <i>CO</i> adsorption vacuum a.t. , (c) 100°C, (d) 200°C, (e) 300°C, (f) 400°C	61
4.24	Monomeric <i>CO</i> chemisorbed on <i>CaO</i> as proposed by Garrone et. al. [18]	62
4.25	<i>CO</i> adsorption on Olivine used (Transmission mode): (a) Subtraction result OU during <i>CO</i> adsorption 10 mbar ambient temperature, (b) Subtraction result OU during <i>CO</i> adsorption 50 mbar a.t., (c) Subtraction result OU during <i>CO</i> adsorption 100 mbar a.t., (d) after adsorption and vacuum	62
5.1	Extrapolation of elemental composition derived by XRF, EDX and XPS results for selected elements (<i>Si, P, K, Ca, Fe</i>)	64
5.2	WGS mechanism over a high temperature catalyst: iron oxide [19]	67
5.3	WGS mechanism over a middle temperature catalyst: magnesium oxide [19]	68
7.17	Collected EDX spectra	90
7.18	Olivine XRD spectra including allocated compounds	90
7.19	Feldspar bark XRD spectra including allocated compounds	91
7.20	Feldspar chicken manure and mix XRD spectra including allocated compounds	91
7.21	Raman spectra of measured reference compounds <i>MgO, CaO</i> and <i>Fe₂O₃</i>	92
7.22	Structures of adsorbed Carbonate and Formate [20]	92

List of Abbreviations

ATR	Attenuated total reflexion
B32h	Bark 32 hours reactor residence time
B8h	Bark 8 hours reactor residence time
BET	Brunauer–Emmett–Teller
BJH	Barrett-Joyner-Halenda
BSE	Backscattered electrons
CIE	International Commission on Illumination (Commission internationale de l'éclairage)
CM8h	Chicken manure 8 hours reactor residence time
DFB	Dual fluidized bed
DRIFTS	Diffuse reflectance infrared fourier transform spectroscopy
EDX	Energy dispersive x-ray spectroscopy
FB	Fluidized bed
FF	Feldspar fresh
FT-IR	Fourier-transform infrared spectroscopy
Mix40h	Fuel mix (70 % bark 30 % chicken manure) 40 hours reactor residence time
Mix8h	Fuel mix (70 % bark 30 % chicken manure) 8 hours reactor residence time
OF	Olivine fresh
OU	Olivine used
SE	Secondary electrons
SEM	Scanning electron microscope
TEM	Transmission electron microscope
WG	Water-Gas reaction
WGS	Water-Gas-Shift reaction
XPS	X-ray photoelectron spectroscopy
XRD	X-ray diffraction
XRF	X-ray fluorescence spectroscopy

Introduction

The origins of gasification date back to the early 17th century when Flemish chemist Jan Baptista van Helmont recognized in his experiments, from heating wood and coal the existence of substances that are neither vapor nor air. He coined the term “gas”, derived from the ancient greek *khaos* or chaos and identified carbon dioxide as one of the formed substances [21]. At the dawn of the 18th century, following the investigations of Thomas Shirley on gas originating from coal reserves, Reverend John Clayton was the first to distill coal obtaining “coal gas”. The first patent for industrial gasification was then issued almost 50 years later by Robert Gardner in 1788 [2].

During its early stages, gasification was primarily used to produce coal gas comprising hydrogen, carbon monoxide, methane, other volatile carbohydrates and small amounts of non-calific gases such as carbon dioxide and nitrogen. The manufactured gas was pumped through elaborate pipe networks to illuminate town centers and large buildings. The dimensions of these coal gas productions are evidenced today by old, large gas storage tanks all over major cities. For instance, the main buildings of the well-known shopping mall and concert venue in Vienna, hence its name Gasometer, were originally designed as gas storage tanks. Coal was processed in a gasification plant in modern chamber furnaces and the annual gas production culminated in 166 million cubic meters in 1951 [22]. The outgassed coal was also of great interest to the steel industry as produced coke was one key ingredient as a reducing agent for smelting iron ore [23].

The advent of electric lightning around 1900 made manufactured gas gradually obsolete for the obvious health and safety advantages that came with it. Yet, the production of coal gas did not cease. The interesting gas composition soon resulted in other applications and further processing. Germany was the first nation to find an alternative to crude oil when Franz Fischer and Hans Tropsch invented in 1926 the process to convert coal gas into petroleum [24]. The today well-known Fischer-Tropsch (FT) synthesis process converts a gaseous reactant which includes carbon monoxide and hydrogen, commonly referred to as “synthesis gas” or “syngas”, into a number of hydrocarbon products, ranging from gaseous to waxy compounds and water.

However, the end of WWII and the availability of abundant oil from the Middle East eliminated the need for gasification eventually also for means of transportation and chemical production. Due to the lack of economic competitiveness industry gave up almost all FT processing entirely. It was not until the global energy crisis in 1973 that triggered new incentives for research towards alternative technologies and a revival of gasification. In a global quest for energy autonomy and sustainable fuels, gasification from renewable resources, such as wood and wastes constitutes a promising alternative to conventional fuels. With the right political incentives biomass gasification can provide raw materials to chemical production, renewable energy and fuel generation [2].

Since the revival of gasification as an alternative to fuel and chemical production in the late 70s, many new processes have been developed and are continuously improved. National governments as well as international organisations, e.g. the international energy agency (IEA), stride towards mineral oil independent energy production. The looming consequences of rising CO_2 levels in earth's atmosphere are affecting more and more people around the world who are demanding a change in energy production. As a less greenhouse gas intensive energy source compared to mineral oil, natural gas consumption is expected to double until 2040 becoming the first primary energy source before crude oil [25]. In spite of the expansion of gas infrastructure, natural deposits are limited. In contrast to natural gas, gasification of biomass allows for high-caloric gas production in a renewable way. The gasification process can be adapted to produce heat, electricity or transform the product gas into a wide range of industrial chemicals with CO_2 -neutral emissions.

Applicable biomass ranges from wood and logging residues to agricultural and municipal wastes. Animal manure and sewage sludge are increasingly interesting as forest derived biomass increases in price due to higher demands [26]. The biggest challenge when processing non-wood biomass are elevated contents of inorganic ash residues and its composition. Residual ash may cause agglomerations in the reactor impeding a proper process conduct. However, several studies have shown beneficial effects of ash in fluidized bed gasification reactors [27]. Ash deposits coat the bed material grains during operation resulting in ash layered bed material grains and better product gas qualities were measured when ash layered bed material was used.

1.1 Aim

A better understanding of catalytic processes and chemical reactions in gasification reactors is vital for a development of better and more feasible gasification. This work focuses on the surface characterization of the bed material employed in the Dual-fluidized-bed (DFB) biomass steam gasification reactor, developed at TU Wien. The iron magnesium silicate mineral Olivine was the first applied bed material that also demonstrated catalytic activity towards tar reduction and the Water-Gas-Shift reaction.

The increased catalytic activity of the bed material by formed ash layers on the mineral grains was first discovered by F. Kirnbauer in 2011 for Olivine [27]. An increase in catalytic activity was further shown for ash layered Feldspar bed material [28].

This work therefore aims for deeper insights in the morphology and the catalytic active sites on the ash layer that shall pave the way for improved process adjustments to maximise ash layer formation and consequently optimize producer gas quality. Thereto a thorough surface examination has been conducted on bed materials Olivine and Feldspar with and without ash deposits. Employed methods of analysis include: SEM microscopy, UV-VIS, EDX, XRF, XRD, XPS, FT-IR and Raman spectroscopy.

Theoretical fundamentals

2.1 Gasification principle

Gasification is a thermochemical conversion process where a solid or fluid energy source is transformed into high caloric gases compared to low caloric gases such as CO_2 or H_2O . During combustion, another thermochemical conversion process, fuel is broken down and forms by reaction with oxygen primarily CO_2 and H_2O . If sufficient quantities of oxygen are supplied, all reactants are fully oxidized and there is complete combustion. In gasification, full conversion of fuel into CO_2 and H_2O is intentionally inhibited. The partial oxidation is ensured by limiting or replacing oxygen with a gasification agent. Typical gasification agents comprise oxygen, air or steam [3].

Another key difference between combustion and gasification is the chemical nature of involved chemical reactions. While combustion is a self-sustaining process, gasification generally relies on external heat supply [3]. The molecular bonds within carbon dioxide and water are much more stable compared to the bonds in fuel and oxygen molecules, resulting in an energy difference that is compensated by the release of heat. Chemical reactions that release this energy difference to their surroundings in form of heat are called exothermic. In combustion, the released heat maintains the progress of the reaction. However, chemical reactions that consume more energy or heat from their surroundings than is released are called endothermic. Most reactions in gasification classify as endothermic and thus require external energy to proceed [29].

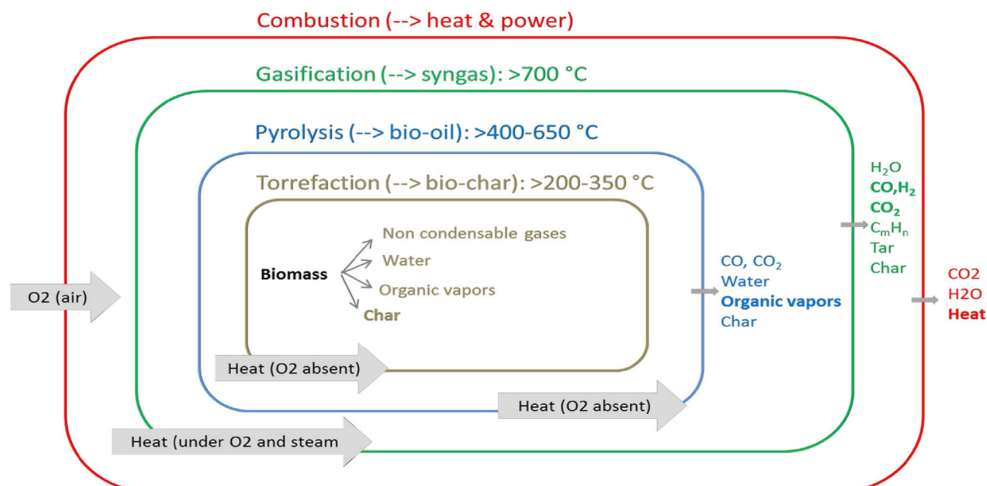


Figure 2.1: Prerequisites and conditions of thermochemical conversion processes [1]

Figure 2.1 illustrates thermal conversion processes by taking the example of biomass as fuel. When biomass is heated its humidity decreases while increasing in energy density. Approximately until temperatures of 200°C water evaporates through the porous structure in an endothermic process. As the temperature further increased with exclusion of oxygen larger organic molecules break down and significant amounts of CO_2 are detected. The formation of carbon dioxide is possible since oxygen is present i.a. in cellulose. These processes that break irreversibly chemical bonds just by means of heat in complete absence of oxygen are called pyrolysis. Torrefaction (fr. roasting) is considered a mild pyrolysis, carried out at lower temperatures. Between circa $280 - 500^{\circ}\text{C}$ under anaerobic conditions strongly exothermic reactions are observed. To form a picture of the order of magnitude, per kg wood around 880 kJ of heat is released enough to boil around $2,5 \text{ L}$ of ambient water. Inflammable gases such as CO , CH_4 , formaldehyde, acetic acid, methanol and hydrogen gas are formed. The gases evaporate quickly and carry along droplets of condensable organic compounds that appear as smoke. The residue of these gasification reactions is charcoal. Over 600°C gasification reactions then reach measurable reaction rates and become technologically exploitable over 700°C [2], [3]. A listing of the principal gasification reactions is given in section 2.1.2.

Consequently, the set temperature, applied pressure and gases fed to (or kept out of) the reactor result in one of the three main types of thermochemical conversion pyrolysis, gasification and combustion.

2.1.1 Chemical reactions during gasification

As aforementioned, biomass undergoes a series of physical and chemical reactions before and throughout gasification. Figure 2.2 lies out schematically observed phenomena and resulting products. Breaking down biomass generates directly gasses, liquids and solids that undergo a different set of reactions.

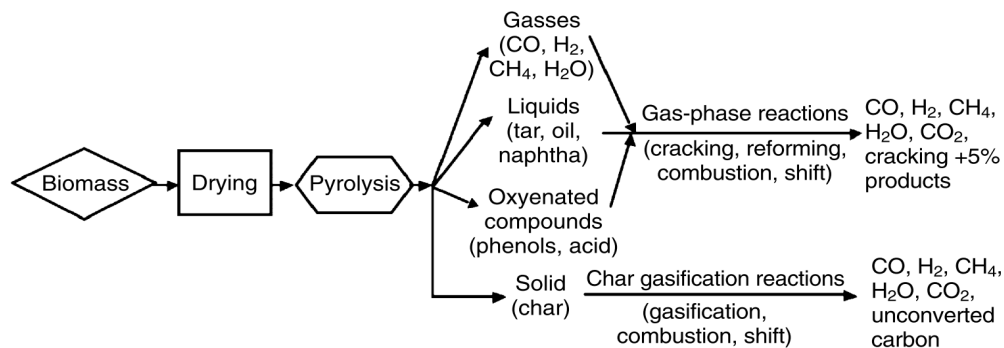


Figure 2.2: Potential paths of gasification [2]

Since oxygen is already present in the fuel compounds as bound in cellulose, carbon oxides and water can be formed already during pyrolysis. Depending on pressure ratios, temperature and concentration of gasifying agent i.a. following reactions 2.3 - 2.17 may occur. The reactions are given with their corresponding reaction enthalpy ΔH (where applicable) and indicates the interchanged amount of heat in an isobaric reaction. For endothermic reactions the reaction enthalpy ΔH is a positive value implying heat needs to be put into the system in order to initiate the reaction. In return, heat is released for exothermic reactions where ΔH is negative.

The following equation 2.1 of heating a solid A_s to produce a gas C_g and a solid residue B_s maps out the concept of reaction enthalpy.



In order to make statements if a reaction starts spontaneously under isobaric conditions another thermodynamic value is introduced, the free reaction enthalpy ΔG . It is not to be confused with the reaction enthalpy ΔH as ΔG includes also the reaction temperature and entailed entropy increase ΔS of the specific reaction.

$$\Delta G = \Delta H - T\Delta S \quad (2.2)$$

The chemical equilibrium is defined as $\Delta G = 0$ and as a result a chemical reaction is only possible to proceed when $\Delta G < 0$. If ΔG was greater zero than the reaction would proceed in counter direction. In practical terms this means that endothermic gasification reactions can only take place at high temperatures. The equilibrium curve ($\Delta G = 0$) is depicted in Figure 2.3 as a function of temperature. At any point distant to the equilibrium curve the system strives to get closer to an equilibrium. When starting at 700K and 100 % of reactants CO and H_2O in plot 2.3 the reaction will proceed until only 20 % of reactants CO and H_2O are left and 80 % of products CO_2 and H_2 are formed.

The principal focus of this work lies on the Water-Gas reactions as the predominant reactions in steam gasification processes. The heterogeneous water-gas (WG) reaction (2.8) leads to an increase in volume and is endothermic while the homogeneous WGS reaction (2.17) is slightly exothermic and stays constant in volume. The reaction equilibria, as shown in Figure 2.3, demonstrate which reaction products are formed under certain pressure, temperature and concentration conditions. The homogeneous WGS reaction is pressure independent, however, indicates an equilibrium shift towards CO and H_2O with increasing temperature. Similarly, high temperatures favor the heterogeneous WG reaction too, though, preferably at lower pressure values as heterogeneous reactions are by nature pressure dependent [30], [3].

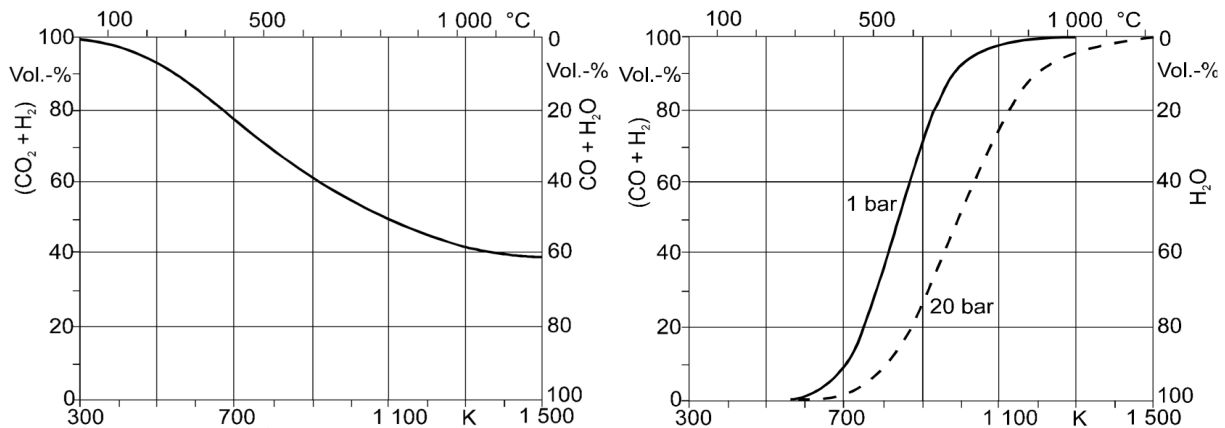
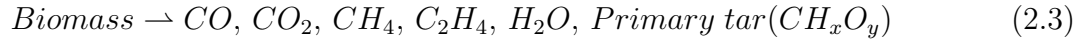
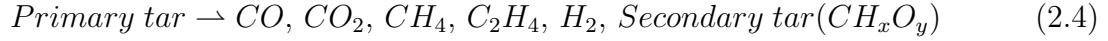
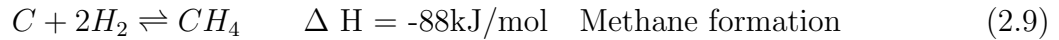
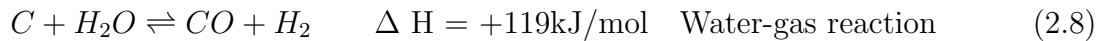
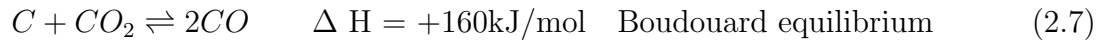
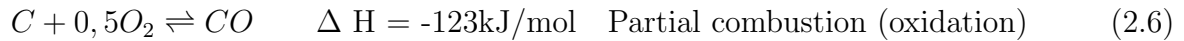
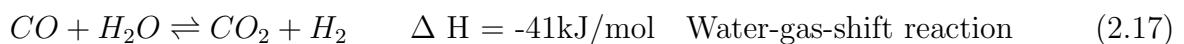
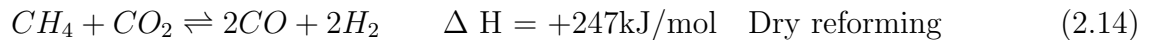
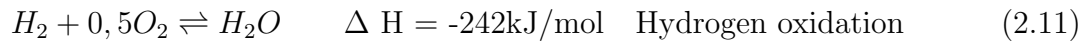


Figure 2.3: Reaction equilibrium homogeneous WGS (left) heterogeneous WGS (right) [3]

Moreover, methane formation (2.9) is disadvantaged at higher temperatures ensuring the preservation of valuable hydrogen gas. The free reaction enthalpy, however, gives no information about how fast a reaction will proceed even though $\Delta G < 0$ [30], [3].

Primary devolatilization**Tar cracking and reforming****Heterogeneous gas-phase (solid-gas) reactions**

The formed gases through solid-gas reactions (2.5 - 2.9) and by pyrolysis during devolatilization (2.3) and cracking (2.4) can undergo further gas-gas reactions (2.10 - 2.17).

Homogeneous gas-phase (gas-gas) reactions

Reaction kinetics

Is the premise of a reaction $\Delta G < 0$ fulfilled, the kinetic properties, that is how fast the reaction proceeds, become the decisive role in chemical manufacturing. Depending on pressure, temperature and reactant concentrations reaction kinetics change. The temperature dependence is characterized by the Arrhenius equation (2.18). The reaction rate constant k quantifies the rate of a chemical reaction. The parameter A is called the pre-exponential factor or the frequency factor. The parameter E_a is called the activation energy and represents the height of the barrier between the reactants and products.

$$\ln(k) = \ln(A) - \frac{E_a}{RT} \quad (2.18)$$

Although the homogeneous WGS reaction 2.17 would yield 80 % product at 700 K the reaction proceeds much faster at 900 K generating only 60 %, cf. Figure 2.3. Consequently, thermodynamic and kinetic control of a reaction always is an act of balance between the two. Self-explanatorily, more product is desirable, yet the operation has to be also timely feasible.

Due to higher temperatures chemical reaction rates typically become very fast, however, other effects are limiting the overall reaction velocity. Mass transfer, especially the diffusion of reactants onto the particle surface (for heterogeneous reactions) is shown to be the limiting factor. This does not mean the reaction proceeds slower at higher temperatures rather the change of limiting effects that inhibit the reaction from taking place even faster.

After pyrolysis carbon is present as a solid, thus for heterogeneous reactions a number of partial steps have to be overcome whereof the slowest of the steps determines the reaction rate (depending on reaction conditions) [3]:

1. Mass transfer of a gasification agent molecule into the reaction zone
2. Diffusion through the gas boundary layer towards the particle surface
3. Diffusion through the particle pores
4. Reaction of the gasification agent with the fuel particle
5. Diffusion of gaseous products from the particle surface
6. Diffusion of gaseous products through the boundary layer leaving the particle surface
7. Mass transfer outwards of the reaction zone

Ideal homogeneous reactions show different transport phenomena but very often homogeneous reactions are catalyzed on the surface of a catalyst particle. As a result, similar approaches can be used to understand this effects and will be further illustrated in section 2.3.1.

2.2 Design of industrial gasifiers

Several types of gasifiers have been developed for different types of biomass and product gas. Every one of them comes with advantages and disadvantages. They can be categorized on the basis of reactor type, heat supply, gasification agent or pressure conditions [3]. Figure 2.4 presents simple sketches of three main gasifier reactor types: fixed bed (updraft and downdraft), fluidized bed and entrained flow gasifier. Fixed bed reactors are characterized by an unmovable grate that keeps biomass in place. Air or other gasification agents enter the reactor from below in the updraft gasifier type whereas in downdraft gasifiers gasification agents enter the reactor at a certain height below the top. The product gas flows accordingly upwards or downwards by passing through hot ash and leaves the reactor. In fluidized bed reactors, the gasification agent enters the reactor from below and conveys fuel particles through the apparatus. Bed material and fuel particles behave like a fluid, hence the name fluidized and demonstrate typically very good mixing and a homogeneous temperature within the reactor. For entrained flow gasifiers, reactants are injected through a single burner at high temperatures and pressures. The fuel has to be very finely ground to be entrained by the oxygen stream into the reactor. All of the oxygen is consumed in the combustion zone close to the burner generating necessary heat for the adjacent gasification [2].

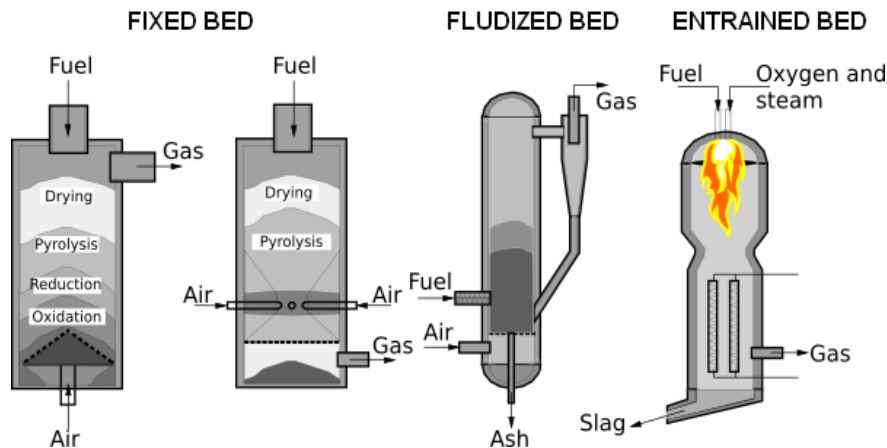


Figure 2.4: Overview of main gasifier reactor types [4]

Each gasifier type is operable in a designated power range as illustrated in Figure 2.5.

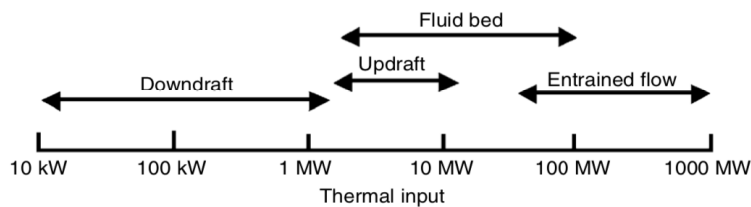


Figure 2.5: Power output of gasifier types [2]

Concerning biomass gasification the fluidized bed design offers many advantages. The excellent gas-solid mixing makes a cumbersome fuel preparation such as grinding superfluous. This makes the design relatively insensitive to fuel quality as fuel agglomeration is mostly obviated.

Under some circumstances, however, created ash may sinter and agglomerations of the bed materials occur. In particular, when the fusion temperature is surpassed ash defluidizes significantly the bed material [31]. On the other hand, FB reactors exhibit as entrained flow reactors low tar production compared to fixed bed reactors and thus facilitate downstream processes decisively [32].

Most notably, the bed material can be used not only as a means for mixing fuel and heat transport but also as a catalyst. Instead of using inert quartz as bed material an iron-rich mineral olivine was found to be not only mechanically robust but also catalytically active towards tar cracking.

2.2.1 Dual fluidized bed reactors

Gasification reactions are endothermic processes and thus consume more heat than they produce. Self-sustained gasifiers use air as a gasification agent featuring combustion zones to release sufficient amounts of heat for ensuing gasification reactions. Since pure oxygen is too expensive and energy intensive, the use of air dilutes the product gas with inert nitrogen and reduces immensely its heating value.

Nonetheless, if the combustion chamber is separated from the gasification chamber high product gas qualities are guaranteed. By using only steam as a gasification agent there is no dilution of product gas. The required heat is generated by combustion of a part of the biomass and is subsequently transferred into the endothermic gasifier, by circulation of bed material. Figure 2.6 (right) shows a simple layout of an external-circulating DFB gasifier that comprises a fast fluidized combustion zone where bed material is heated up. Eventually, hot bed material rises to the top and flows into the gasification chamber. To ensure constant temperatures, bed material is drained off to the combustion chamber circulating between both chambers. No external heating is required for this design as created char during pyrolysis in the gasification reactor is used as combustible.

Limitations of this set-up lie, firstly within the char content that can be produced by the employed biomass to generate sufficient amounts of heat. Secondly, only a fraction of steam participates in gasification reactions, the major part only dilutes the product gas and consumes large amounts of heat [2].

2.2.2 Notable industrial operations

In 2002 with participation of TU Vienna a steam blown gasifier producing heat and power ($4.5 MW_{th}$, $2 MW_{el}$) including a gas engine went into operation in Güssing, Austria. The centerpiece of the small-scale demonstration plant was a circulating dual fluidized bed reactor as illustrated in Figure 2.7. The product gas was cooled, cleaned (2 stages) and used in a gas engine to produce electric power. Wood chips from forestry served as biomass fuel with a water content of about 25-40 %. The heat produced in the process was partly used internally, e.g. for air preheating, steam production whereas the rest was delivered to an existing district heating system. The net electricity produced was fed into the electrical grid.

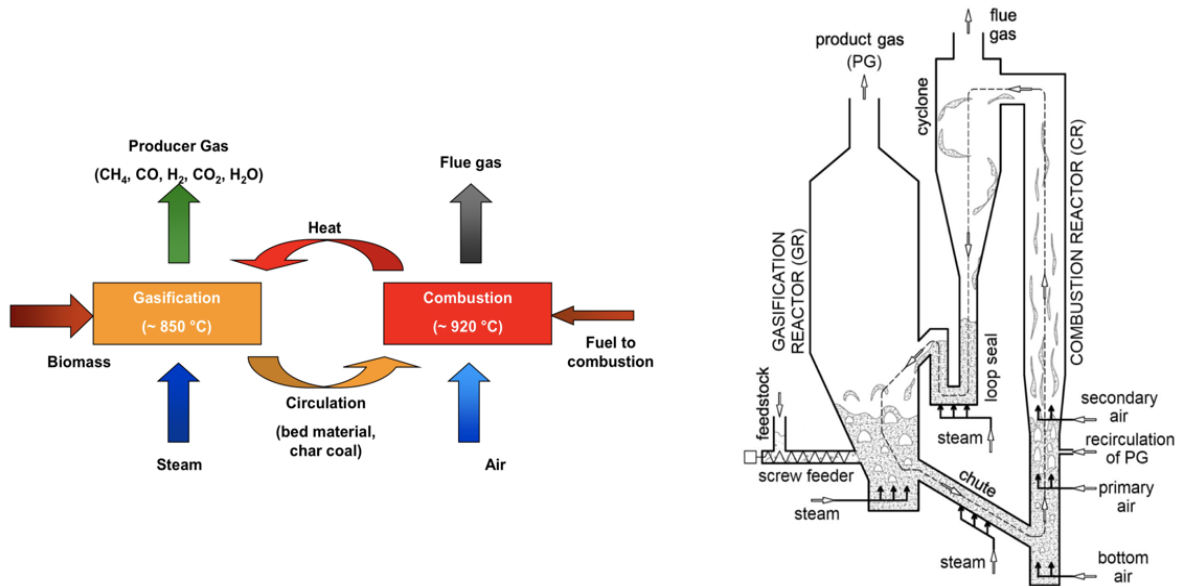


Figure 2.6: DFB principle scheme (left) and simplified reactor layout (right) for biomass gasification developed at TU Vienna [5]

The first stage of the product gas cleaning system comprises a fabric filter to separate the particles and some of the tar. These particles are not fully oxidized and are reintegrated into the combustion zone of the gasifier. The second stage consists of a scrubber that liberates the gas from tar by means of a scrubber. Saturated scrubber liquid with tars and condensate can be vaporized and fed for thermal disposal into the combustion reactor of the gasifier. Moreover, the scrubber is used to reduce the temperature of the clean synthesis gas to about 40°C . The clean gas is finally fed into a gas engine to produce electricity and heat. Alternatively, the product gas could be used for production of hydrogen and Fischer-Tropsch liquids or just burned to generate additional heat [6].

Unfortunately, in 2016 eco-electricity subsidies were discontinued by the government what made the plant economically unfeasible and was closed the same year.

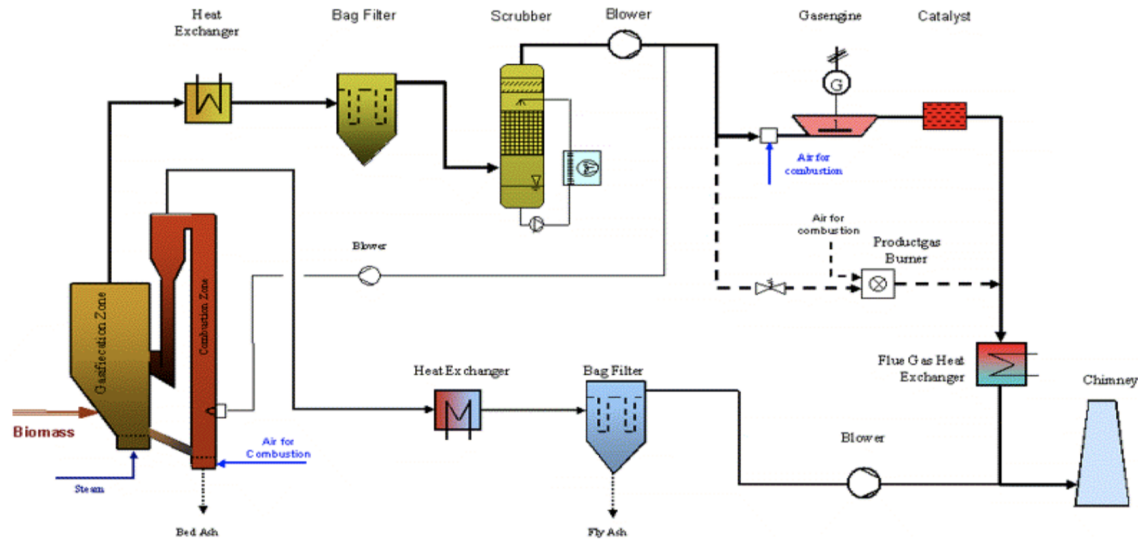


Figure 2.7: Flowsheet of the steam blown gasifier 8 MW CHP plant Güssing, Austria [6]

Ten countries (Austria, Denmark, Finland, Germany, Italy, Sweden, Switzerland, The Netherlands, Norway, USA) are participating the Task 33 of the IEA on thermal biomass gasification. Growing volumes of municipal waste [33] and increasing demand of renewable energy and hydrogen production [34] lead to the investigation and installation of gasification plants.

An excerpt of other ongoing commercial thermal biomass gasification facilities in Europe within Task 33 of the IEA [6] is presented in the following:

- Senden, Germany
generates electricity of around 2.5 MW in two gas engines and has the capacity to produce district heating of 4 MW. It uses wood chips as feedstock in a DFB design according to the power plant in Güssing.
- Gothenburg Biomass Gasification Project, GoBiGas, Sweden
produces biomethane (20 MW) by gasification of forest residues such as branches, roots and tops that is destined to replace natural gas in the future.
- Skive plant, Denmark
is a demonstration plant to convert wood-based biomass into electricity and district heating. The product gas contains about 20 % carbon monoxide (CO), 12 % carbon dioxide (CO_2), 16 % hydrogen (H_2) and 4 % methane (CH_4) by volume. It has a heating value of about 5 MJ/kg.
- Lahti Energy's Kymijärvi II, Finland
uses waste material as feedstock to produce electricity (50 MW) and district heating (90 MW).

2.3 Challenges and motivation

The point of gasification is the production of a product gas that can be further processed or burnt in spatial and temporal separation of its generation. The product gas is sometimes referred to as syngas when the product gas is cleaned and intended as raw material for chemical synthesis. Crucial for the process is the use of oxygen-rich gasification agents (i.e. air, oxygen, steam or carbon dioxide) for transforming residual carbon into combustible gases (i.a. CO and H_2) [3].

Challenges of turning solid biomass into a useful gas are manifold: high investment costs and a lack of political incentives impede a competitive production of heat or hydrogen compared to conventional combustion or steam reforming. IGCC plants (integrated gasification combined cycle) that exploit at maximum efficiency the production of product gas by utilizing exhaust heat to generate steam, involve high construction expenses. Still, to this day IGCC plants are unfortunately not economically competitive. To evaluate and compare gasification processes criteria and parameters were developed in order to evaluate and compare gasification performance [30], [3]:

- Fuel depended product gas
 - $CO : H_2$ Ratio
Dependent on biomass composition, choice and amount of gasification agent, reactor temperature and pressure
 - Lower heating value of product gas (LHV)
Percentage of chemical energy contained in the product gas in relation to the initial fuel
 - Cold gas efficiency (CGE)
Percentage of energy input over the potential energy output. When a mass of solid fuel M_s is produced into a mass of gas M_g with an LHV of Q_g resulting in a cold gas efficiency η as depicted by formula 2.19. Modern gasifiers yield between 70 - 80% of CGE.

$$\eta = \frac{Q_g M_g}{LHV_f M_f} \quad (2.19)$$

- Fuel conversion
 - Carbon conversion
Ratio of initial carbon to produced carbon monoxide or dioxide

The most problematic issue during gasification are however contaminants in the product gas such as tars, NO_x , SO_x and Particles (e.g. fine ash). Tar reduction in particular is a cumbersome process. The condensable polyaromatic compounds, if not properly removed, cause clogging and fouling of the heat exchanger pipes. Conventionally, scrubbers are employed to take out tars as they are soluble in the scrubber liquid. The commonly utilized rapeseed methyl esters (RME) or biodiesel are burned after the usage, causing high costs in relation to other operational expenses.

Another important consideration for a successful operation of a fluidized biomass gasification is the consideration of the ash melting temperature. Residues like potassium lower the ash melting temperature leading to agglomerations of the bed material. Accordingly, the ash melting temperature varies with the fuel as does the ash content. Woody biomass produces little ash 5-8 % with ash melting temperatures $> 1000^{\circ}\text{C}$. A more problematic fuel is straw, remaining ash shows melting temperatures around 700°C . Since the wood gasification is not economically feasible other wastes such as straw or even sewage sludge are targeted. These rather complex wastes involve however sophisticated reactor design and control as more ash with sometimes low melting temperatures is generated.

Albeit many obstacles and challenges gasification is an already quite established industrial process all around the world. To compete with much more worked out petrochemical processes (that have had an over 100 years head start) more research has to be done.

Motivation for gasification today lies in versatility of applications of product gas or syngas - as fuel gas or as precursor for chemical synthesis. Higher exhibited electrical efficiencies are realized with gas engines compared to Rankine cycles where biomass is combusted to heat a boiler driving a steam turbine. Moreover, CHP applications (combined heat and power) allow parallel production of product gas and heat at maximum efficiency. Despite some inconveniences, there is a huge potential for the high value exploitation of otherwise unused or only thermally used wastes such as sewage sludge or animal waste. In addition, the IGCC plants are able to integrate CO_2 capture and storage technologies. What is more, the employment of CO_2 as a gasification agent is thinkable.

To conclude, the renewable production of energy, fuels and chemical products is the major motivation for gasification today. Crucial for future integration of biomass and waste gasification in modern energy production, process optimization is crucial [30], [2].

2.4 Catalysts for biomass gasification

2.4.1 Beginnings and development

As early as the 1950s, additives for heavy oil cracking were introduced to fluidized bed gasifiers by Yamamoto et.al. [35]. It was found that catalysts most notably dolomite and nickel were best suited for this purpose. $CaCO_3$ yielded the best results in terms of heat efficiency (ratio of total heating values of the gas produced to the heating values of feed oil) whereas nickel catalysts were rendered inactive by carbon and sulfur compound deposits during prolonged operating times.

Since the mid-1980s, after the revival of gasification as an alternative to fossil fuels, interest has grown not only on oil gasifiers but rather on the subject of catalysis for biomass gasification. In addition to tar cracking properties of the catalyst also pollution control i.e. NO_x and SO_x removal as well as methane reformation for syngas production is desired. To tackle the increasing requests for catalysts multiple types have been developed. For biomass gasification two groups of catalysts can be distinguished [36]. The first group of catalysts (primary catalysts) is added directly to the biomass prior to gasification. These catalysts are purposed to reduce the tar content as indicated by the equation 2.10 and have little effect on the conversion of methane and hydrocarbons in the product gas. They operate under the same conditions of the gasifier and are to be refilled only as small particles are conveyed out of the reactor by the product gas.

The second group of catalysts (secondary catalysts) is placed in an additional reactor downstream from the gasifier. Independent of the type of gasifier, they can be operated under different conditions than those of the gasification unit. The catalysts are active in reforming hydrocarbons and methane according to formulas 2.14 and 2.15.

The primary catalysts are of much more interest as they do not depend on additional reactors and equipment. Following up the research on coal and heavy oil gasification, dolomite ($MgO.CaO$) was found to be favoring tar cracking reactions also in biomass [37], [38]. Deployed as primary catalyst it is dry-mixed with biomass but during calcination of the mineral it becomes very brittle and produces a fine powder that impedes stable reactor operation. In the same studies ferrous rocks were also shown to be catalytically active towards tar reduction, albeit significantly less compared to dolomite. Still, this catalytically active role of iron triggered a change of strategy away from additive catalysts towards catalytically active bed materials. During a systematic study of Gruidl, T. at TU Wien the iron-rich, magnesium silicate Olivine ($(Fe, Mg)SiO_4$) turned out not only to be mechanically sufficiently resilient but also catalytically active. Natural Olivine represents a blend of Forsterite (Mg_2SiO_4) and Fayalite (Fe_2SiO_4) with ratios often occurring as $(Fe_{0,12}, Mg_{0,88}SiO_4$) [39]. Further studies showed the potential of olivine as a bed material for FB biomass gasifiers [40]. It was not much later discovered that ash layers are formed on the bed material grains that are even more catalytically active than the native olivine [27]. The positive catalytic effects have been attributed to Ca-rich ash layers leading to a significant improvement of the product gas quality. Kirnbauer et al. showed a decrease of up to 80 % for tars detectable by gas chromatography when using layered olivine compared to fresh olivine. Regarding the the Water-Gas-Shift reaction, cf. formula 2.17, produced a gas containing three times more H_2 with layered olivine compared to fresh olivine [41].

However, the disposal of bottom ash including olivine involves a much more complex and costly disposal due to non-neglectable heavy metal concentrations such as Chromium and Nickel. For this reason, other materials are investigated as bed material.

Two candidates, quartz and feldspar, were found eligible as bed material and carriers for catalytically active ash layers. For its abundance and mechanical stability Quartz (SiO_2) is a widely studied bed material for gasification. Nonetheless, Quartz bed materials are prone to form agglomerates as ash layers form, in particular when employed with potassium-rich fuels. It was shown that potassium can react with silicon in the Quartz structure to form melts that cause agglomeration [42].

Feldspars on the other hand have been much less studied as a bed material in gasification. Similar in abundance and mechanical strength, it is like Quartz a good candidate for bed material in biomass gasification. The mineral group of Feldspars comprises essentially three endmembers differing in the counterion K , Na or Ca with corresponding formulas $KAlSi_3O_8$, $NaAlSi_3O_8$ and $CaAl_2Si_2O_8$ [43]. Naturally occurring are often mixtures of all three endmembers and if employed as a bed material Feldspar shows catalytic activity towards tar reforming [44] and was tested in a 2 MW gasifier [45]. The pure K-Feldspar, however, is catalytically completely inactive. A gradual activation by layer formation can be realized depending on the employed time and fuel [46].

The formation of layers depends on fuel composition and the bed material itself. It was demonstrated that fuels with a high ash content, such as straw or chicken manure, yield a quick and thick layer formation. Contrary to Quartz Feldspar showed no formation of silicate melts with potassium rich fuels and no agglomeration [46], [47].

It was shown by EDX measurements that the ash layer is rich in calcium for both Olivine and Feldspar bed materials [27], [46]. The thickness of the layer was found to be up to 50 μm and is depicted in Figure 2.8. Furthermore, the ash layer formation seems to be equal in both FB combustion and DFB gasification as ash layer formation probably occurs in combustion zone [48], [49]. The conversion of a model tar compound, toluene, was enhanced significantly by the ash layer on Olivine grains [50], [7] whereas Feldspar fresh showed no conversion and CaO 100 % conversion.

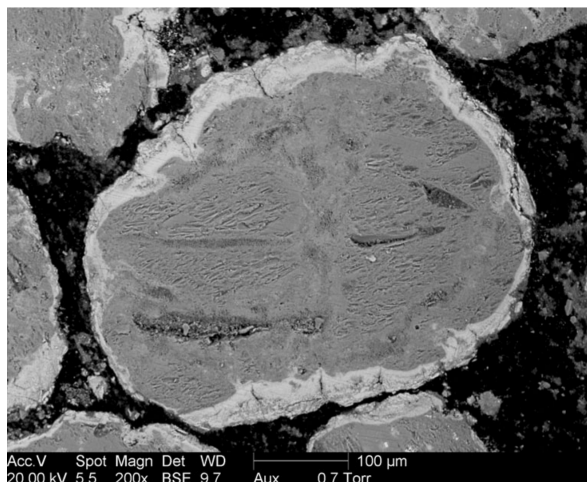


Figure 2.8: Backscattered SEM image of an Olivine used cross-section showing an ash layer of heavier elements [7]

Experiments at the pilot gasification power plant in Güssing further substantiate the positive effects of the ash layer on Olivine bed material. Significantly lower tar contents and higher H_2 concentrations were measured in the product gas when employing used Olivine rather than fresh Olivine [41]. Moreover, recent research findings conclude positive effects of ash layers on Feldspar. Indications of a correlation between H_2 concentrations in the product gas and the residence time of Feldspar bed material in the fluidized bed reactor were found. This effect is even more pronounced for fuels with a high ash content [51].

In that sense, the surface morphology of bed material grains and its ash layer composition seems to be the pivotal aspect for catalytic activity.

Concerning the effects of alkali elements, predominantly calcium, on gasification reactions various mechanisms have been proposed. For instance the effect of alkali on the unzipping of cellulose chains [52] has been discussed or the potential for alkali carbonates to promote the formation of liquid-surface [53]. Other published studies have suggested that the observed effects of alkali-elements are linked to oxygen transport to the tars, thereby facilitating their oxidation [54].

The effectiveness of Olivine used bed material compares to other industrial catalysts such as *Ni*- or *Fe*- catalysts. H_2 concentrations up to 44 % in the product gas for steam gasification of wood residues with ash layered Olivine bed material were registered [41]. Xiao et.al. achieved H_2 concentrations up to 45-50 % in the product gas by steam gasification of red pine wood by deploying a *Ni*-catalyst bed above the fluidized bed reactor [55]. Enrichment of Olivine bed material with nickel increased H_2 concentrations to only 45 % in DFB gasification reactors [56].

Since ash deposits not only on bed material grains but also on metal catalysts their lifetime is limited. Compared to ash layered bed material face heavy metal catalysts a problematic disposal with only a small increase in H_2 concentrations.

2.4.2 Principles of heterogeneous catalysis

Rates of reaction usually go up when the temperature increases, as stated in section 2.1. However, temperature increase is not effortlessly realized. Firstly, heating is extremely energy-intensive and not very economical. Secondly, and perhaps more importantly, certain operations face technical temperature limits. Some reactions are only thermodynamically possible at low temperatures, e.g. the conversion of N_2 and H_2 to NH_3 is practically impossible above $600\text{ }^\circ\text{C}$. Furthermore, reactors that maintain safely extreme conditions are difficult to make considering melting points of the construction material. Gasification operations in particular need to be carried out below the ash melting temperature that would otherwise lead to agglomerations of the fluidized bed [30].

In addition to regular reaction control on the basis of temperature, concentration, pressure and contact time, catalysis constitutes a powerful tool. Catalysts accelerate reactions by orders of magnitude and thus enable industrially important reactions to be carried out in the most favorable thermodynamic regime and at much lower temperatures and pressures [8].

The essence of a catalyst lies in the formation of bonds within the reaction molecules and allowing these to react to a product and by leaving the catalyst itself unaltered to be available for the next reaction. Figure 2.9 displays a potential energy diagram for a gaseous reaction. The non-catalytic reaction proceeds when A and B collide with sufficient amount of energy to overcome the activation barrier.

The catalytic reaction, on the other hand, starts by bonding of the reactants A and B to the catalyst surface. In heterogeneous catalysis the catalyst is a solid while reactants are liquid or gaseous. The adsorption process is exothermic and the free energy is lowered. Whilst being bound to the catalyst A and B react to (an intermediate) product P^* after overcoming a small activation barrier. Finally, the product P^* detaches from the catalyst surface in an endothermic step to the final product P [8].

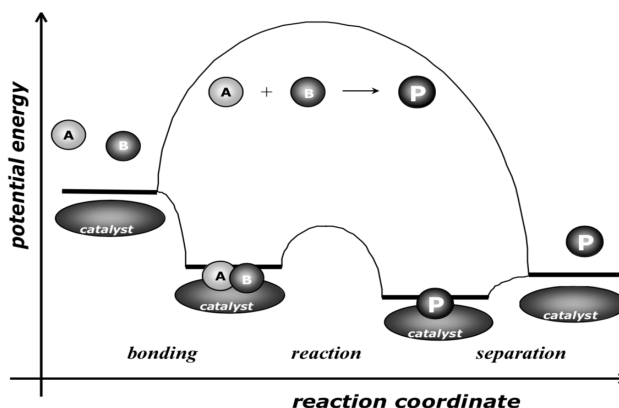


Figure 2.9: Potential energy diagram of a gaseous reaction without catalyst that overcomes a substantial energy barrier contrasted to the same reaction with a solid catalyst [8]

In conclusion, catalysts render the reaction more complex but also energetically much more favorable. Catalyst deployment increases reaction rate (kinetics) but does not change the thermodynamic situation. As reactants adsorb on the catalyst surface, the surface area or rather the distribution of active sites on the surface is pivotal for the catalyst performance.

2.5 Catalyst characterization

The characterization of bulk and surface properties is essential for an understanding of the nature of an active catalyst and the first step towards optimization. Bulk analysis comprises analytical methods with information depths that go very deep into the sample in contrast to surface analysis where only near surface layers are probed.

Good research practice insists on cross verification of found results by different sources and methods. Each presented analysis approach provides a piece of information to be assembled to a complete picture. Every method shows specific advantages but also limitations, together they corroborate and complement each other.

2.5.1 Colorimetry

The simplest examination of unknown substances is by visual inspection. First distinctions can be drawn by observing differences in color that may indicate disparate compositions of samples. (UV-)VIS spectrophotometer measure the reflected wavelength distribution ensuring a precise color assignment. The collected spectra then can be transformed into CIE color values [57]. The CIE color space, established in 1931 by the international commission on illumination, is based on human color perception. The retina in the human eye comprises three color sensors, blue, green and red (orange to be precise). The human three color parameters (RGB) are translated into a three dimensional XYZ coordinate system. Consequently, each measured VIS spectrum can be transposed as a point in a 2D projection of the XYZ coordinate system, depicted in Figure 2.10. The concept allows a color to be separated into chromaticity and brightness information. The 2D image therefore represents the chromaticity of a color regardless its brightness, visible to the average person. An example clarifies the idea: grey and white share the same chromaticity differing only in brightness.

In Figure 2.10 the outer curved boundary represents the spectral locus with wavelengths shown in nanometers whereas x and y represent the three stimuli (XYZ). The white point is found at $y = x = 0.33$ the equal blend of red, green and blue [9].

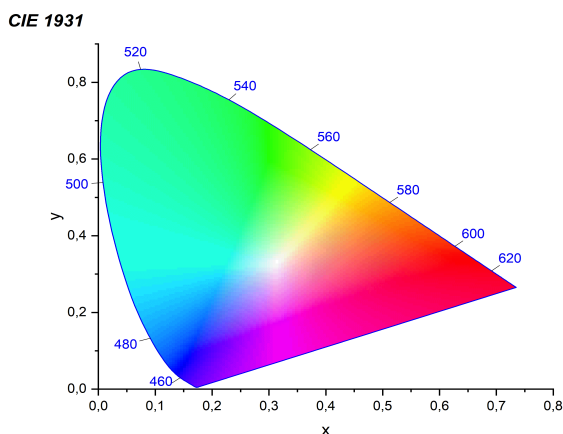


Figure 2.10: CIE 1931 color space chromaticity diagram [9]

2.5.2 Scanning electron microscopy (SEM)

Microscopes allow the examination of small objects by magnification, yet face resolution limits. The resolution of optical microscopes, i.e. the minimum distance between two objects that leads to two distinct images, is on the order of the wavelength of light used as a probe. Conventional microscopes employing visible light have resolutions in the micrometer range and are blind to features on a nanometer scale. The discovery of the wave-particle duality of elementary particles such as electrons entailed a wide range of innovations and new analytical techniques. Electron microscopy, in which a beam of electrons, with a well-defined de Broglie wavelength, replaces the lamp found in traditional light microscopes. Magnetic fields are used instead of glass lenses to focus the beam onto the specimen. In scanning electron microscopy (SEM) electrons scattered back from a small irradiated area of the sample are detected and the electrical signal is sent to a video screen. An image of the surface is then obtained by scanning the electron beam across the sample.

As in traditional light microscopy, the wavelength of and the ability to focus the, in this case electron beam, govern the resolution. Electron wavelengths can be as short as 10 *pm*, however, magnetic lenses are not able to focus electrons so well. Typical resolutions for SEM instruments are above 50 *nm*. As a consequence, individual atoms cannot be resolved (with typical diameters of about 0.2 *nm*) [29].

Irradiation of a sample with electrons produces a wealth of signals due to many possible interactions between primary electrons and the target. The most notable interactions of electrons with matter are illustrated in Figure 2.11. Information on the surface texture is collected by measuring secondary electrons (SE). Secondary electrons are emitted due to inelastic scattering of the incident electron beam as primary electrons pass kinetic energy onto a bound electron. Due to their low energy secondary electrons escape the sample only from a few nanometers below the surface. The brightness of the signal corresponds to the number of electrons reaching the detector. At edges more electrons are emitted likewise less electrons from dents leave the sample so they appear darker. This phenomenon is called edge effect.

Incident electrons also interact elastically with the sample, these electrons are then called backscattered electrons (BSE). Backscattered electrons possess more energy and can therefore reach the detector from greater depths compared to secondary electrons. Moreover, electrons are much easier scattered the heavier the probed elements are. Thus, brighter areas in the BSE image indicate heavier elements.

Photonic signals are also excited (including x-rays) when primary electrons that interact with inner orbital electrons of the sample (see section 2.4.3 below). Furthermore, a detector can also be placed beneath a thin sample that collects information about interactions during the transmission of electrons through the sample. This technique is specified as transmission electron spectroscopy (TEM) [58].

2.5.3 Energy dispersive x-ray spectroscopy (EDXS)

The generation of x-rays is often a secondary process, preceded by the ionization of an atom. X-ray spectroscopy is widely integrated in SEM instruments as x-radiation emission is a consequence of electron bombardment. The x-radiation emitted is produced during inelastic interactions of primary electrons and electrons in inner orbitals as illustrated in Figure 2.11 (bottom right). The transferred energy leads to the excitation of the inner orbital electron

to a higher unoccupied energy state or even into the vacuum. As a result, a “hole” is left behind (where the electron had been) and the atom is ionized. After a short dwell time the excited system relaxes and the hole is filled with an electron from a higher orbital. The energy difference between the “hole” and the higher orbital is compensated by the emission of either Auger electrons or x-rays [58].

The x-ray wavelength or energy is characteristic for each element giving information about the chemical composition of the specimen. Not only depends the spatial extension of the volume from which a specific interaction signal is gained on the diameter and energy of the electron beam but also heavily on the material itself. Each individual interaction process can change the direction of the electron path within the specimen, leading to a broadening of the average diameter of the electron beam. In massive silicon, for instance, electrons undergo a large number of elastic and inelastic interactions during their passage through the material, until they are completely stopped. The resulting penetration depth is approximately $50\ \mu\text{m}$, whilst in perpendicular direction almost twice that. The resolution is for every element different, however in another method for foil specimen in transmission electron microscopy (TEM) much higher lateral resolutions are obtained due to less beam broadening along a thin sample.

In EDX spectra, the x-ray intensity is plotted against energy and comprise typically several approximately gaussian-shaped peaks characteristic of the elements present. Most chemical elements can be identified by EDXS, however, limitations arise out of particular detector windows. Modern detectors with light-element windows are able to register even soft x-rays corresponding to atomic numbers $Z=5$ (Boron). Quantitative EDXS analysis involves the determination of the background contribution, background subtraction and counting the net intensities of characteristic peaks. The most simple background extrapolation is averaging the background intensities. Good quantifications, however, require the measurement of standards yielding exact correlations of counts to concentrations [58].

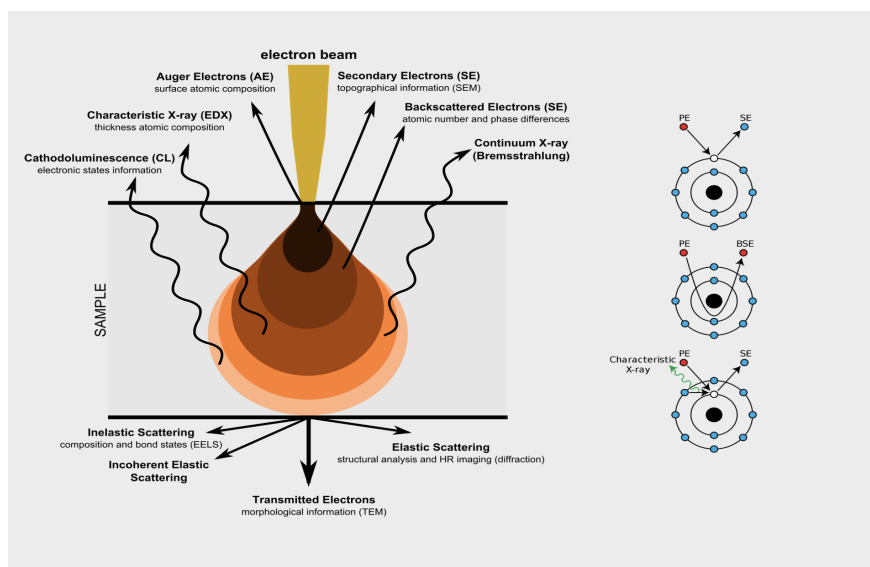


Figure 2.11: Electron interactions with matter (left) [10] and emission mechanisms (right) [11]

2.5.4 Assessment of surface area (BET method)

Resuming the first morphological assessment of a catalyst by SEM imaging, that is, how the surface looks like (derived from the greek *morphé* - shape and *lógos* - teaching) a more thorough examination of surface details is sought. Electron microscopes will disclose small imperfections and pores of the surface, irregularities and details smaller than the microscope's resolving power will, however, remain hidden. Also not accessible for microscopes is the pore distribution and its contribution to the surface area. The surface area is a crucial quality of a catalyst describing directly its surface reaction capacities - the larger the surface area, the more reactants can adsorb simultaneously to the surface resulting in a higher catalytic activity.

The most widely accepted method to measure surface areas of porous solids and powders is by BET gas adsorption. By enveloping a particle in an adsorbed film, the method of gas adsorption can probe the surface irregularities and pore interiors even at the atomic level [29].

Depending on the interaction strength, adsorption is divided into physisorption and chemisorption processes. The irreversible or chemical adsorption of gases involves large interaction energies approaching the value of chemical bonds. High heats of adsorption (all adsorption processes are exothermic) indicate structural changes of adsorbate and adsorbent as they undergo a quasi chemical bond. The second category called reversible or physical adsorption comprises lower interaction energies and lower heats of adsorption indicating a binding by intermolecular forces. Attraction is induced by dipole moments (that are caused by electron movement) of the adsorbate and adsorbent surface molecules that couple into phase, as described by F. London and J. van der Waals [59].

The characteristics of physisorption make it more suitable for surface area determination: i.a. little or no surface alteration of the sample; it may form multilayers to measure pore volumes; there is no physisorption at elevated temperatures so relatively clean surfaces can be prepared prior to the measurement; the reversibility allows a studying of the adsorption and desorption; physisorption is not restricted to specific sites and therefore probe molecules cover the entire surface. S. Brunauer, P. Emmett and E. Teller studied previous adsorption theories and developed further Langmuir's kinetic theory of adsorbate monolayers to a multilayer adsorbate formation [60]. The amount of adsorbate on a solid surface herein depends on temperature, pressure and their interaction potential. At constant temperature the adsorbate equilibrium pressure over the sample and the added mass of adsorbate are measured. The obtained plot of adsorbate mass to relative pressure is called adsorption isotherm [59].

In 1985 IUPAC recommended the classification of adsorption isotherms into six types, illustrated in Figure 2.12. It has been shown that each type is strongly related to particular pore structures. Type I isotherms are given by microporous solids with relatively small surface areas. Type II isotherms stem from adsorption of most gases on non porous or macroporous solids. Point B corresponds, in most cases, to the completion of monolayer coverage. The linear section indicates the start of formation of an adsorbed multilayer and appears to increase without limit when $p/p^0 = 1$. Type III lacks a point B and therefore shows no monolayer formation. Type IV isotherms are given by mesoporous solids with monolayer formation similar to type II but is followed by pore condensation. Type IV isotherm that become horizontal near $p/p^0 = 1$ indicate the absence of macropores, composite types II + IV on the other hand with no horizontal section near $p/p^0 = 1$ evidence the presence of

macropores. Hereby condensation of gas to a liquid-like state inside pores is observed at pressures less than the saturation pressure p^0 and is indicated in the plot as a plateau at high pressures. Striking in type IV(a) isotherms is the occurrence of a hysteresis loop. This difference in adsorption and desorption behavior happens when the pore width exceeds a certain critical width. Hysteresis starts to occur for pores wider than 4 nm with nitrogen as probe molecule. With adsorbents having mesopores of smaller width, completely reversible Type IV(b) isotherms are observed. Type V isotherms share great similarity with type III showing low adsorbate-adsorbent interactions. Type VI demonstrates a stepwise adsorption on a non porous solid [12].

Similarly, IUPAC also classifies pores of widths exceeding about 50 nm as macropores, pores of widths between 2 nm and 50 nm are called mesopores and pores with widths not exceeding about 2 nm are called micropores [12].

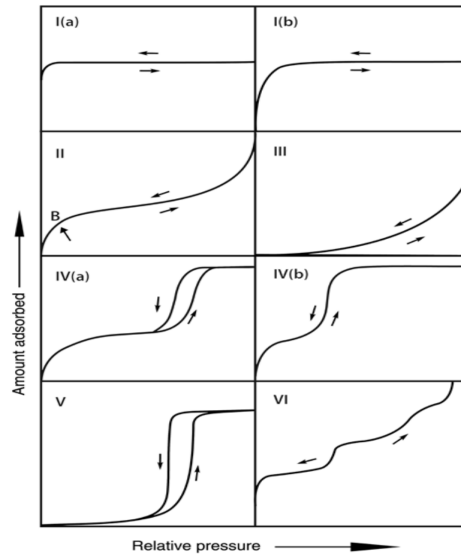


Figure 2.12: Classification of physisorption isotherms (IUPAC update 2015) [12]

The BET-area can be regarded as the area accessible to the specified probe molecule. To calculate the surface area, the physisorption isotherm is firstly transformed into the BET plot, by applying the linear BET equation 2.20 where n represents the specific amount adsorbed at p/p^0 and n_m as the specific monolayer capacity. The parameter C is related to the monolayer adsorption capability. C is above 80 when the knee of the isotherm is sharp and point B well defined. The value is below 50 for isotherms where B is not well defined by a single point and the derived specific monolayer capacity n_m is questionable. When $C < 2$, the isotherm is either type III or V and the BET method is not applicable. Also for type I and VI other methods have to be found.

$$\frac{p/p^0}{n(1 - p/p^0)} = \frac{1}{n_m C} + \frac{C - 1}{n_m C} (p/p^0) \quad (2.20)$$

Subsequently, with knowledge of n_m (derived from the BET plot) and the molecular cross-sectional area σ_m , occupied by the adsorbate molecule in the complete monolayer, the BET specific area $a_S(BET)$ can be calculated. L denotes the Avogadro number and m the adsorbent (sample) mass. Nitrogen (at its boiling temperature, 77 K) is traditionally the adsorptive generally used with $\sigma_m(N_2)$ assumed to be 0.162 nm².

$$a_S(BET) = n_m L \sigma_m / m \quad (2.21)$$

In spite the success of the BET method, some assumptions of the theory are disputable. The theory assumes an energetically homogeneous surface, that is, all the adsorption sites were energetically identical which may e.g. for an heterogeneous sample or an irregular surface not be the case. Further, it ignores all lateral interaction of the adsorbed species that may cause an error in the calculation [59]. Moreover, the already mentioned cross-sectional area σ_m may change up to 20 % due to the quadrupole moment of nitrogen, making different orientations of the molecule on the surface possible [12].

Furthermore, the BET method lacks information about the prevalent pores in the specimen. The method of Barrett, Joyner, and Halenda (BJH) is a procedure for calculating pore size distributions from experimental isotherms using the Kelvin model of pore filling. The Kelvin equation describes the change of vapor pressure on curved liquid-vapor interfaces. Cylindrical pores are assumed and a total pore volume is derived, with knowledge of the total surface area the diameter of the pores can be estimated.

It applies, however, only to the mesopore and small macropore size range thus corresponding to type IV isotherms. Moreover, lacking in accuracy pore diameters below 10 nm will be underestimated by 20 - 30 % [12].

2.5.5 Energy dispersive x-ray fluorescence (EDXRF)

One of the most straight-forward methods yielding the elemental distribution is represented by EDXRF or short XRF spectroscopy. Similarly to EDX, atoms of the specimen are excited whereby an inner orbital electron moves to a higher state or leaves the atom. XRF differs from EDX in how the specimen is excited. In XRF x-radiation serves as excitation source rather than electron bombardment. The analysis is non-destructive and does not need sample preparation with measurement times ranging in the seconds. As no vacuum is needed for the measurement mobile devices are available that further facilitate the measurements and make on-site analysis possible.

Based on the photoelectric effect, in XRF an electron is ejected from the atom as it takes up the energy of incident x-radiation. For photoemission to occur, the photon interacting with the specimen atom has to surpass a threshold energy, denoted as ionization energy what is reached by x-radiation for inner orbital electrons. Subsequent to the electron ejection, the generated "hole" is filled by an electron from an outer orbital whereby the energy difference is compensated by emitting secondary x-radiation. This effect is called x-ray fluorescence. Corresponding to the energy difference of the orbitals involved characteristic radiation energies for the elements present are released. Energy dispersive x-ray detectors collect spectra similar to EDX where each x-ray energy corresponds to an electron transition characteristic for one element. However, more than one x-ray energy can correspond to one element. As illustrated in Figure 2.13, K- α denotes the fall of the next higher electron to the K-shell whereas K- β indicates the fall from the following shell. Consequently, two x-ray fluorescence energies, green indicating a higher energy and red a lower energy are observed even though originating from the same atom. This slight energy difference is relatively small compared to energy differences to other elements and does usually not impede peak assignment [61].

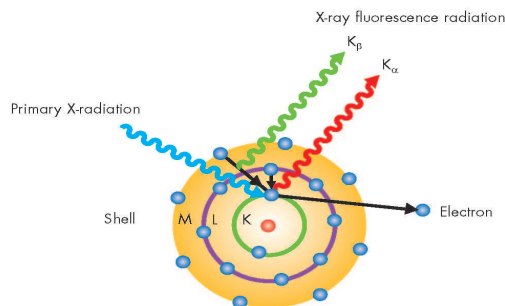


Figure 2.13: Simplified scheme of the XRF principle based on the Bohr model of atoms [13]

In principle, even light elements such as Beryllium or Boron are possible to detect, however, due to instrumental limitations and low x-ray emission of light elements the practical limit of detection is Sodium ($Z=11$). As an X-ray passes through matter it decreases in intensity primarily due to collisions with atoms. Owing to attenuation of an x-ray beam passing through a homogeneous medium the number of photons decreases exponentially, controlled by Lambert-Beer's law. The heavier the element the higher the mass-attenuation coefficient becomes resulting in reduced penetration depths [62], [61]. To give an idea of encountered orders of magnitude following examples are given for x-radiation incidence at right angles and 20 keV [63]:

- Fe_2SiO_4 Fayalite ($\rho = 4.4\text{ g/cm}^3$) attenuation length around $175\ \mu\text{m}$
- Mg_2SiO_4 Forsterite ($\rho = 3.3\text{ g/cm}^3$) attenuation length around $1500\ \mu\text{m}$
- $(Fe_{0.12}Mg_{0.88})SiO_4$ ($\rho = 3.4\text{ g/cm}^3$) attenuation length around $1000\ \mu\text{m}$
- $KAlSi_3O_8$ K-Feldspar ($\rho = 2.5\text{ g/cm}^3$) attenuation length around $1200\ \mu\text{m}$
- CaO ($\rho = 3.37\text{ g/cm}^3$) attenuation length around $300\ \mu\text{m}$

Given the large attenuation lengths (the distance into a material where the intensity of the beam has dropped to $1/e$) XRF methods show only the bulk composition of specimens and do not allow surface analysis.

2.5.6 X-ray diffraction (XRD)

X-ray diffraction is one of the oldest and most frequently applied techniques in catalyst characterization as it allows to identify crystallographic phases. Compared to other techniques XRD provides insight not only in the elemental composition but what is more in the chemical phases of which the specimen is made of. Diffraction always occurs when a wave front strikes obstacles or slits of the same dimension as its wavelength. X-ray diffraction takes place in the elastic scattering of x-ray photons by atoms in a periodic lattice. The scattered monochromatic x-rays at two different lattice planes that are in phase give constructive interference. Figure 2.14 (bottom left) illustrates how diffraction of x-rays allows the calculation of lattice spacings by using the Bragg relation [8]:

$$n\lambda = 2d\sin(\theta) \quad (2.22)$$

where λ is the wavelength of the x-rays and d the distance between two lattice planes. θ is the angle between the incoming x-rays and the normal to the reflecting lattice plane, n is an integer called the order of the reflection. When angles 2θ are measured, under which constructively interfering x-rays leave the crystal, the Bragg relation 2.22 gives the corresponding lattice spacings, which are characteristic for a particular compound [8].

Diffractograms are measured as a function of the angle 2θ . A rotation of the specimen during the measurement augments the number of particles that contribute to diffraction as they are not necessarily oriented in the same direction, see illustration 2.14 top right.

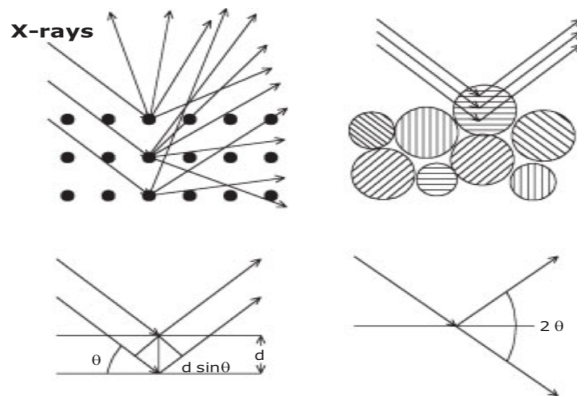


Figure 2.14: Illustrations of x-ray scattering at an ordered lattice as a function of the angle 2θ [8]

Important limitations to XRD are for one the sufficiently large ordered structures, amorphous compounds are not identified. Hence, there is always the possibility of more phases present than detected with XRD. Moreover, the crystallite sizes need to be larger than 100 nm as smaller sizes do not yield sharp peaks. Analogous to XRF, XRD passes through the sample yielding no specific information on surface characteristics but rather on the bulk composition.

2.5.7 X-ray photoelectron spectroscopy (XPS)

One of the most important surface analysis tools is XPS. It yields not only information on the elemental composition but also provides information of the oxidation state. As XRF it is based on the photoelectric effect, however in XPS the ejected electron is analyzed not fluorescence radiation, cf. Figure 2.13. After irradiation of the surface with x-radiation an atom can absorb the entire energy of a photon $h\nu$ so that a core or valence electron with binding energy E_b is ejected with a kinetic energy E_{kin} :

$$E_{kin} = h\nu - E_b - \phi \quad (2.23)$$

where h represents Planck's constant and ϕ is a small, almost constant, work function term specific for the spectrometer. By measuring the kinetic energy of the photoelectron and knowledge of the frequency of the exciting radiation ν the binding energy E_b can be calculated. No two elements share the same set of electronic binding energies - the premise for elemental analysis. In addition, any changes in E_b are reflected in E_{kin} , in other words slight changes in the chemical environment of an atom can be followed by monitoring changes in the kinetic energy of the photoelectron providing further chemical information [58], [8].

Routinely applied x-radiation sources for XPS exhibit energies between 1-1.5 keV (contrasting > 20 keV for XRF) resulting in kinetic energies of photoelectrons in the range 0-1 keV. At these low energies electrons travel no more than a few atomic distances through the solid. The mean free path of an electron depends on its kinetic energy and characterizes the average distance travelled by the electron. It was found the optimum surface sensitivity is obtained with photoelectrons ranging between 20-200 eV where the mean free path is limited to less than 1 nm.

The obtained XPS spectrum comprises the intensity of detected photoelectrons as ordinate axis and the binding energy in eV as abscissa. In addition to the expected photoelectron peaks, the spectrum features also peaks due to Auger electron emission. The “hole”, left behind after the ejection of the photoelectron is filled by an higher orbital electron. Instead of compensating the energy difference by photon emission the surplus energy can be passed onto a valence electron that is in consequence ejected, as illustrated in Figure 2.15. Auger electrons have fixed kinetic energies, independent of the energy that generated the initial hole. Nevertheless, the peaks are plotted on the binding energy scale (bearing no physical meaning) and can be spotted by recording the spectrum at two different x-ray energies. Photoelectron peaks will appear at the same binding energy while Auger electrons shift according to the excitation energy. This issue is elegantly solved by the utilization of a dual anode of *Mg* and *Al* in the x-ray source.

Photoelectron peaks are labeled according to the quantum numbers of the level from which the electron originates. Whereas an Auger electron labeled KLM originated from a transition with the initial hole in the K shell, which is filled by an electron from the L shell and the Auger electron emitted from the M shell. [8].

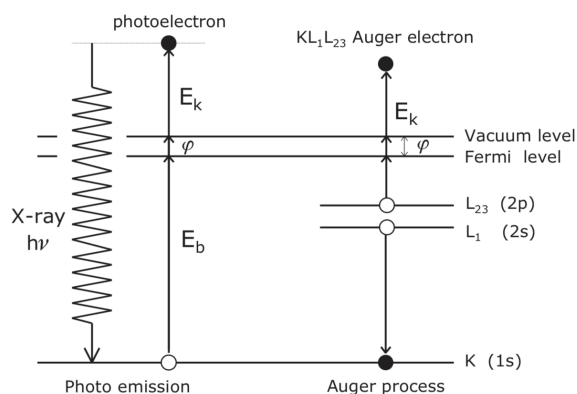


Figure 2.15: Photoemission and the Auger process [8]

In principle XPS can be used to analyze all elements in the periodic table, however, hydrogen and helium cannot be detected due to low cross-section of interaction. Conventional XPS lacks spatial resolution with analyzed areas of several square millimeters. Yet modern instruments are now capable of resolutions in the micrometer range. Similarly, to other spectroscopic methods, intensities of the signal may vary up to 10 % wherefore the use of an internal standard is recommended to decrease inaccuracy below 10 % [58].

2.5.8 Fourier-transform infrared spectroscopy (FT-IR)

In spectroscopical methods, described in previous sections (XRF, EDX, XPS), transitions between electronic energy levels are stimulated. The high energy thresholds for inner orbital to be excited or to be ejected correspond to high energy radiation such as x-radiation. The energy of infrared radiation on the other hand is much less energy intensive, stimulating only energy levels between vibrational states of a molecule. Whereas even lower energy radiation, such as microwaves stimulate rotational states. Vibrational spectroscopy as IR is only partially suitable for analysis of chemical composition. It constitutes, however, a powerful tool to identify adsorbed species and to study the way in which these species are chemisorbed on the surface of the catalyst.

For a molecule to show infrared absorption it must possess an electric dipole moment that changes during vibration. This selection rule for IR absorption is satisfied by heteronuclear diatomic molecules, such as *CO* and *NO*. The dipole moment of such molecules changes as the bond expands and contracts. In contrast, homonuclear diatomic molecules are infrared inactive as the dipole moment is zero no matter the elongation of the bond. Whereas, a diatomic molecule exhibits only one vibrational mode a non-linear molecule A-B-A shows three vibrational modes, two of which corresponding to stretching motions and one bending motion. A linear molecule type B-A-B has four vibrational modes, two of which correspond to bending motion and in addition one symmetrical and one asymmetrical stretching motion. Yet, not all vibrations are IR active (i.e. symmetrical stretching in linear triatomic molecules) for only motions where the dipole moment is altered absorb infrared radiation [64], [8].

The stiffness of the bond, characterized by the force constant k and the masses of the attached atoms determine the frequency of the vibrations and thus consequently also the frequency of absorbed radiation. The reduced mass μ provides a useful way to simplify calculations and is presented as follows:

$$\mu = m_1 m_2 / (m_1 + m_2) \quad (2.24)$$

As a result, the equation relating the force constant, reduced mass and frequency of absorption (in cm^{-1}) can be written as:

$$\tilde{\nu} = (1/2\pi c) \sqrt{(k/\mu)} \quad (2.25)$$

where c is the speed of light.

Since the energy levels that can be occupied by molecules are quantized, as are vibrational energy states, a molecule can only absorb radiation of the same energy as the exact difference between the fundamental modes of vibration of the molecule. Transition between vibrational levels occur by absorption of photons with frequencies in the infrared range (wavelengths 1 - 1000 μm , wavenumbers 10.000 - 10 cm^{-1} , energy differences 1240 - 1.24 meV). The obtained absorption bands in IR spectra correspond to these energy differences in vibrational modes. These bands are more intense the larger the induced change in the dipole moment of the molecule. Complications in evaluation of IR spectra arise due to the overlapping of individual bands and the appearance of additional bands, e.g. overtone and combination bands. Multiples of the fundamental absorption frequencies are called overtone bands and correspond to excitations to the second (or higher) following energy state. By implication

will the first overtone appear in the spectrum at twice the wavenumber as the fundamental. Combination bands emerge when two fundamental bands absorbing at $\tilde{\nu}_1$ and $\tilde{\nu}_2$ absorb energy simultaneously. The resulting band will appear at $(\tilde{\nu}_1 + \tilde{\nu}_2)$ wavenumbers.

Molecules in gas phase have additionally to vibrational also rotational freedom, and the vibrational transitions are accompanied by rotational transitions. Only visible in high resolution spectra this vibration-rotation bands are characterized by fine structures and appear in two branches, see Figure 2.16. Upon adsorption, the molecule loses its rotational freedom and only broad vibrational transition bands are observed. The frequency, however, is shifted. First of all, mechanical coupling of the *CO* molecule to the heavy substrate increases the *C – O* vibration frequency. Secondly, the chemisorption alters the distribution of electrons over the molecule and thus weakens the *C – O* bond. These effects, i.a. contribute to a shift of absorbance bands, usually towards higher frequencies (lower wavenumbers) for the adsorbed species [8], [64], [65].

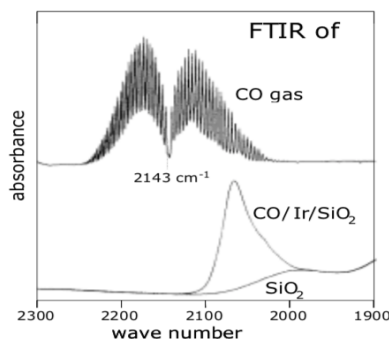


Figure 2.16: The infrared spectrum (wavenumbers in cm^{-1}) of CO in gas phase and adsorbed on an *Ir/SiO₂* catalyst [8]

In terms of experimental methods for IR spectroscopy a great variety of techniques has been developed. The heart of every spectroscopic method is the spectrometer, that shows the intensity, in this case of infrared radiation, as a function of frequency, wavelength or energy. The predominant spectrometer today are Fourier-transform infrared spectrometers. It is based on the interference of radiation of two beams to produce an interferogram out of polychromatic radiation. The interferogram is then passed through the sample before it reaches the detector. The interferogram comprises all information from all wavelengths and by the mathematical method of Fourier-transformation the signal is converted back, presenting the original information of absorbance for each wavelength. The advantage of FT spectrometers is that radiation from all wavelengths is measured simultaneously, rather than consecutively. As a result, higher throughput is possible at also higher signal to noise ratios [64], [65].

Besides different instrumentation for obtaining IR spectra, i.e. spectrometers, a selection of measurement techniques is available.

Transmission

Transmission spectroscopy is the oldest and most straightforward infrared method, where not only solids but also gases and liquids can be measured. As the infrared radiation passes through the sample cell certain frequencies are absorbed, specific to the analyte.

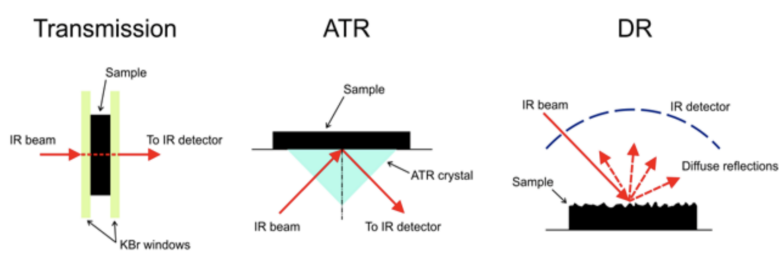


Figure 2.17: Infrared spectroscopy techniques, from left to right: transmission, attenuated total reflectance (ATR) and diffused reflectance (DR) [14]

Employed window material of the sample cell sets the usable transmission range. The standard material is *KBr* with a range of $43500 - 400 \text{ cm}^{-1}$. After leaving the sample cell the IR beam is guided to the detector as illustrated in Figure 2.17 (left).

In conclusion, transmission spectroscopy represents the most sensitive technique to study adsorbed species on a solid catalyst. Sample preparation for solid samples is however sometimes problematic. The sample has to be finely ground and pressed to a disc, while the resulting heat and friction may alter the sample. Furthermore, the discs must not be too thick to ensure a sufficiently high signal and not too thin as they may break [64], [65].

Attenuated total reflectance

Attenuated total reflectance (ATR) spectroscopy utilizes the phenomenon of total internal reflection of radiation inside an optical dense crystal. The beam will undergo total reflection at the interface between the optical dense medium (ATR crystal) to the optical rare medium (sample) when the angle of incidence exceeds a critical value. As the electromagnetic wave cannot be discontinuous at a boundary it propagates a fraction of a wavelength beyond the reflecting surface. This so-called evanescent wave, when close enough to a material can be selectively absorbed just as a regular light wave. The depth of penetration is a function of the wavelength, the refractive index of the ATR crystal and the angle of incidence.

Different designs of ATR cells allow examination of both solid and liquid specimens. The limited path length through the sample is advantageous as it allows a study of near surface layers. Also the investigation of aqueous solutions can be carried out that are otherwise inaccessible for transmission IR. Furthermore, the design of continuous flow chambers makes in-line monitoring of chemical processes possible. Despite multiple advantages, is the ATR technique not suitable for detecting adsorption of reactants on a solid surface [64], [65].

Diffuse reflectance

At optically scattering interfaces (inhomogeneous samples like powders) with roughness down to the range of the wavelength incident light may be partly reflected regularly, partly scattered diffusely, and partly enter the substrate. The entered part of radiation is scattered at various grains and is transmitted through grains of powder where the analytes specifically absorb IR frequencies. In the Mid-IR range, diffuse reflectance, however, is very weak and was made realizable only as FT-IR spectrometers became available, hence the name DRIFTS, diffuse reflectance infrared Fourier-transform spectroscopy.

The diffusely reflected IR radiation is usually collected by large ellipsoidal mirrors, to collect as much reflected beams as possible.

Virtual no sample preparation is required for DRIFT spectroscopy that could falsify properties of powder catalysts. As in transmission operation, DRIFTS is carried out in chambers where the interactions of different atmospheres with the sample can be studied. Further, it allows the measurement of high scattering or absorbing specimen such as textiles, foams or paper [64], [65], [66].

2.5.9 Raman spectroscopy

When electromagnetic radiation interacts with matter it can either be absorbed (and possibly initiate succession processes i.a. fluorescence) or be scattered. Scattering occurs when a particle is illuminated by an electromagnetic wave and electrons in the particle are set in oscillatory motion by the electric field of the incident wave. The resulting oscillating dipole moment develops with a magnitude proportional to the polarizability of the particle and the strength of the electric field. These accelerated electric charges emit electromagnetic waves radially into all directions, and this secondary radiation is called “the radiation is scattered by the particle”.

If the particle is perfectly homogeneous, as in a perfect crystal, the scattered waves interfere destructively in all directions except the direction of propagation of the exciting radiation, i.e. specular reflectance on mirrors. Waves (with adequate wavelengths) scattered at different levels in a crystal lattice may further interfere constructively to give diffraction patterns as is foundation for XRD measurements. If the medium is inhomogeneous, however, as in an imperfect crystal, a solution of macromolecules or a gas, radiation is scattered into other directions as well. Consequently, many phenomena that are not denoted scattering are in fact ultimately a result of scattering.

Contrary to absorption, scattering of light does not require photons that match an energy gap corresponding to a difference between the ground state of a molecule and the excited state. As the electronic geometry gets distorted by the incident wave it is polarized. The shape of the distorted electronic geometry is defined by the frequency (i.e. the energy) of the incident light and therefore does not correspond to electronic states of the particle or molecule. As a result, this very short-lived “state” is often called a virtual state. The distortion or polarization of the electronic geometry relaxes by emitting the secondary radiation. The most intense form of scattering, Rayleigh scattering, occurs when the electron cloud relaxes without any nuclear movement. This is essentially an elastic process and there is no appreciable change in energy wherefore the secondary radiation shows the same frequency as the incident radiation. Rayleigh scattering is observed at all particles much smaller than the wavelength of the radiation. This phenomenon also causes the sky to appear blue, as blue light is more effectively scattered at nitrogen molecules than other wavelengths.

Albeit much less probable, the electron cloud may also relax inelastically, emitting light with frequencies differing from the incident light. This process referred to as Raman scattering is a much rarer event which involves only one in 10^7 of the photons scattered. This occurs when the light and the electrons interact and the nuclei begin to move at the same time. Since the nuclei are much heavier than the electrons, there is an appreciable change

in energy of the molecule to either lower or higher energy depending on whether the process starts with a molecule in the ground state (Stokes scattering) or from a molecule in a vibrationally or rotationally excited state (anti-Stokes scattering). As a consequence, incident radiation collects energy from the molecule (anti-Stokes) or loses energy to the molecule (Stokes) as illustrated in Figure 2.18. Comparable to personal life, one more easily loses than wins something, similarly in light scattering the Stokes scattering is more probable. Consequently, Raman spectra comprise only the more intense Stokes scattering since Stokes and anti-Stokes scattering are equivalent in information content.

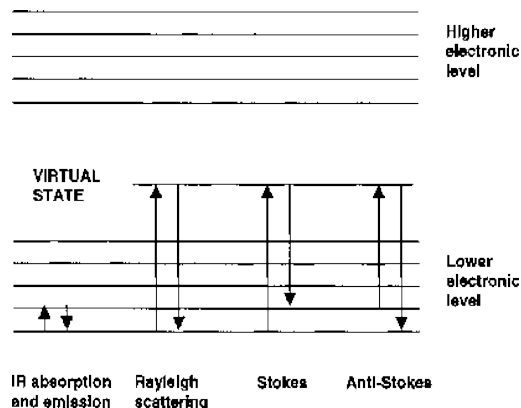


Figure 2.18: Transitions between vibrational states of molecules involved in Raman and IR spectroscopy [15]

While in infrared spectroscopy a range of frequencies is directed onto the sample where specifically frequencies are absorbed, in Raman spectroscopy only one frequency but with high intensity is used. In a typical Raman spectroscopy experiment, a monochromatic incident laser beam of visible light is passed through the sample and the radiation scattered from the front face of the sample is monitored. This detection geometry allows the study of gases, pure liquids, solutions, suspensions, and solids. The obtained spectrum is the plot of intensity versus Raman shift, that is the shift relative to the incident laser frequency. As in the case of the IR spectrum, the features of a Raman spectrum (number of Raman bands, their intensities and their shapes) are directly related to the molecular structure of a compound.

The gross selection rule for vibrational Raman transitions is that the polarizability should change as the molecule vibrates. This is in complete contrast to infrared absorption where a dipole change in the molecule gives intensity of the absorption band and, at a very simple level, this means asymmetric rather than symmetric vibrations will be intense. However, as homonuclear and heteronuclear diatomic molecules swell and contract during a vibration, the control of the nuclei over the electrons varies, and hence the molecular polarizability changes. Whereas only heteronuclear diatomic molecules are IR active, both types of diatomic molecule are vibrationally Raman active. Figure 2.19 compiles the vibrational modes of CO_2 as an example of a triatomic molecule and further illustrates the rule of thumb: symmetric vibrations are Raman active and asymmetric vibrations are IR active [29], [65],[67], [68].



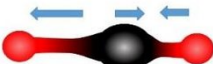
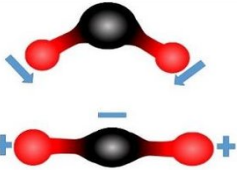
Vibrational mode	Molecular structure	IR and Raman activity
Equilibrium structure		No activity at equilibrium position
Symmetrical stretch		$\partial\mu/\partial Q = 0$ IR inactive $\partial\alpha/\partial Q \neq 0$ Raman active $\omega = 1388 \text{ cm}^{-1}$
Asymmetrical stretch		$\partial\mu/\partial Q \neq 0$ IR active $\partial\alpha/\partial Q = 0$ Raman inactive $\omega = 2349 \text{ cm}^{-1}$
Bending		$\partial\mu/\partial Q \neq 0$ IR active $\partial\alpha/\partial Q = 0$ Raman inactive $\omega = 667 \text{ cm}^{-1}$

Figure 2.19: Vibrational modes of CO_2 , a triatomic linear molecule, and the corresponding IR/Raman activities in wavenumbers [16]

As illustrated in Figure 2.19 a molecular vibration is IR active if the dipole moment μ , permanent or induced, changes during the vibration, and it is Raman active when the polarizability α of molecules changes during vibration. As a result, Raman and IR spectra complement each other for not every vibration evokes a signal in both methods.

One of the main issues concerning Raman spectroscopy are fluorescent samples. Broad and intense fluorescence peaks mask other peaks of the sample. Moreover, it is important to consider the differing Raman scattering intensities of the analytes and the surrounding matrix as well as possible contamination. If an impurity is a strong Raman scatterer the impurity may dominate the obtained spectra and lead to wrong conclusions. To give an example: When a bottle is filled with sulphur only the sulphur bands will be observed as the polyethylene is a much weaker Raman scatterer. On the upside, water is a strong absorber of infrared radiation as well as glass. Both are weak scatterers in Raman spectroscopy, which makes the technique particularly suitable for samples in aqueous solutions or glass containers.

Raman spectrometers are often coupled with microscopes to examine the specimen and focus the laser on specific areas. Since visible light is easily focused by glass lenses the theoretical spatial resolution is up to $1 \mu m$, referred to as the diffraction limit. The high spatial resolution, and the use of automated stages, enables mapping and imaging experiments to be carried out relatively easily. However, representative spectra for inhomogeneous samples is often hard to obtain as different spots may produce very different spectra [67].

2.5.10 Method comparison

The analytical methods presented in this chapter each offer valuable information about the examined olivine and feldspar bed materials with formed ash layers. The techniques differ, however, in gathered information to complement and corroborate each other. Moreover, the detected medium (such as light in different frequencies or electrons) differs from method to method. Similarly, the techniques rely on excitation of the specimen either by electromagnetic radiation ($h\nu$) or by electron bombardment (e^-) as is summed up in table 2.1.

Table 2.1: Analytical techniques used in this work tabulated by means of detection and excitation

Detection	Excitation	
	e^-	$h\nu$
e^-	SEM	XPS
$h\nu$	EDXS	XRF, XRD UV/VIS, IR, Raman

Figure 2.20 illustrates the lateral resolutions and the detection range of each applied method. The wide spot size of XRF corresponds, together with XRD, to the high penetration potential of x-radiation, constituting bulk analysis methods. Characteristic x-radiation produced by electron excitation as used in EDX (sometimes referred to as WDS - wavelength dispersive spectroscopy) originates from depths around $50 \mu\text{m}$. It characterizes together with Raman as an intermediate technique between bulk and surface analysis. The relatively large spot size of XPS demonstrates a poor lateral resolution, however, since photoelectrons are generated with low energies only the outermost 1 nm of the sample yield elemental and chemical information.

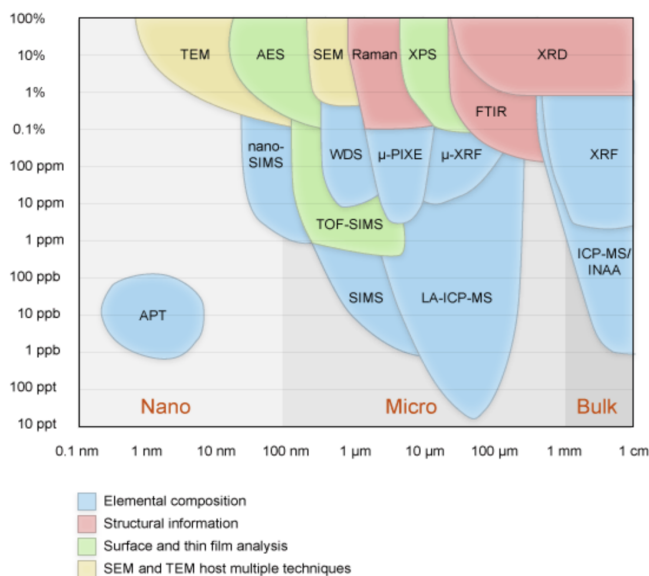


Figure 2.20: Visualization of analytical dimensions for principal microanalysis tools; the x-axis shows the electron or light spot size whereas the y-axis demonstrates the detection limit [17]

Materials and methods

3.1 Studied bed material

3.1.1 Olivine

The focus of this study is on Olivine and K-Feldspar bed materials where layers of ash formed, cf. section 2.4.1. Fresh or unused Olivine mineral ($(Fe, Mg)_2SiO_4$) was provided by the Senden gasification plant and sieved to a particle size of 200-250 μm as a reference to used Olivine.

The used Olivine samples were collected in preceding works [69] from the DFB gasifier power plant in Senden, Germany using logging residues as fuel. The power plant is designed for a fuel power of 15 MW_{th} , generates electricity of about 5,1 MW_{el} and district heating of about 6.4 MW_{th} . Logging residues include cut-off root ends, tops, and branches. This lower-cost feedstock comprises on average 15 % of bark and 15 % of needles as a consequence, only 70 % of the used fuel is wood chips. A few kilograms of sample were drawn from the very bottom of the combustion reactor after an operation time of around 1200 h without cooling down. The decisive property of the fuel for ash layer formation is its ash content. The determination is standardized internationally (CEN/TS 14 775 /9-46/) and follows defined heating procedures.

Table 3.1: Elemental composition (expressed as oxides) of wood ash from literature and XRF measurements for fuel ash from the Senden gasifier and used Olivine bed material

Compound	Literature [3] (wt%)	Feedstock ash average [69] (wt%)	Bedmaterial average [69] (wt%)
Na_2O	1	0.8	2.2
MgO	6	5.0	39.5
Al_2O_3	n.a.	3.3	0.9
P_2O_5	n.a.	4.8	0.3
SO_3	n.a.	2.9	0.1
SiO_2	n.a.	13.4	34.3
K_2O	6	12.6	0.7
CaO	42	55.6	13.8
Fe_2O_3	small amounts	0.7	6.8
<i>Others</i>	n.a.	0.8	0.8

Wood exhibits, compared to all other biogenic fuels, with around 2 % to dry mass the lowest ash content and bark around 4 % [3]. Besides organic residues wood ash predominantly

comprises CaO , K_2O , MgO and P_2O_5 . Table 3.1 lists typical literature ash composition contrasting measurements of fuel ash and Olivine bed material with ash deposits from the Senden gasifier [69].

3.1.2 K-Feldspar

The fresh K-Feldspar ($KAlSi_3O_8$) endmember was also sieved to a particle size of 200-250 μm to be used as a reference. The purest available K-feldspar presented a remaining quartz content of 4 %.

Similarly to used Olivine, the used K-Feldspar samples stem also from previous research [70] where in a bench-scale fluidized bed reactor bark and chicken manure were combusted. Approximately 500 g of bed material was filled into the 5 kW and 0.7 $kg h^{-1}$ of fuel was fed up to 40 h of operating time, ranging between 730 and 830 °C. The combustion of pure chicken manure and pure bark, however, had to be stopped ahead of time. The chicken manure combustion lead to agglomeration of the fluidized bed after 11 hours, the bark combustion was halted after 36 hours due to operational problems. Only the mixture of 70 % bark and 30 % chicken manure was completed as planned. Samples were drawn from the reactor after certain intervals to undergo further examination. It was shown that ash layers grew with time with a strikingly high calcium content, higher than would be expected just by ash deposit. Moreover, phosphorus and magnesium was detected by EDS measurements [70].

For this work used bed material grains were sieved to a particle size 200-250 μm and the ash deposits of following fuels investigated:

- Pure chicken manure sampled after 8 hours (CM8h)
- Pure bark sampled after 8 hours (B8h)
- Pure bark sampled after 32 hours (B32h)
- A blend of 70 % bark and 30 % chicken manure sampled after 8 hours (Mix8h)
- A blend of 70 % bark and 30 % chicken manure sampled after 40 hours (Mix40h)

The ash content of these fuels was determined following DIN 14775 but at a temperature of 550°C. Table 3.2 shows the elemental distribution of the fuel ash as determined by [70]. The ash elemental composition of the blend lies between the two pure fuels. Only a higher calcium content was measured for the blend compared to the pure fuels.

Table 3.2: Elemental composition derived by XRF of ash from bark, chicken manure and the blend of 70% bark and 30% chicken manure, derived from [70]

	B (wt%)	CM (wt%)	Mix (wt%)
Total ash content	8.1	25.4	13.5
Na	4.8	7.9	5.5
Mg	5.6	14.2	11.0
Al	20.8	1.8	7.2
P	2.4	24.9	14.8
S	2.4	5.3	3.0
Cl	0.8	6.3	3.0
Si	42.4	5.3	19.8
K	3.2	7.9	5.9
Ca	12	25.8	27.4
Fe	5.6	0.7	2.5

3.2 Analytical equipment

This work comprises measurements carried out at the Jagiellonian University in Kraków and at TU Wien in Vienna.

UV-VIS

Kraków: The UV-VIS diffuse reflectance spectra for Colorimetry were collected by an AvaSpec-ULS3648 high-resolution spectrometer (Avantes BV, Apeldoorn, The Netherlands). The sample was illuminated by an AvaLight-D(H)-S Deuterium-Halogen Light Source (Avantes BV) that covers a spectral range of 200 - 1000 *nm*. As black reference black current was used after the lamp was switched off and the sensor blocked. As white reference served Sarspec DRSTD98.

The collected UV-VIS spectra were subsequently transformed into points in the color space chromaticity diagram via the add-in “Chromaticity” v1.1 1/2/2019 for Originlab (Northampton, Massachusetts, USA).

SEM-EDS

Vienna: The surface morphology assessment was carried out with a scanning electron microscopy equipment (FEI Company Quanta 200, Hillsboro, OR, USA). Prior to analysis, the samples were applied onto a graphite band and degassed at 10 *mA* and 0.1 *mbar* for about 30 seconds. The acceleration voltage ranged between 0.2 - 30 *kV* and were typically set to 20 *kV* that yielded the best images, measurements were operated in “low vacuum mode” at 80 *Pa*. Secondary electron images were measured by the installed Large Field Detector (LFD) and backscattered electron images by a Solid State Backscattered Electron Detector SSD-BSD (Dual BSD). The in the images shown WD value indicates the distance between sample to the blend and HFW displays the image size. EDS spectra were collected with an EDAX Genesis detector.

BET surface area

Krakòw: N_2 -sorption at $-196^\circ C$ was carried out using a 3Flex v1.00 (Micromeritics) automated gas adsorption system. Prior to the analysis, samples were degassed under vacuum at $350^\circ C$ for 24 h. Sample weights amounted to 300 mg.

Vienna: BET Surface area analysis was conducted with a micromeritics ASAP 2020 V4.00 and N_2 -sorption at $-196^\circ C$. Prior to analysis the samples were degassed under vacuum at $350^\circ C$ for 480 min. Analyzed sample weights amounted to around 1000 mg.

The specific surface area of the samples of both equipments was determined using the BET (Braunauer-Emmett-Teller) model according to the recommendations of Rouquerol et al.. The mesopore volume was calculated from the desorption branch using the BJH model (Kruk-Jaroniec-Sayari empirical procedure) in the range of 1,7 – 300 nm. The experiments allowed the specific surface area and pore volumes of the prepared catalyst samples to be determined.

XRF

Krakòw: A Tracer III-SD from Bruker was used for XRF measurements, equipped with a silicon detector (10 mm^2 XFlash SDD, cooled with the Peltier system). The source of X-ray radiation was a rhodium lamp with a maximum voltage of 40 kV. The spectrometer was operated by the S1PXRF program, supplied by the manufacturer.

XRD

Krakòw: X-ray diffraction data for all prepared samples was collected using a Panalytical Xpert Pro Diffractometer (Almelo, The Netherlands) equipped with monochromatised $Cu\ K\alpha$ radiation ($\lambda = 1.54\text{ \AA}$). Analysis was carried out in the scan range from 5° to $65^\circ\ 2\theta$ with a scanning step of $0.02^\circ\ 2\theta$. The samples were measured without further preparation as grains. XRD analysis software Highscore by Malvern Analytical (Malvern, United Kingdom) was used for peak assignment and based on the elemental information derived by XPS and XRF.

XPS

Krakòw: X-ray Photoelectron Spectroscopy was performed using the ESCA Prevac spectrometer equipped with a hemispheric analyser of charged particles XPS and AES (VG Scienta R3000), an X-ray tube equipped with two anticathodes Mg/Al (power $Mg/Al = 400/600\text{ W}$) and the X-ray monochromator with the radiation source (single anticathode - Al). Each XPS spectrum was calibrated to the carbon component $C1s$ binding with energy of 285.0 eV . The fitting of high resolution spectra was done in CasaXPS software. All XPS measurements were performed directly without sample preparation.

FT-IR

Vienna: Transmission

IR spectra were recorded in transmission using a Bruker Vertex 70 spectrometer with an MCT detector. The samples were pressed to small discs and fixed in the IR cell. All infrared spectra were collected at a resolution of 4 cm^{-1} in the $4000\text{--}900\text{ cm}^{-1}$ range by averaging 128 scans to achieve good signal to noise ratios.

Kraków: DRIFTS, ATR

DRIFTS: The THERMO/Nicolet 8700 spectrometer equipped with a liquid nitrogen-cooled mercury cadmium telluride (MCT) detector was used for scanning in mid-IR range. The samples were placed without preparation in a Praying Mantis High-Temperature Reaction Chamber (Harrick Scientific Co., Ossining, NY) with *ZnSe* windows. The gas flow for adsorption experiments was set to 30 mL/min either *He* gas or the adsorbents (*CO*, *HAc*, *CH₃OH*, *NH₃*). Prior to analysis, was the sample annealed at 500°C in helium atmosphere. The instrument was controlled by OPUS v 8.0 software.

ATR: Further sample characterization was carried out by ATR measurements with Golden Gate ATR accessory (Specac Ltd., Orpington, UK) to the same spectrometer as for DRIFTS.

Raman

Kraków: Raman spectroscopy was performed at a LabRAM HR800 confocal Raman microscope (Horiba Jobinn Yvonne, France). Possible employed laser lines: He-Ne (633 nm), diode (532 nm) and HeCd (325 nm), however, the red laser (532 nm) with 50 mW power yielded the best results and was almost always used. The catalyst and reference samples were loaded without preparation in a reactor cell Linkam-CCR1000 (Scientific Instruments Ltd, Waterfield, Surrey, England), fitted with quartz windows. Raman heating experiments were conducted with a 30 mL/min flow of helium gas in a high temperature reaction chamber (Harrick Scientific Co., Ossining, NY) with *SiO₂* windows. The laser signal was calibrated at a pure silicium specimen to 520 cm^{-1} Raman shift.

Research findings

4.1 Surface Morphology

4.1.1 Colorimetry

Easily recognizable, fresh K-Feldspar grains appear in a general white color with occasional small brown grains that are presumed impurities. The distinct white color of native K-Feldspar differs from the general brown tone of the other sample grains. Native olivine grains, however, denoted as Olivine fresh appears brighter compared and the Feldspar sample bark 8h appears particularly dark compared to the other samples. This observation is supported by the colorimetry analysis as depicted in figure 4.1.

CIE 1931

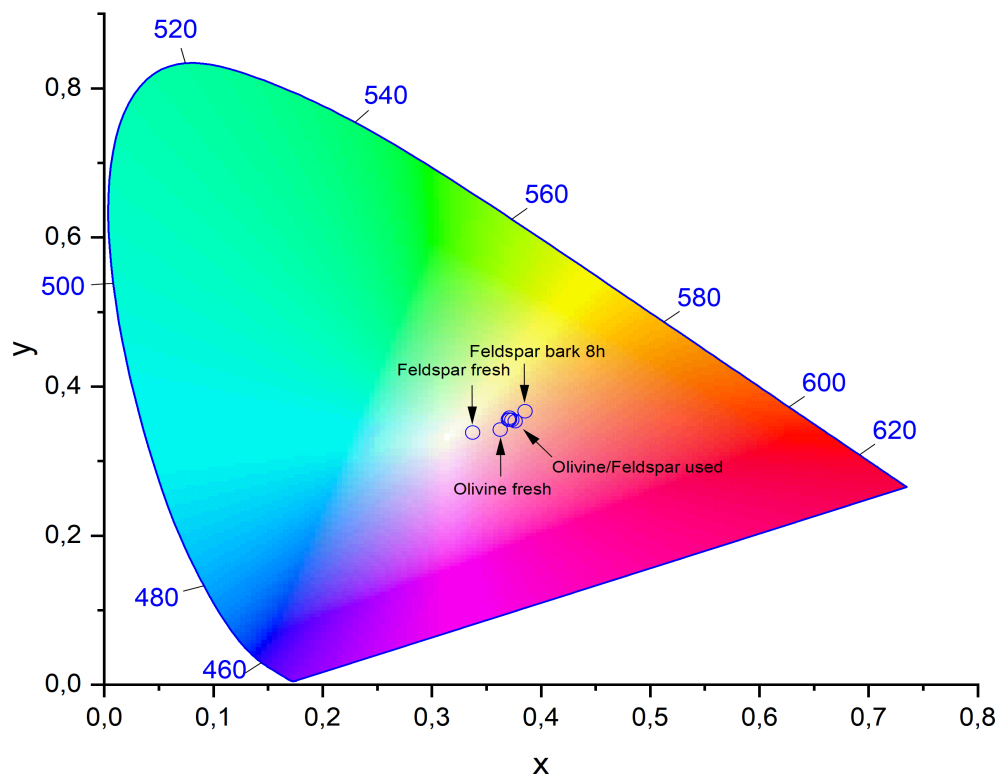


Figure 4.1: CIE 1931 color space chromaticity diagram with color points

4.1.2 BET surface area

The collected isotherms of all samples correspond to composite type II and IV isotherms and the lacking of a horizontal line close to $p/p^0 = 1$ indicates the absence of macropores. Only the Feldspar CM8h isotherm shows a slight step in the adsorption isotherm as well as in the consequential desorption curve. Moreover, all samples demonstrate a hysteresis loop indicating pores wider than 4 nm. The isotherm plots from measurements with sample weights of 1 g are set out in the appendix.

Table 4.1 compiles the results of the BET surface area assessments and indicate a surface area increase with reactor residence time. Olivine used shows the highest, Olivine fresh and Feldspar fresh the lowest surface areas. Particularly striking is Feldspar CM8h with a high surface area compared to samples of equal reactor times B8h and Mix8h. The two sets of experiments produce almost the same results and demonstrate a good reproducibility. Substantiated on the not measurable surface area of Olivine fresh it is assumed, however, that a higher sample mass of 1 g produces more reliable results. Moreover, the literature surface areas of Olivine and Feldspar minerals evidence a good experimental conduct and corroborate the experimental findings.

Table 4.1: Assessment of the BET surface area; measured with sample weights of about 1000 mg* and 300 mg** compared to literature values

Sample	BET surface area* m^2/g	BET surface area** m^2/g	Literature m^2/g
Olivine fresh	0.4	-	0.4[71]
Olivine used	4.6	4.6	
Feldspar fresh	0.4	0.3	0.1-0.3 [72]
Feldspar CM8h	1.4	0.8	
Feldspar B8h	0.4	0.6	
Feldspar B32h	0.9	0.8	
Feldspar Mix8h	0.9	0.8	
Feldspar Mix40h	2.1	1.6	

Also interesting are the average pore sizes of the samples, comprised in table 4.2. The results suggest a decrease in pore width with increasing surface area. Only Feldspar bark samples demonstrate a pore size increase compared to Feldspar fresh.

Table 4.2: Assessment of the BJH desorption pore size distribution measured with sample weights of about 1000 *mg*

Sample	Average pore width (<i>nm</i>)
Olivine fresh	14.5
Olivine used	7.2
Feldspar fresh	14.9
Feldspar CM8h	9.6
Feldspar B8h	34.8
Feldspar B32h	16.7
Feldspar Mix8h	10.8
Feldspar Mix40h	11.0

4.1.3 SEM imaging

Figures 4.2 - 4.9 show secondary electron images of the bed material grains and offer information about the surface texture. The shown particles were randomly chosen and are representative for the grain distribution of the samples only with some reservation as they varied in shape and size.

Overall, the pictures show grains ranging between 200-250 μm in diameter but also some debris becomes obvious next to the grains. The fresh minerals, as illustrated in figures 4.2 and 4.4, were found to have a rather rough surface texture at low magnification. On a microscopic level, however, the well organized crystalline structures of Olivine and Feldspar minerals shows. Little irregularities among this organized structure therefore makes the surface appear smooth at high magnification. In contrast to the fresh mineral grains the ash layered samples displayed in figures 4.3, 4.6 - 4.9, appear smooth at low magnification. Yet, a further magnification reveals a wide variety of surface irregularities that contribute to a surface area increase that is consistent with BET results in table 4.1.

The surface texture of Feldspar C8h fig. 4.5 is particularly irregular and much of fine debris was found next to the bed material grains, indicating a lower adhesion of the ash layer. Significant amounts of debris was spotted also in sample Mix8h and Mix40h although less compared to CM8h. Another peculiar feature is presented by Feldspar Mix8h fig. 4.6 where “needles” were found amongst the bed material grains. According to EDS measurements these needles consist of Silicon and Oxygen. The origin of these needles is presumed due to contamination by glass wool during the sampling process as no such needles were found among Feldspar Mix40h grains.

Backscattered electron images display no particular bright spots, indicating a homogeneous distribution of elements and thus an even ash layer formation. On some grains indications of a terrace structure can be found at high magnifications suggesting a consecutive ash layer growth. The surface structure of Feldspar B8h and B32h seems very similar whereas Mix8h and Mix40h differ in quantity of surface details. Mix8h exhibits a much more irregular surface already on low magnification compared to Mix40h that seems have a more even surface.

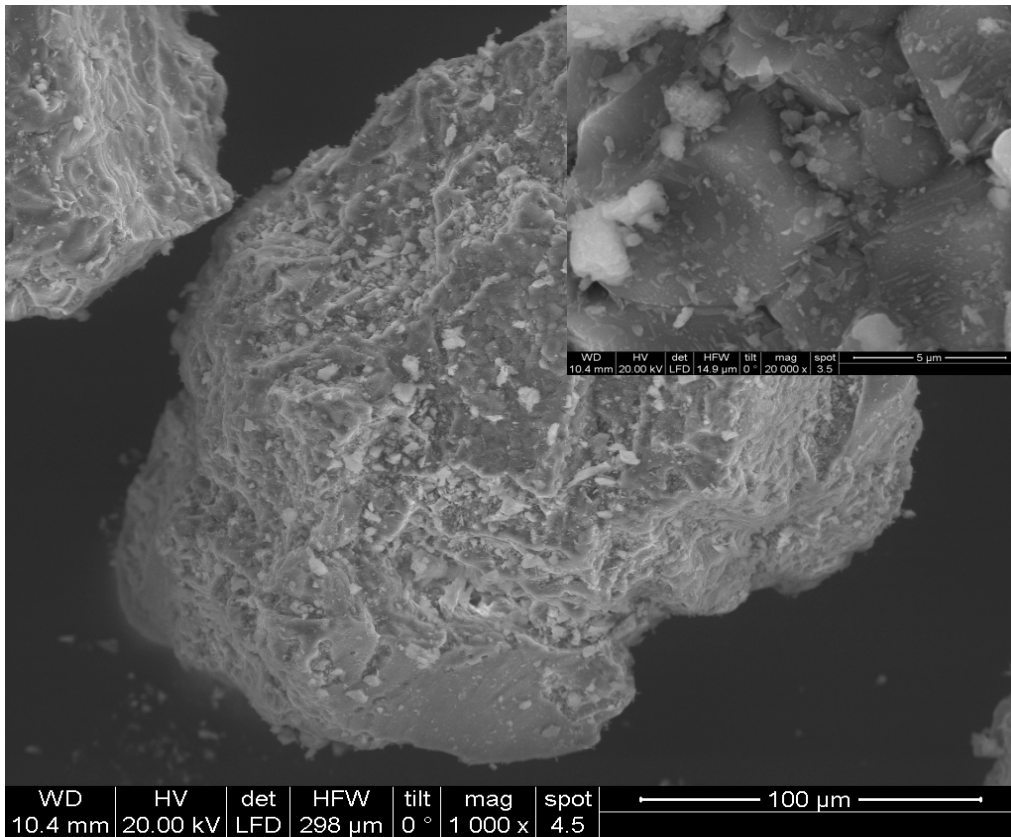


Figure 4.2: SE image of Olivine fresh and surface close-up

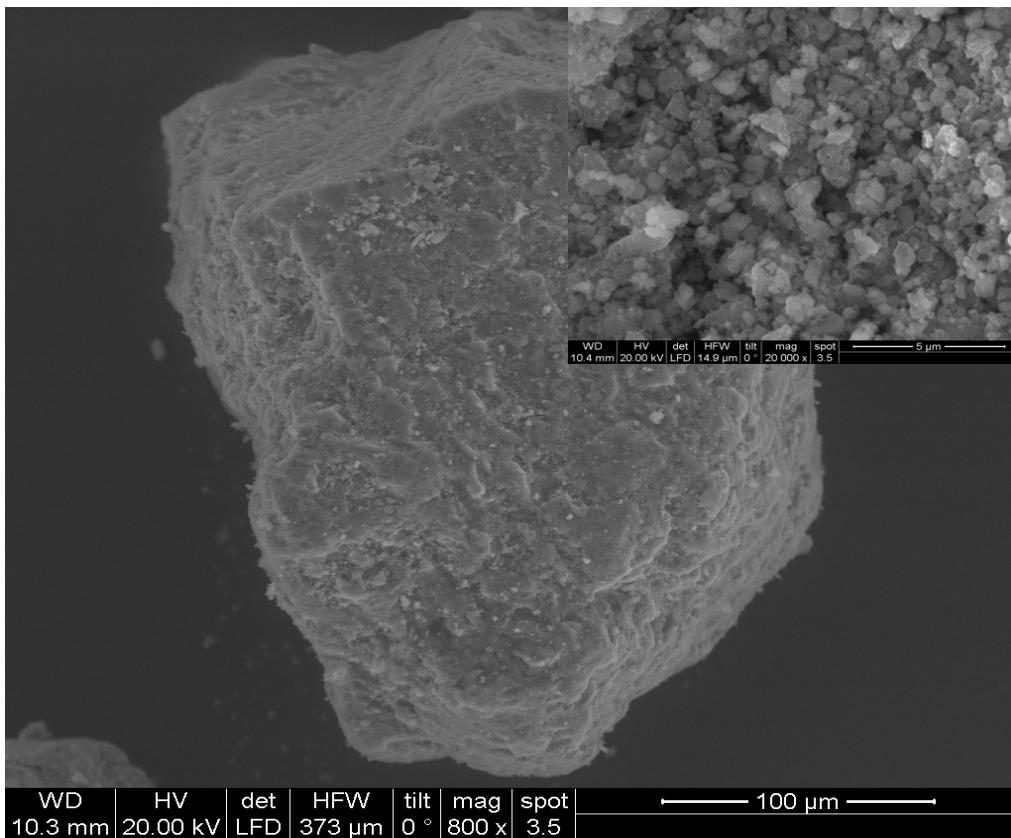


Figure 4.3: SE image of Olivine used and surface close-up

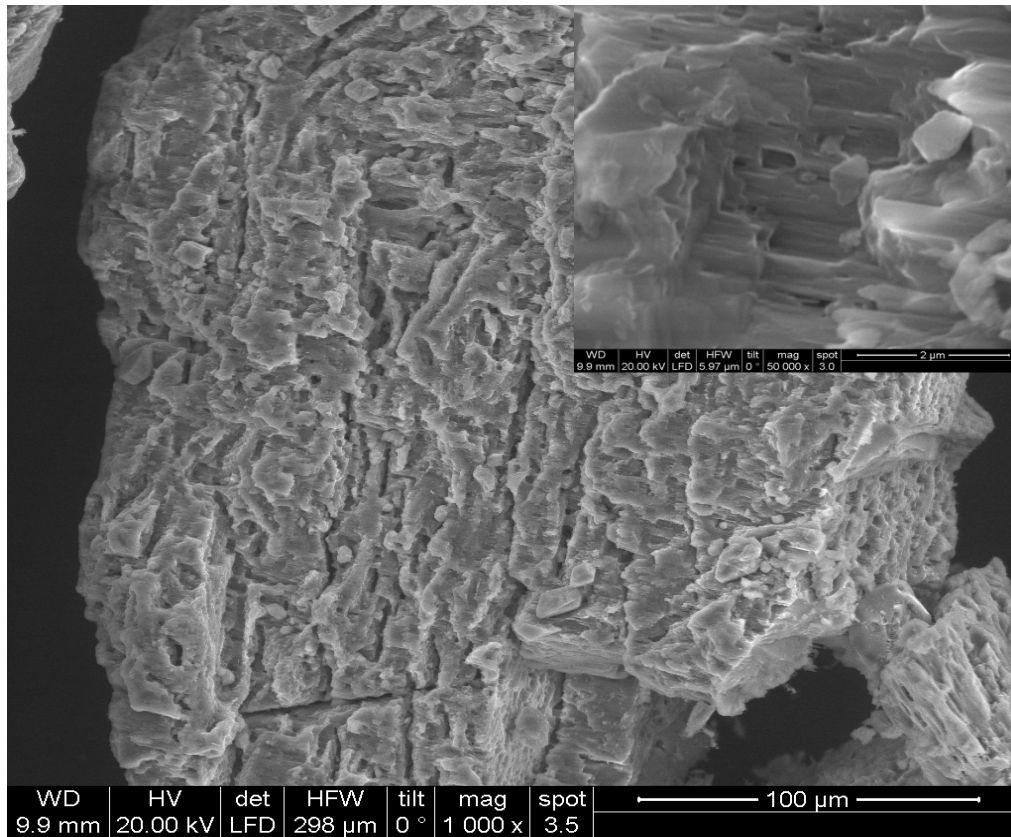


Figure 4.4: SE image of Feldspar fresh and surface close-up

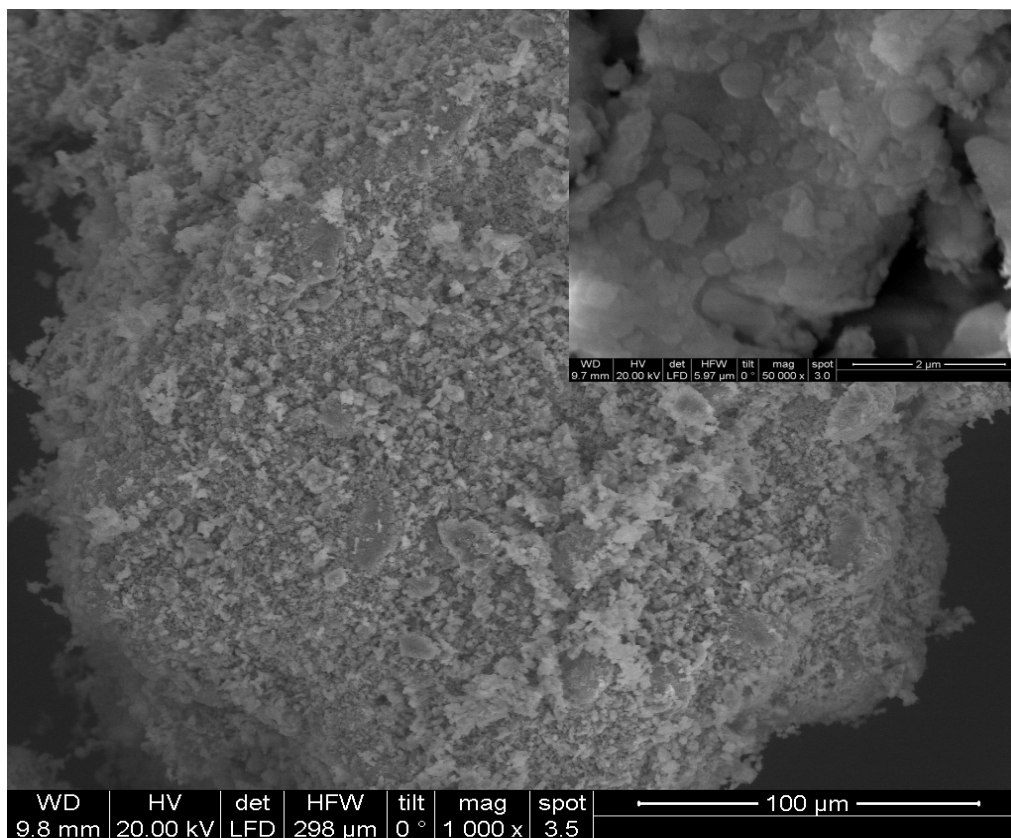


Figure 4.5: SE image of Feldspar CM8h and surface close-up

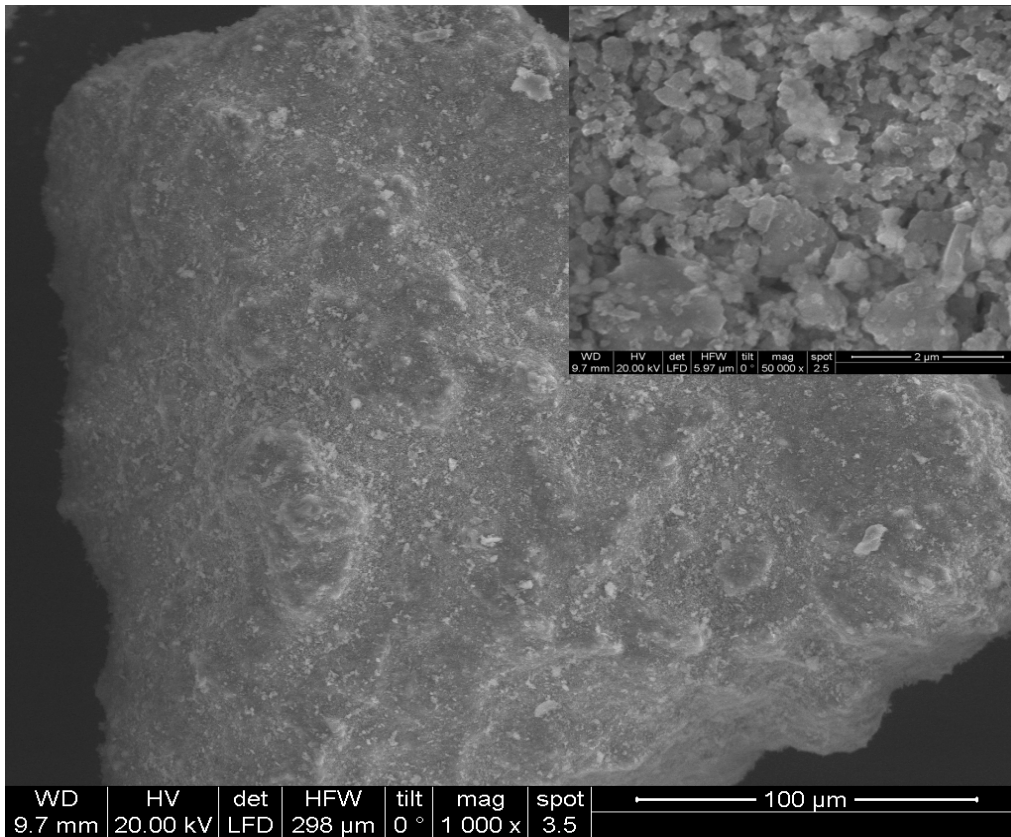


Figure 4.6: SE image of Feldspar B8h and surface close-up

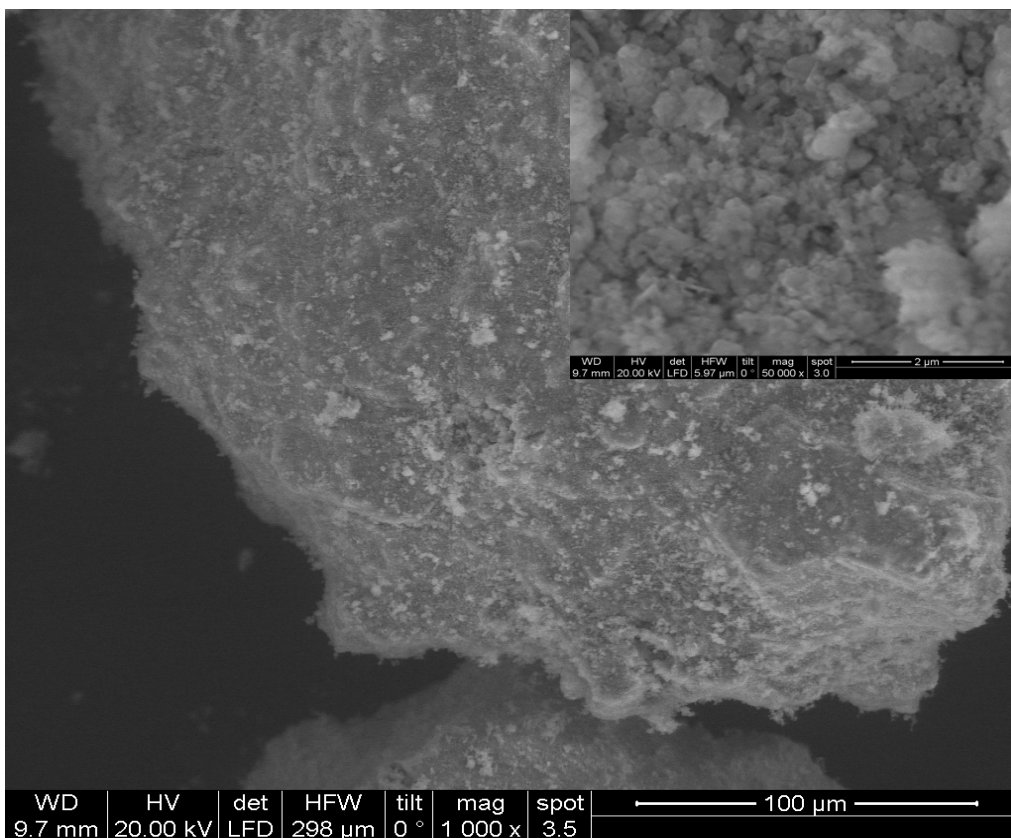


Figure 4.7: SE image of Feldspar B32h and surface close-up

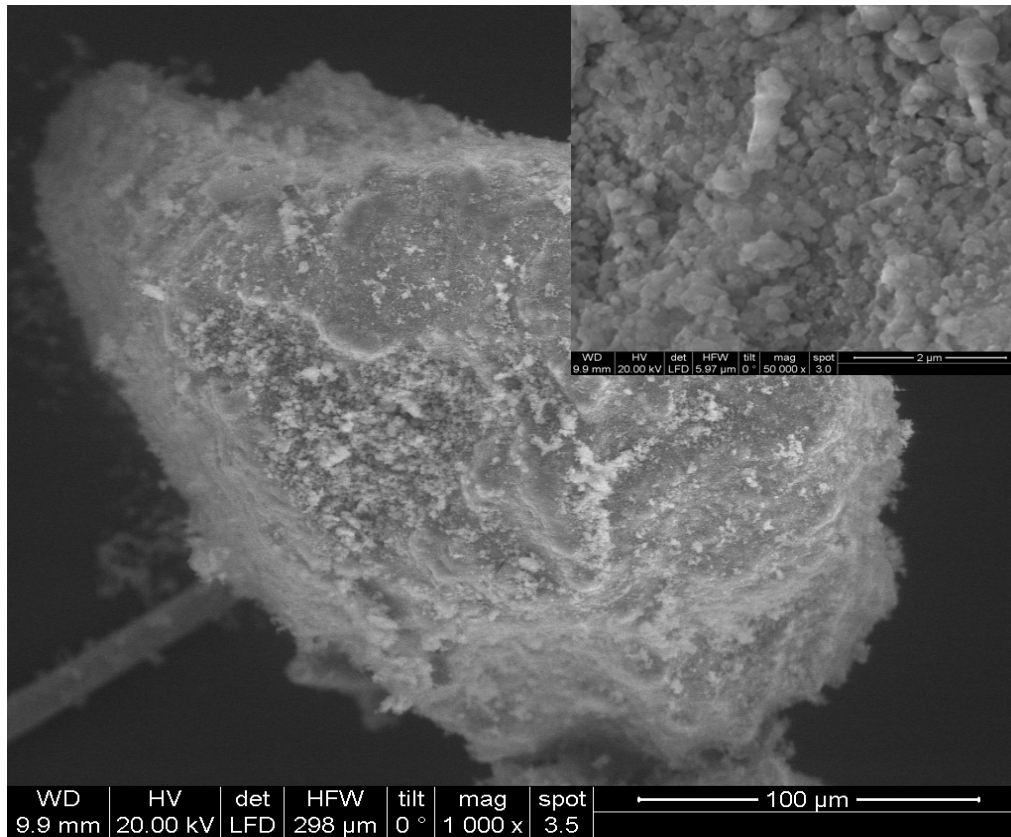


Figure 4.8: SE image of Feldspar Mix8h and surface close-up

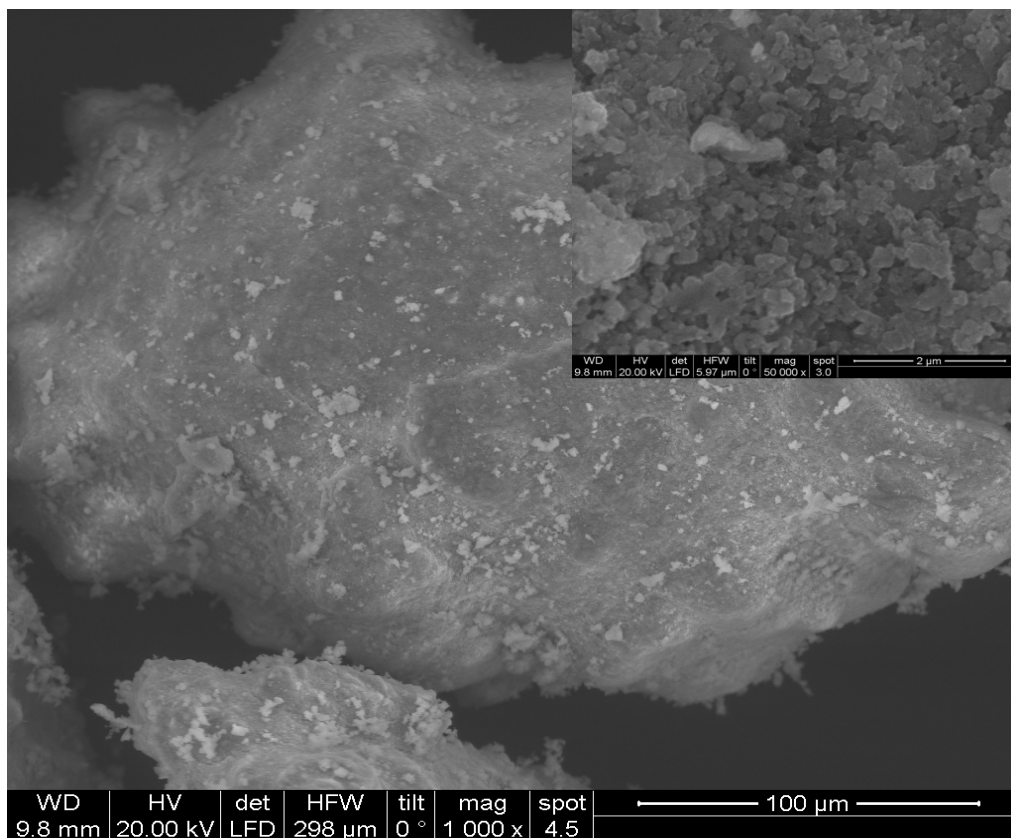


Figure 4.9: SE image of Feldspar Mix40h and surface close-up

4.2 Bed material composition

4.2.1 Surface properties: XPS and EDX

The composition of the outermost surface layer of a few nanometers is disclosed by XPS. Over a third of all samples surfaces is made up of oxygen as set out in Figure 4.10. In addition, the minerals Olivine and Feldspar exhibit significant amounts of silicon, 10 % and 18 % respectively. As expected, Olivine fresh shows a high concentration in both magnesium and iron compared to the other samples.

In contrast to Olivine fresh, Olivine used comprises almost no iron indicating the covering of the grains with a layer of fuel ash. All used samples present a high content of calcium > 15 % compared to the fresh mineral samples where calcium was found to be only 7 % for Olivine fresh and < 1 % for Feldspar fresh. Moreover, significant amounts of carbon were detected on all samples and phosphorus was found > 3 % in FF, CM8h, B8h, Mix8h and Mix40h. Negligible traces < 1 % of *Cr*, *Ni* and *Zn* were detected in Olivine used and B8h and B32h as well as *F* in Feldspar fresh and *Cl* in Olivine used and CM8h but are not included in Figure 4.10.

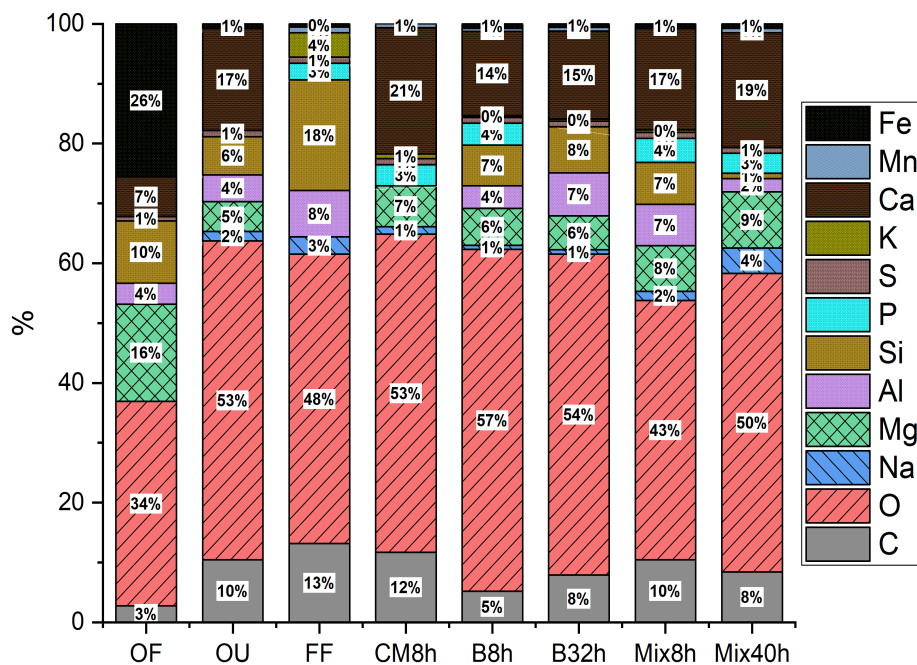


Figure 4.10: Elemental information derived by XPS measurements

The found carbon concentration in all samples, ranging between 3-13 % (the lowest with 3 % in OF and the highest of 13 % in FF), is to a significant amount due to exposure to air. This thin layer of carbonaceous deposits is known as adventitious carbon and comprises a variety of hydrocarbons [73].

Besides elemental information of the sample, XPS indicates further the electronic state of the element and thus the compound as which it occurs.

The exact position of the peak signals the electronic state of the element. Metallic calcium exhibits a binding energy of $345.8 \pm 0.8 \text{ eV}$ whereas the binding energy of calcium oxide is shifted towards higher energies. Interesting binding energies are listed in the following [73]:

- $Ca\ 2p_{3/2}$ in CaO : $346.6 \pm 0.5 \text{ eV}$
- $Ca\ 2p_{3/2}$ in $CaCO_3$: $347.1 \pm 0.3 \text{ eV}$
- $Ca\ 2p_{3/2}$ in $CaHPO_4$ and $Ca_3(PO_4)_2$: $347.5 \pm 0.2 \text{ eV}$
- $O\ 1s$ in FeO_x : $\sim 530 \text{ eV}$
- $O\ 1s$ in $(PO_4)^{-2}$: $531.0 \pm 1.0 \text{ eV}$
- $O\ 1s$ in $(CO_3)^{-2}$: $531.3 \pm 0.3 \text{ eV}$
- $O\ 1s$ in SiO_2 : $532.9 \pm 0.4 \text{ eV}$
- Elemental P : $130.2 \pm 0.3 \text{ eV}$
- $P\ 2p_{3/2}$ in $(PO_3)^{-}$: $134.6 \pm 0.5 \text{ eV}$
- $P\ 2p_{3/2}$ in $(PO_4)^{-3}$: $133.2 \pm 0.7 \text{ eV}$
- $P\ 2p_{3/2}$ in $CaHPO_4$: $133.2 \pm 0.7 \text{ eV}$
- $P\ 2p_{3/2}$ in $ZnPO_4$: 134.0 eV

Apart from the shift in binding energy, the detected peaks may be a composite of a plurality of individual peaks and have to be fit manually. Figure 4.11 displays the high resolution scans of the $2p\ Ca$ peaks with fitting. The fitting was done to minimize the error and to optimally represent the measurement points with typical FWHM (full width at half maximum) of 1.7; 2.8 and 3.2 [74].

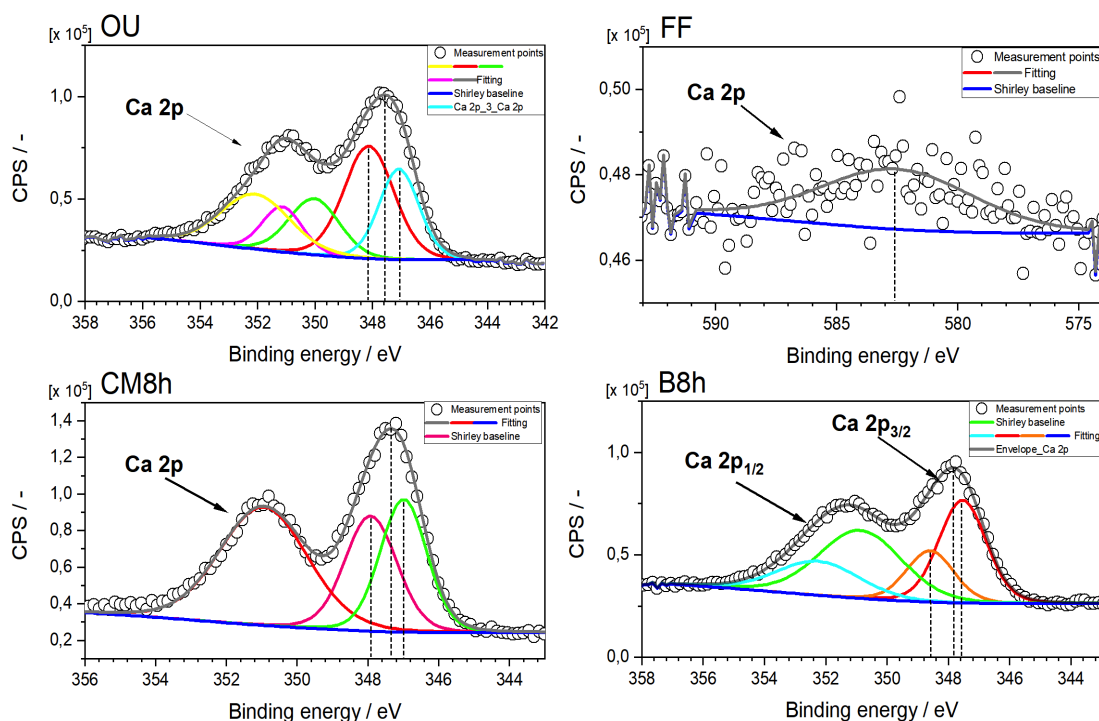


Figure 4.11: XPS fitting for $Ca\ 2p$ peaks of selected samples

The $Ca\ 2p_{3/2}$ binding energy peak of Olivine used was measured at 347.5 eV and two peaks were fitted beneath, at 347.0 eV and at 348.2 eV. The fitting corresponding to an energy of 347.0 eV suggests the occurrence of Ca as CaO and at 348.2 eV to possibly another (unknown) Ca species. Similarly, the measured $Ca\ 2p_{3/2}$ peak of CM8h can be fitted by two peaks, one at 347.0 eV to be assigned to again CaO and another peak at 347.8 eV that roughly corresponds to $CaHPO_4$. Moreover, Figure 4.11 displays a fitted peak for B8h at 347.4 eV suggesting CaO and the second fitted peak at 348.6 eV another compound of calcium. The Ca peak of feldspar fresh points out the occurrence of a different calcium species with a peak at 582.5 eV.

Analogous to Ca , other detected elements can be assigned to corresponding compounds as well. Table 4.3 lists the possible and plausible assignments for selected elements. The XPS spectra, including available high resolution spectra, are to be consulted in the appendix (Figure 7.9 - 7.16).

CaO could be assigned to Olivine used, CM8h, B8h and B32h whereas $CaHPO_4$ to CM8h, Mix8h and Mix40h. However, phosphorus was detected in FF, CM8h, B8h, B32h, Mix8h and Mix40h ranging between 3-4 %, cf. Figure 4.10. A look at the binding energy shift for P corroborates the occurrence of phosphorus as phosphate for CM8h, Mix8h and Mix40h other high resolution spectra of phosphorus were unfortunately not made. Further were the binding energies of oxygen examined. The silicate species of oxygen is plausible for all samples since all bed material grains are essentially silicates. Oxygen as phosphate is possible for FF, CM8h, B8h, B32h, Mix8h and Mix40h and was also fitted accordingly. Literature binding energies for oxygen as MgO or CaO could not be found. Carbonates are the most similar compounds found to these oxides and are possible according to $O\ 1s$ peaks for OU, CM8h, B8h, Mix8h and Mix40h.

Table 4.3: Plausible assignments of fitted peaks for Ca , O and P

	Ca species	O species	P species
OF	no high resolution spectra	SiO_2	-
OU	CaO	$SiO_2, (CO_3)^{-2}$	-
FF	-	$SiO_2, (PO_4)^{-3}$	no high resolution spectra
CM8h	$CaO, CaHPO_4$	$SiO_2, (CO_3)^{-2}, (PO_4)^{-3}$	$(PO_4)^{-3}$
B8h	CaO	$SiO_2, (CO_3)^{-2}, (PO_4)^{-3}$	no high resolution spectra
B32h	CaO	$SiO_2, (PO_4)^{-3}$	no high resolution spectra
Mix8h	$CaHPO_4$	$SiO_2, (CO_3)^{-2}, (PO_4)^{-3}$	$(PO_4)^{-3}$
Mix40h	$CaHPO_4$	$SiO_2, (CO_3)^{-2}, (PO_4)^{-3}$	$(PO_4)^{-3}, CaHPO_4$

The EDX signals differ not only in penetration depth compared to XPS but also in sensitivity towards light elements ($Z < 10$). Still, the same elements were detected by EDX as in XPS, however, in (very) different percentages. Light elements, such as carbon and oxygen, emit low energetic x-radiation (below 1 keV), that is, in addition not very intensive. Figure 7.17, in the appendix, displays the registered x-ray spectra following EDX measurements. As illustrated in Figure 4.12 EDX therefore underestimates the oxygen content of the samples and the silicate structure of Olivine fresh and Feldspar fresh is not recognized. Moreover, the magnesium/iron ratio in OF is significantly higher (11.5) compared to XPS (0.6). Consequently, the sensitivity towards iron is in EDX is also very low. However, the aluminium/silicon ratio in FF derived by EDX (0.3) is more related to the one by XPS (0.4).

Calcium was measured in all samples except Olivine and Feldspar fresh ranging between 18% in OU and B8h and 59% in CM8h. Significant amounts of phosphorus > 10% were found in CM8h, Mix8h and Mix40h as well as > 14% of aluminium in OU, FF, B8h and B32h and > 9% of potassium in all samples but OF and CM8h.

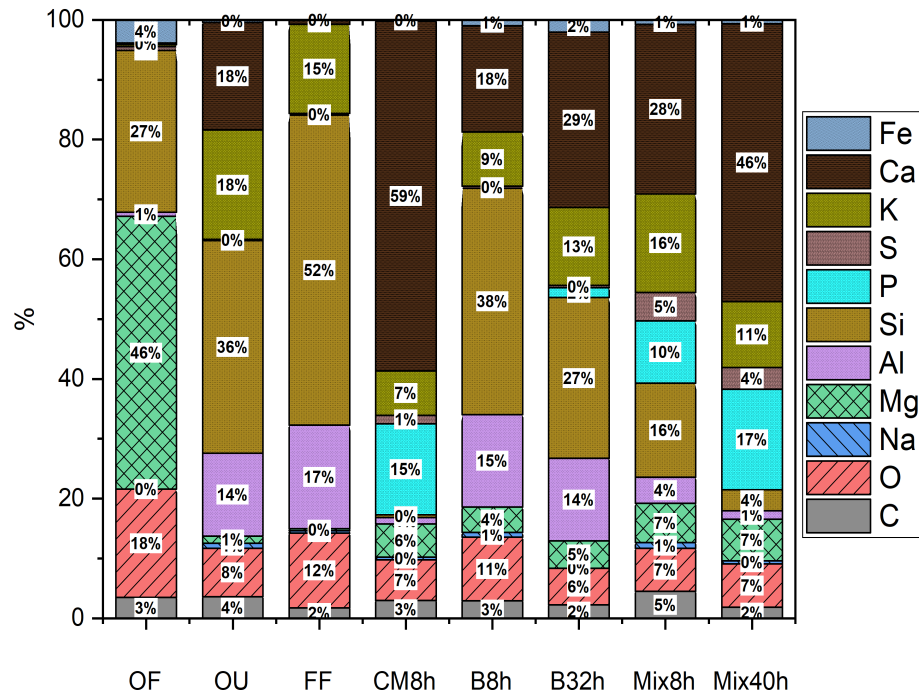


Figure 4.12: Elemental information derived by EDX measurements

4.2.2 Bulk properties: XRD and XRF

High energy x-radiation passes through the bed material grains and only elements $Z > 11$ -13 emit effectively secondary x-rays. Consequently, the heavy elements iron and potassium are overestimated in samples OF and FF, respectively. Despite the lack of surface sensitivity Figure 4.13 illustrates high contents of calcium throughout all used bed material grains. The samples that were 8 hours in the reactor showed calcium concentrations of 32 % for B8h and 41 % for Mix8h and 55 % for CM8h. Similar to CM8h, the measurements indicate high calcium concentrations of 46 % in B32h, 57 % in Mix40h and 68 % in OU. Moreover, iron concentrations were found not only in the Olivine samples but also in Feldspar samples. Particularly striking are iron concentrations of 21 % in B32h compared to 25 % in Olivine used. That suggests a high iron content in bark ash and calls the real penetration depth of XRF into question.

Phosphorus was detected in significant quantities > 3 % in CM8h, Mix8h and Mix40h. The silicon content is highest in Feldspar fresh and was measured in lower quantities only in B8h, B32h and Mix8h. Sulfur was registered in CM8h, B32h, Mix8h and Mix40h. Heavy metals such as chromium was found with 4 % in Olivine fresh and 1 % in Olivine used, manganese was found in all samples and up to 6 % in B32h. Traces < 4 % of nickel were found in all samples however, zinc was only detected in CM8h, B8h, B32h, Mix8h and Mix40h.

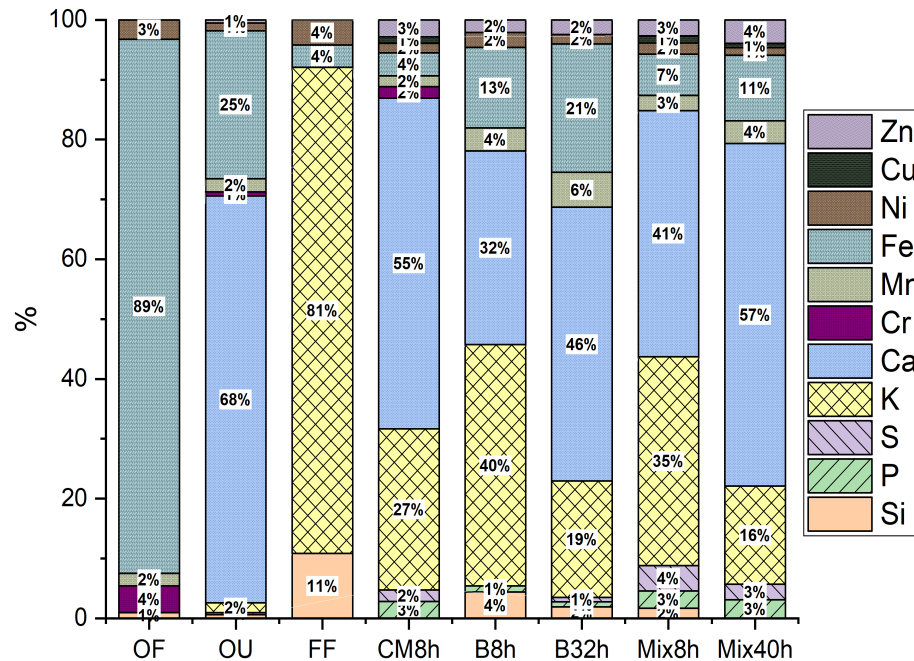


Figure 4.13: Elemental information derived by XRF measurements

In XRD the employed high energy x-radiation passes through the bed material grains and yields information about the lattice structures of the samples, contrasting elemental information disclosed by XRF. Figure 7.18 shows the line-up of the diffraction spectra for Olivine fresh and Olivine used. Peaks that were detected only in Olivine used were assigned to corresponding compounds based on elemental information derived by XPS and XRF. Each compound produces a plurality of peaks in the spectra wherefore a definite allocation of peaks is difficult for heterogeneous specimen. The employed criteria for the assignment was the match of at least 2 well defined peaks.

Figures 7.19 and 7.20 reveal the XRD spectra of the feldspar samples which are overall more complex compared to Olivine used, in particular spectra of CM8h, Mix8h and Mix40h and are to be consulted in the appendix.

The summary of this phase analysis is presented in Figure 4.14 and is not quantitative. Carbon species and quartz were found in all used samples whereas CaO peaks could only be allocated to Olivine used and CM8h. Other calcium species were found in all used bed materials, however. Phosphate compounds were found in CM8h, Mix8h and Mix40h. $Ca_{10}(PO_4)_6O$ was assigned to peaks in spectra of CM8h and Mix40h and $KNaCa_2(PO_4)_2$ in CM8h and Mix8h. Potassium compounds matched with peaks in spectra of B32h, Mix8h and Mix40h.

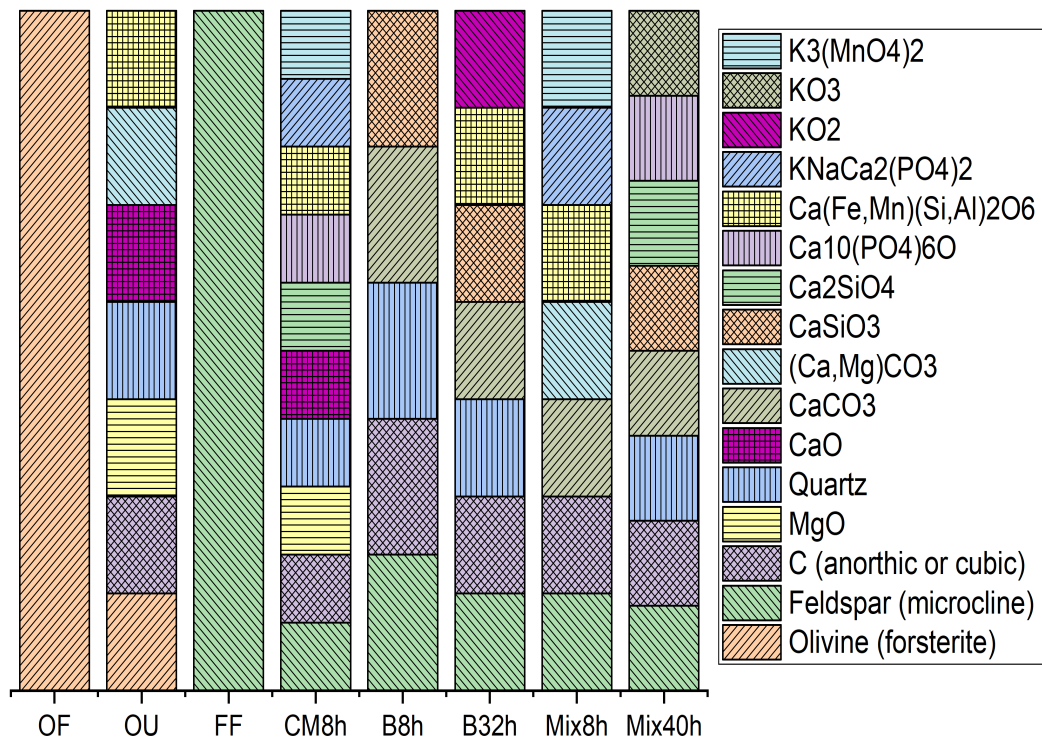


Figure 4.14: Compilation of the XRD phase analysis

4.2.3 Chemical structure: Raman spectroscopy

Figure 4.15 displays the measured Raman spectra of both Olivine fresh and Olivine used. The Raman spectra of Olivine crystals exhibit a characteristic set of two lines between 900 - 800 cm^{-1} . The asymmetric stretching band of Si-O appears at circa 850 cm^{-1} and the symmetric stretching band around 825 cm^{-1} [75]. The exact position depends on the metal ions present in the crystal lattice. Forsterite (Mg_2SiO_4) produces a peak at 856 and 824 cm^{-1} whereas Fayalite (Fe_2SiO_4) at 840 and 814 cm^{-1} [39]. The measured peaks in Olivine fresh and Olivine used appear at 854.5 and 823.1 cm^{-1} and thus resemble more Forsterite than Fayalite. This shift in peak position, depending on the metal ions present in the lattice, applies also for the other peaks wherefore all given wavenumbers of Olivine samples are rounded. The peaks in both OF and OU at 325 cm^{-1} (SiO_4 rotation), 300 cm^{-1} ($M2$ translation) and 225 cm^{-1} (SiO_4 translation) correspond to vibrations in the mineral lattice and are therefore not considered for the evaluation of the ash layer [75].

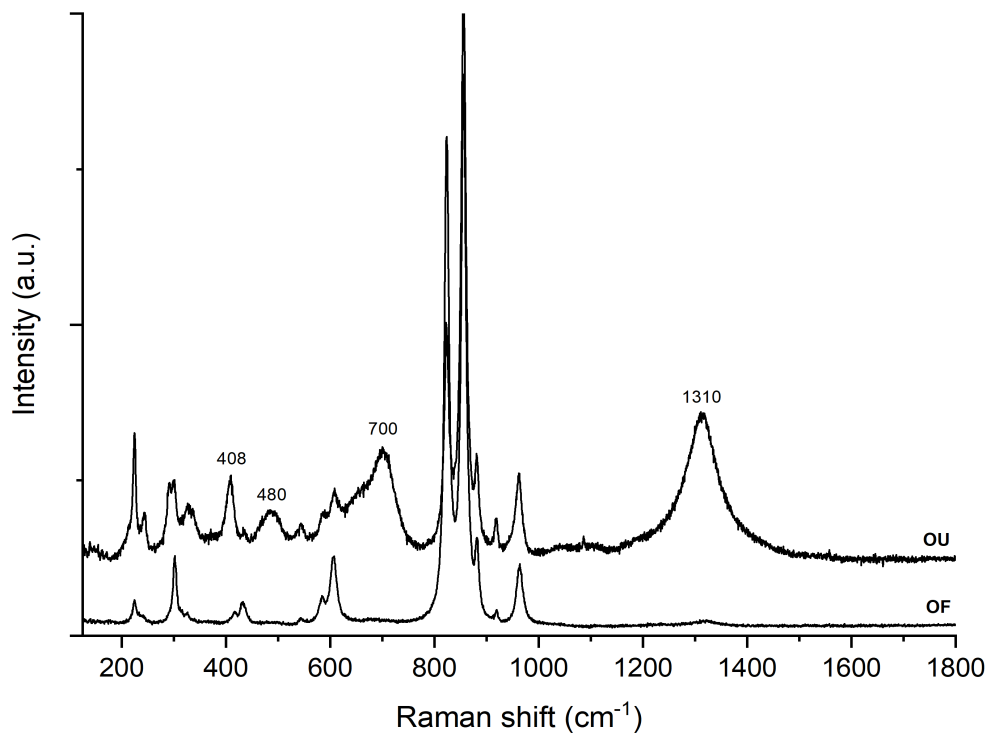


Figure 4.15: Raman spectra of Olivine samples

Figure 4.16 displays the measured Raman spectra of the Feldspar samples. Similarly to Olivine, Feldspar exhibits three characteristic lines. The peak where found at 513.7 cm^{-1} , 475.8 cm^{-1} and 453.5 cm^{-1} match perfectly with literature values of Microcline or Orthoclase ($KAlSi_3O_8$) [76].

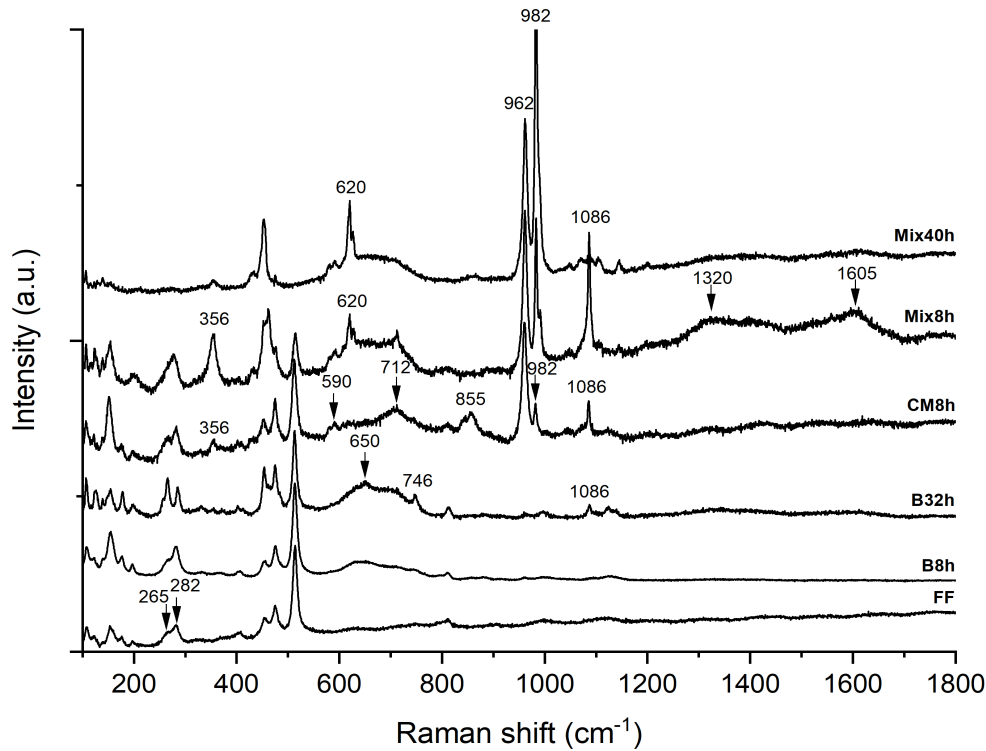


Figure 4.16: Raman spectra of Feldspar samples

By comparison of Olivine used with Olivine fresh and the used Feldspar grains with Feldspar fresh the peaks standing out and can be attributed to the ash layer and are listed in Table 4.4. Spectra of pure CaO , $CaCO_3$, MgO and Fe_2O_3 were collected as well and allow for the allocation of peaks, cf. appendix Figure 7.21. Where not applicable, literature data was sought.

Table 4.4: Raman signals evoked by the ash layer and allocation to reference compounds

Raman shift	Sample	Reference compound
~ 1600 and 1320 cm^{-1}	(Mix8h)	<i>Carbonaceous deposit</i> [77]
1310 cm^{-1}	(OU, Mix8h)	Fe_2O_3
1086 cm^{-1}	(B32h, CM8h, Mix8h)	$CaCO_3$ (CaO)
982 and 962 cm^{-1}	(CM8h, Mix8h, Mix40h)	$(PO_4)^{-3}$ [78]
982 cm^{-1}	(CM8h, Mix8h, Mix40h)	K_2SO_4 [79]
855 cm^{-1}	(CM8h)	<i>unknown</i>
712 cm^{-1}	(CM8h, Mix8h)	$CaCO_3$
$\sim 650\text{ cm}^{-1}$	(OU, B8h, B32h, CM8h, Mix8h, Mix40h)	CaO
620 cm^{-1}	(CM8h, Mix8h, Mix40h)	K_2SO_4 [79]
590 cm^{-1}	(CM8h, Mix8h, Mix40h)	$(PO_4)^{-3}$ [78]
480 cm^{-1}	(OU)	SiO_2 [80]
410 cm^{-1}	(OU)	Fe_2O_3
356 cm^{-1}	(B32h, CM8h, Mix8h, Mix40h)	CaO

As ash layers are formed some peaks originating from the mineral structure of K-Feldspar such as 265 and 282 cm^{-1} alter their shape or disappear completely, as in Mix40h. Moreover, the Raman measurements suggest the occurrence of CaO in all used bed material grains for a broad peak $\sim 650\text{ cm}^{-1}$ was detected in all used samples. A second CaO signal at 356 cm^{-1} , however, was only found for B32h, CM8h, Mix8h, Mix40h. Since CaO and $CaCO_3$ share an intensive peak at circa 1080 cm^{-1} (CaO at 1080 cm^{-1} and $CaCO_3$ at 1086 cm^{-1}) a distinction has to be made by a second peak. $CaCO_3$ produces another signal at 712 cm^{-1} and was measured for CM8h and Mix8h. In Mix40h the peak at 712 cm^{-1} is not detected.

Penel et. al. [78] detected an intensive peak at 964 cm^{-1} corresponding to the vibration of $(PO_4)^{-3}$ in hydroxyapatite ($Ca_5(PO_4)_3(OH)$). Yet, after measuring carbonated apatite, that is when carbonates replace some phosphate groups in the lattice, they detected a splitting of the single peak in two parts 957 and 947 cm^{-1} . Litasov et. al. [81], on the other hand, measured various phosphate minerals and the found signals in CM8h, Mix8h and Mix40h at 983 and 962 cm^{-1} could be explained by a blend of Merrilite $Ca_9NaMg(PO_4)_7$ that shows signals at 974 and 958 cm^{-1} and Brianite $Na_2CaMg(PO_4)_2$ presenting peaks at 986 and 968 cm^{-1} .

Interestingly, in CM8h the peak at 962 cm^{-1} is more intensive than 982 cm^{-1} whereas in Mix8h they are equally intensive and in Mix40h 982 cm^{-1} is much higher than 962 cm^{-1} . The signal detected in CM8h, Mix8h and Mix40h at 590 cm^{-1} supports, however, the presence of phosphate as it corresponds to the ν_4 vibration of PO_4 . Nevertheless, the signal at 982 cm^{-1} fits also very well to K_2SO_4 that is suggested also by a second peak appearing at 620 cm^{-1} in CM8h, Mix8h, Mix40h [79].

Hematite (Fe_2O_3) could be assigned to peaks found in Olivine used and Mix8h. The broad peak at 1320 cm^{-1} in Mix8h belongs probably together with another broad peak at 1605 cm^{-1} to carbonaceous deposit. The peak at 1605 cm^{-1} corresponds to crystallite graphite and the second at 1320 cm^{-1} to a disordered carbon phase, formed during combustion and is called pyrolytic carbon [77].

4.2.4 Chemical structure: FT-IR spectroscopy

The samples were assessed by three sampling modes of IR spectroscopy: ATR, DRIFT and Transmission mode. The collected spectra obtained by each sampling mode of Olivine used is arranged in Figure 4.17. A sharp high frequency band and a broad band around 1500 cm^{-1} characterize Olivine used. Although all three techniques yield the same major signals differences in the scanned frequency range and varying intensities of some peaks become apparent. ATR gives spectra ranging from $4000 - 500\text{ cm}^{-1}$ whereas the used Transmission IR recorded a spectral range from $4000 - 1000\text{ cm}^{-1}$. Mid-frequency peaks at circa 3000 , 2500 and 2000 cm^{-1} are missing in the ATR spectrum but are detected in both DRIFTS and Transmission IR.

Moreover, only DRIFTS and Transmission techniques allow for a study of adsorbed molecules on the bed material surface.

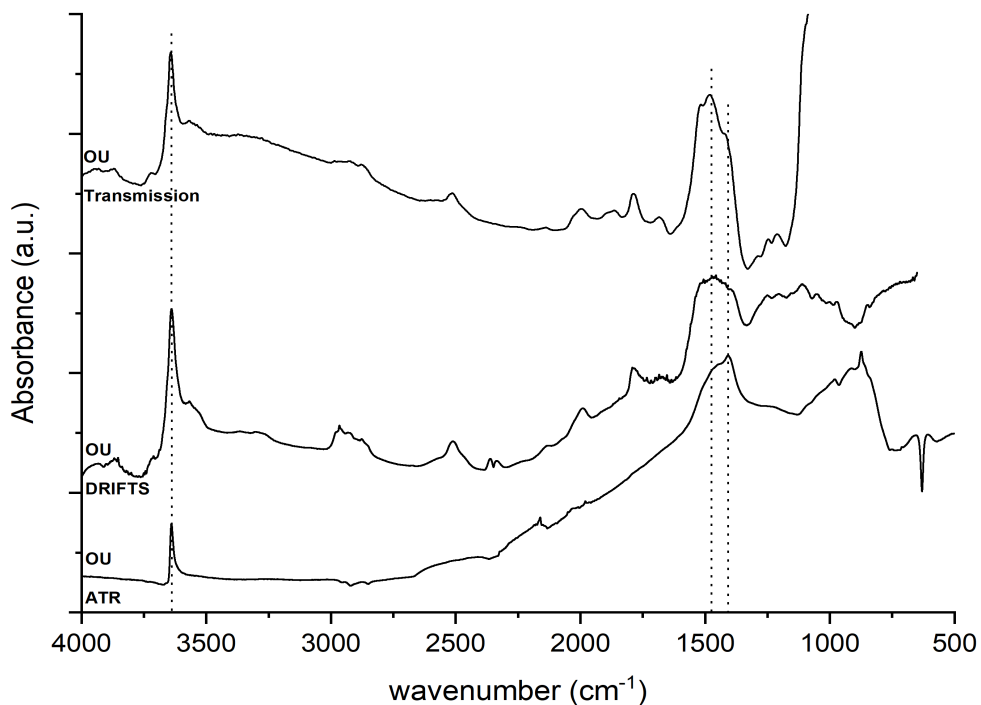


Figure 4.17: Olivine used spectra obtained from ATR, DRIFTS, Transmission IR

Spectra of reference compounds (CaO , MgO and SiO_2) were also collected and are shown together with Olivine and Feldspar samples in Figure 4.18 and 4.20. In addition, literature [82], [83], [84] helped the allocation of a majority of peaks.

The high frequency peak which appears at $3650\text{--}3640\text{ cm}^{-1}$ in OU, B8h, CM8h and Mix40h corresponds to $O\text{-H}$ of $\text{Ca}(\text{OH})_2$, formed by atmospheric humidity. The broad band around 1480 cm^{-1} , clearly visible in OU and even more pronounced in ground OU, corresponds together with 875 cm^{-1} to $C\text{-O}$ elongation modes of carbonate.

However, the broad 1480 cm^{-1} band appears also for pure CaO (neglecting minor amounts of $\text{Ca}(\text{OH})_2$ on the surface). Unique to CaCO_3 are, however, peaks at 2925 cm^{-1} corresponding to harmonic vibration of $C\text{-O}$ elongation, found in OU, and seem to disappear during grinding OU. The $C\text{-O}$ vibration at 2515 cm^{-1} is part of a CaCO_3 and $\text{Ca}(\text{OH})_2$ spectra.

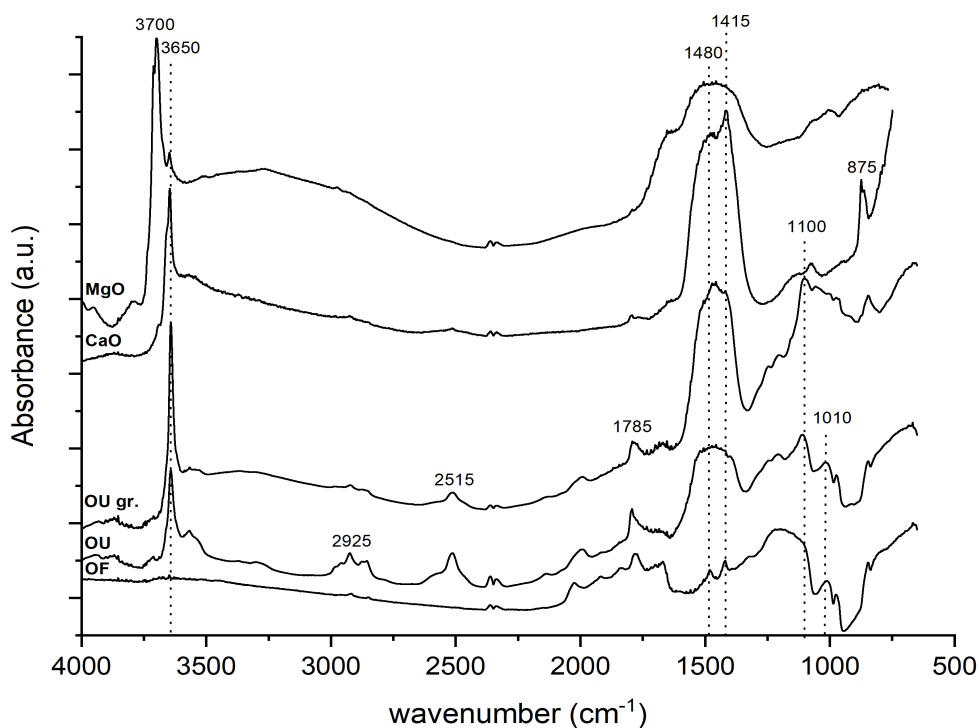


Figure 4.18: Olivine fresh, Olivine used and Olivine used finely ground are compared to CaO and MgO (DRIFTS)

The $O\text{-H}$ peak disappears when heating the sample up to 500°C as depicted in Figure 4.19 indicating the desorption of water from the surface. The peak is only restored by hydrating the sample, a reducing treatment with hydrogen is not sufficient (at least at 350°C). Overall, reducing conditions do not alter the Olivine used spectrum compared to oxidizing conditions. High temperature oxidizing conditions enhance $C\text{-O}$ related peaks around 1500 and 1750 cm^{-1} .

Figure 4.20 illustrates the Feldspar samples compared to SiO_2 . Analogous to OU present the used Feldspar samples (only B8h, CM8h and Mix40h are depicted) a high frequency peak at 3643 cm^{-1} corresponding to $O\text{-H}$ of $\text{Ca}(\text{OH})_2$. CM8h and Mix40h further indicate a second high frequency peak at 3568 cm^{-1} that can be allocated to hydroxy groups formed by reaction phosphates with atmospheric humidity. Apart from that, the Feldspar spectra resemble to a large extent the silicate spectrum.

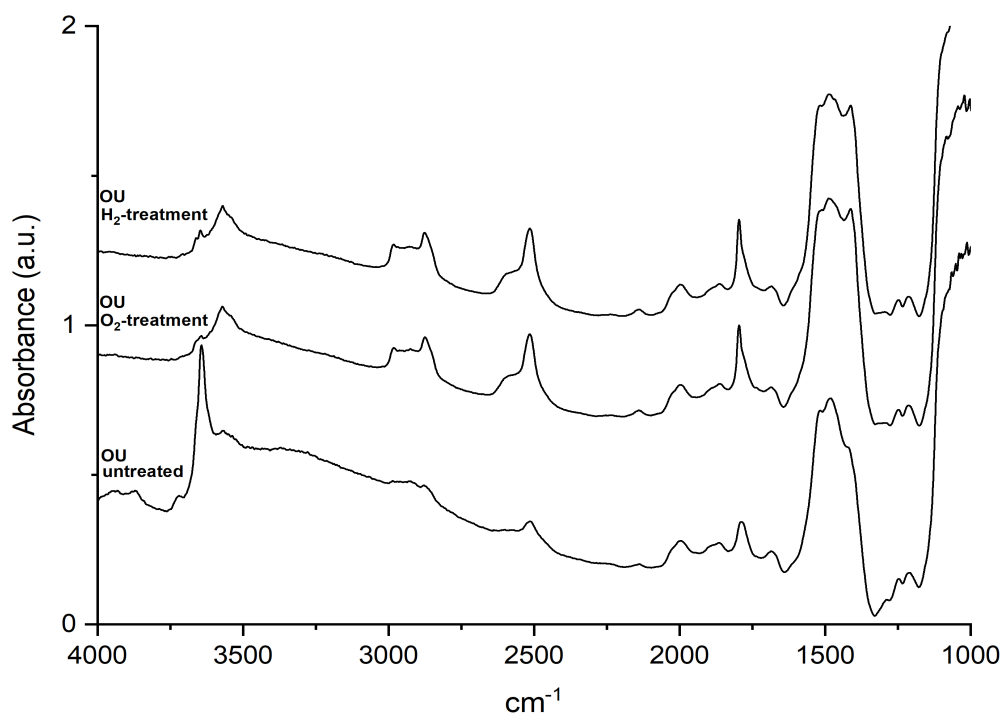


Figure 4.19: Changes in OU spectra after heating the sample up to 500°C in O₂ atmosphere and afterwards heating up to 350°C in H₂ atmosphere (Transmission IR)

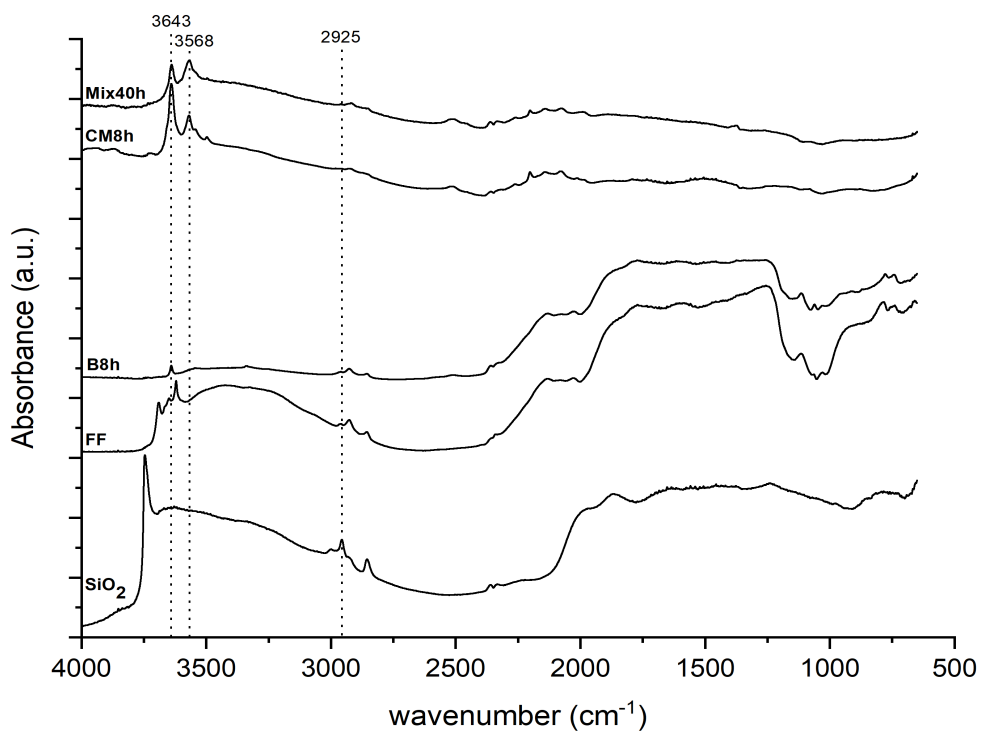


Figure 4.20: Feldspar samples compared to SiO₂ (DRIFTS)

4.3 Adsorption of probe molecules

4.3.1 Methanol adsorption

Since IR spectroscopy is very sensitive to polar functional groups in molecules it is mostly employed for the detection of adsorbed species on a solid rather than its structural analysis. Adsorbing different probe molecules onto a solid allows for the study of active sites present on the surface. Methanol is a polar molecule that is able to dissociate its proton and donate it to Brønsted basic sites. In addition, due to the electron pairs on the oxygen atom it is a Lewis base and thus able to bind also onto Lewis acid sites.

The spectra in Figure 4.21 are complicated and indicate simultaneous presence of adsorbed species on *CaO*. The broad peak between $3300 - 3200\text{ cm}^{-1}$ is assigned to the stretching mode of hydrogen bonded hydroxyl groups. The peak disappears at higher temperatures indicating that such species is easily desorbed. The band located at circa 1650 cm^{-1} is physisorbed water and desorbs also between $100\text{-}200\text{ }^\circ\text{C}$. [20]

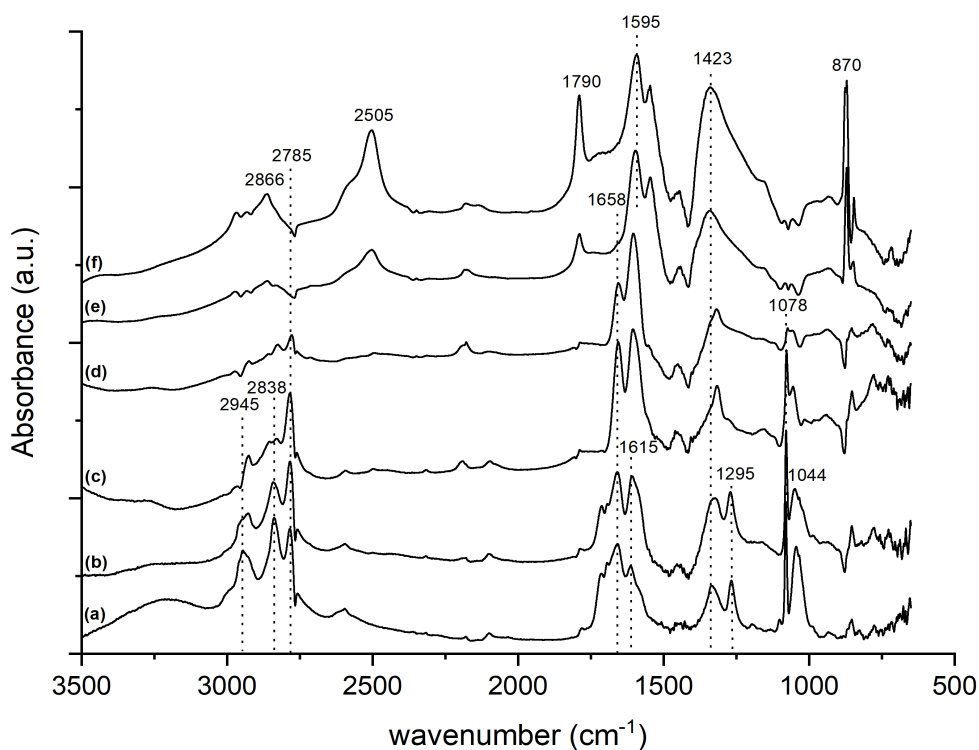


Figure 4.21: MeOH adsorption on *CaO* (DRIFTS): (a) Subtraction result *CaO* after MeOH adsorption $40\text{ }^\circ\text{C}$, (b) $100\text{ }^\circ\text{C}$, (c) $200\text{ }^\circ\text{C}$, (d) $300\text{ }^\circ\text{C}$, (e) $400\text{ }^\circ\text{C}$, (f) $500\text{ }^\circ\text{C}$

The chemisorption of methanol is indicated by three peaks 3000-2800 cm^{-1} , two sharp shoulders at 1423 and 1295 cm^{-1} and a sharp band at 1078 cm^{-1} that disappear above 300 °C. The *C-O* stretching mode belongs to 1078 cm^{-1} of chemisorbed methoxy (CH_3O). The methoxy group is further characterized by three peaks in the regime 3000-2800 cm^{-1} corresponding to symmetric *C-H* stretching mode that disappears together with band 1078 above 400 °C. The splitting is due to Fermi resonance with a symmetric deformation [85]. 1423 and 1295 cm^{-1} correspond to *C-H* bending modes. [86], [20]

The band at 1615 cm^{-1} that shifts to 1595 cm^{-1} at higher temperatures can be attributed to *C-O* vibrations. Adsorption bands in the region of 1300-1400 cm^{-1} are due to the symmetric *OCO* stretching mode and bands between 1500 and 1700 cm^{-1} are because of the asymmetric mode of this group. However, the assignment is not unambiguous as Carbonate and Formate species show bands in this region, cf. Figure 7.22. With increasing temperature the peaks related to Formate in the region of 1700-1500 cm^{-1} shifts to lower wavenumbers that might be explained as bidentate Formate is more stable than monodentate Formate. [20], [86]

As the signal of chemisorbed methoxy decreases a new peak at 870 cm^{-1} in the region of *C-H* of olefines. At 500 °C a broad band at 2866 cm^{-1} emerges corresponding to *C-H* of aliphatic CH_3 or acyclic $C=OCH_2$.

Similarly to *HAc* adsorption a peak at 2505 cm^{-1} appears at 400 °C and may be assigned to ketene ($C=C=O$) [87], [88]. The emergence of 1790 cm^{-1} further suggests a vibration of *C=O* in condensated or cyclic carbonate groups [87].

4.3.2 Acetic acid adsorption

The adsorption of acetic acid vapor (CH_3COOH or HAc) discloses the presence of Brønsted basic sites, that is, the oxygen ions (O^{-2}) on the surface of oxide systems [19].

The peak at 3645 cm^{-1} is attributed to $O-H$ of protonated CaO and shifts at higher temperatures towards 3633 cm^{-1} at $400\text{ }^\circ C$ before it disappears at $500\text{ }^\circ C$. The band at 2930 cm^{-1} can be assigned together with 1025 and 1328 cm^{-1} to $C-H$ modes in CH_3 that stay unshifted at high temperatures. 1707 cm^{-1} can be assigned to $C=O$ and 1305 cm^{-1} to $C-OH$ of residual acid and consequently is driven off the surface above $100\text{ }^\circ C$. [89]

Further remarkable is the peak at 2490 cm^{-1} that appears at $500\text{ }^\circ C$ and can be assigned to ketene ($C=C=O$) [87], [88].

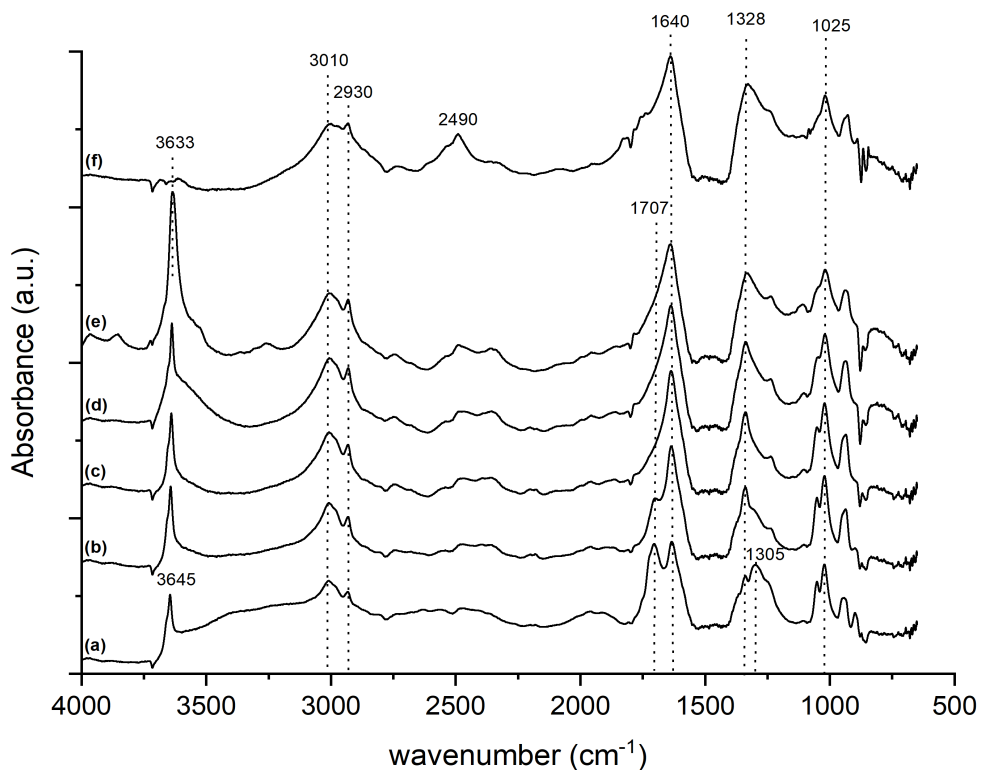


Figure 4.22: HAc adsorption on CaO (DRIFTS): (a) Subtraction result CaO after HAc adsorption $40\text{ }^\circ C$, (b) $100\text{ }^\circ C$, (c) $200\text{ }^\circ C$, (d) $300\text{ }^\circ C$, (e) $400\text{ }^\circ C$, (f) $500\text{ }^\circ C$

4.3.3 Carbon monoxide adsorption

Carbon monoxide has a special ability as a probe molecule for its small size and produces relatively simple IR spectra. CO probe molecules can be used to investigate both basic and acidic Lewis sites on both oxides and transition metals. With transition metals CO forms synergistic π -bonds characterized by a σ and two π bonds. The chemisorption of CO on metal oxides involves surface oxygen ions, hydroxyl groups and unsaturated cations. During interactions with surface oxygen ions carbonate groups are often formed and together with surface hydroxyl groups it produces surface formate species. [8]

Figure 4.23 presents the adsorption of carbon monoxide on CaO . Two prominent peaks at 2170 and 2120 cm^{-1} during the adsorption belong to gas phase CO . Adsorbed species of CO on a transition metal would produce a signal just below 2100 cm^{-1} . However, a peak at 1565 cm^{-1} is observed already during adsorption at low temperatures. 1565 cm^{-1} ranges in the regime of $C-O$ stretching modes of CO_2^{-2} . Again the distinction between formate and carbonate signals is not unambiguous. However, 1565 cm^{-1} could be allocated to carbonate that decreases with elevated temperatures and the small peak at 1328 cm^{-1} to formate.

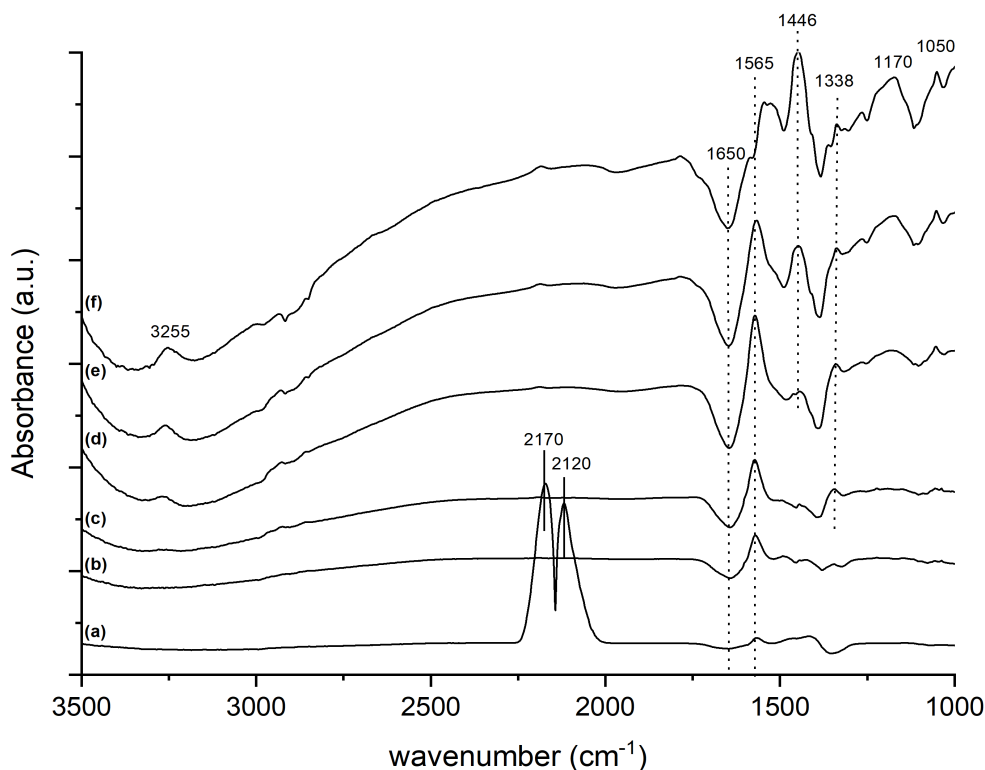


Figure 4.23: CO adsorption on CaO (Transmission mode): (a) Subtraction result CaO during CO adsorption 500 $mbar$ ambient temperature, (b) after CO adsorption vacuum a.t., (c) 100°C, (d) 200°C, (e) 300°C, (f) 400°C

At elevated temperatures a second peak at 1446 cm^{-1} appears, possibly $C-O$ modes of carbonate, cf. 1480 cm^{-1} in Figure 4.18. Nevertheless, the surging peak could also be due to structural changes in the oxide.

Garrone et. al. propose two possible electronic structures for adsorbed CO $C-O$ and $C=O$ species chemisorbed on CaO . They measured a peak at 1484 cm^{-1} , compared to the detected peak at 1446 cm^{-1} , and was allocated to $C=O$ in (II) Figure 4.24 [18].

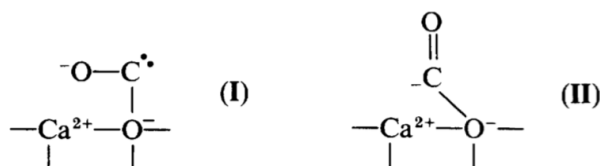


Figure 4.24: Monomeric CO chemisorbed on CaO as proposed by Garrone et. al. [18]

The adsorption of CO on Olivine used is not very pronounced, recognizable in Figure 4.25 by high noise levels. Nevertheless, a peak at 1365 cm^{-1} remained after evacuating the IR chamber and could be attributed to formate, cf. CO adsorption on CaO .

A second peak emerging at 1595 cm^{-1} corresponds also to $C-O$ of formate groups by reaction with CaO . In addition, a sharp peak at 2044 cm^{-1} was detected that corresponds to chemisorbed CO on iron [90]. A broad peak around 1923 was also measured but could not be assigned.

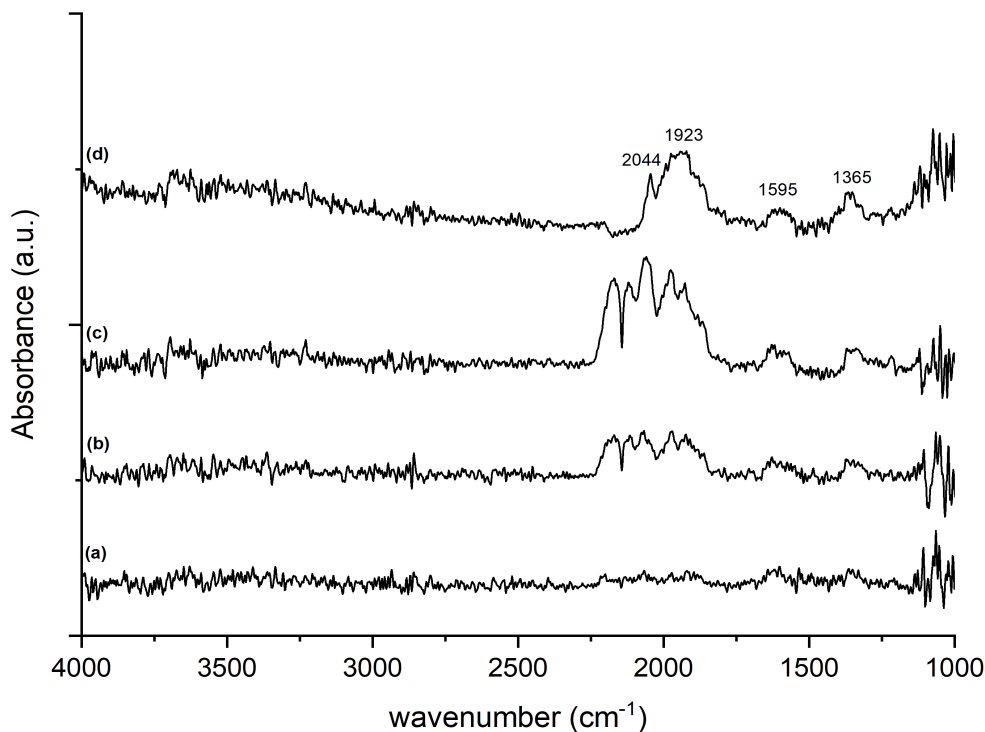


Figure 4.25: CO adsorption on Olivine used (Transmission mode): (a) Subtraction result OU during CO adsorption 10 mbar ambient temperature, (b) Subtraction result OU during CO adsorption 50 mbar a.t., (c) Subtraction result OU during CO adsorption 100 mbar a.t., (d) after adsorption and vacuum

Discussion of results

Both SEM images and BET surface area measurements show an increase in surface irregularities at a microscopic level. A comparison of close-up views of Olivine fresh (OF) and Olivine used (OU) in Figures 4.2, 4.3 discloses a much more irregular surface texture of Olivine used. This claim is substantiated by BET surface areas: Olivine used exhibits a surface area of $4.6 \text{ m}^2/\text{g}$ whereas Olivine fresh only $0.4 \text{ m}^2/\text{g}$. Moreover, the BJH pore size distribution analysis suggests the formation of small pores over the process of the ash layer formation. The average pore width for Olivine fresh is estimated as 14.5 nm and for Olivine used 7.2 nm , cf. Table 4.2. The measured surface areas, however, are very low compared to industrial catalysts with surface areas typically above $100 \text{ m}^2/\text{g}$ [8].

The same increase in BET surface area is observed for Feldspar grains taken out of a reactor fueled with bark (B8h and B32h), chicken manure (CM8h) and the mix of chicken manure and bark (Mix8h and Mix40h). However, a reduction in pore width compared to Feldspar fresh is only indicated for CM8h, Mix8h and Mix40h. Besides a greater surface area and a smaller average pore size, SEM images reveal fine structures (visible at low magnification) of ash layered CM8h and Mix8h. In particular CM8h and Mix8h show fine ash deposits adhered to the grains. Yet, they seem to diminish with residence time in the reactor as Mix40h shows much less fine surface structures.

The substantially higher BET surface area of CM8h ($1.4 \text{ m}^2/\text{g}$) compared to B8h ($0.4 \text{ m}^2/\text{g}$) is presumed to be a result of the high ash content of chicken manure (25 %) compared to bark (4-8 %). Significantly more ash stayed in the fluidized bed reactor leading to faster ash layer formation and thus more and smaller pores. However, it cannot be ruled out that loosely adhered ash on CM8h and Mix8h and its debris next to the grains affects the assessment of surface area. Due to a lower ash content of bark B8h and B32h show a less irregular surface texture at low magnification compared to CM8h, Mix8h and Mix40h. Also the average pore size of B8h and B32h is estimated higher compared to Feldspar fresh. Nevertheless, BET surface area increases from B8h to B32h and high magnification SEM images disclose fine irregularities similar to other used bed material grains.

The assessment of the elemental composition of the bed material was carried out by XPS, EDX and XRF. Since not all techniques are sensitive to the same range of elements selected element concentrations, theoretically detectable in all techniques, were extrapolated and are displayed in Figure 5.1. Consequently, each method presents information of different depths of the bed material grains but convey also information about their sensitivity towards certain elements. High energy x-radiation of XRF passes through the grains, low energy x-rays in XPS are sensitive to the outermost layer of 1 nm and the electron beam employed by EDX penetrates up to a quarter of the grain's length.

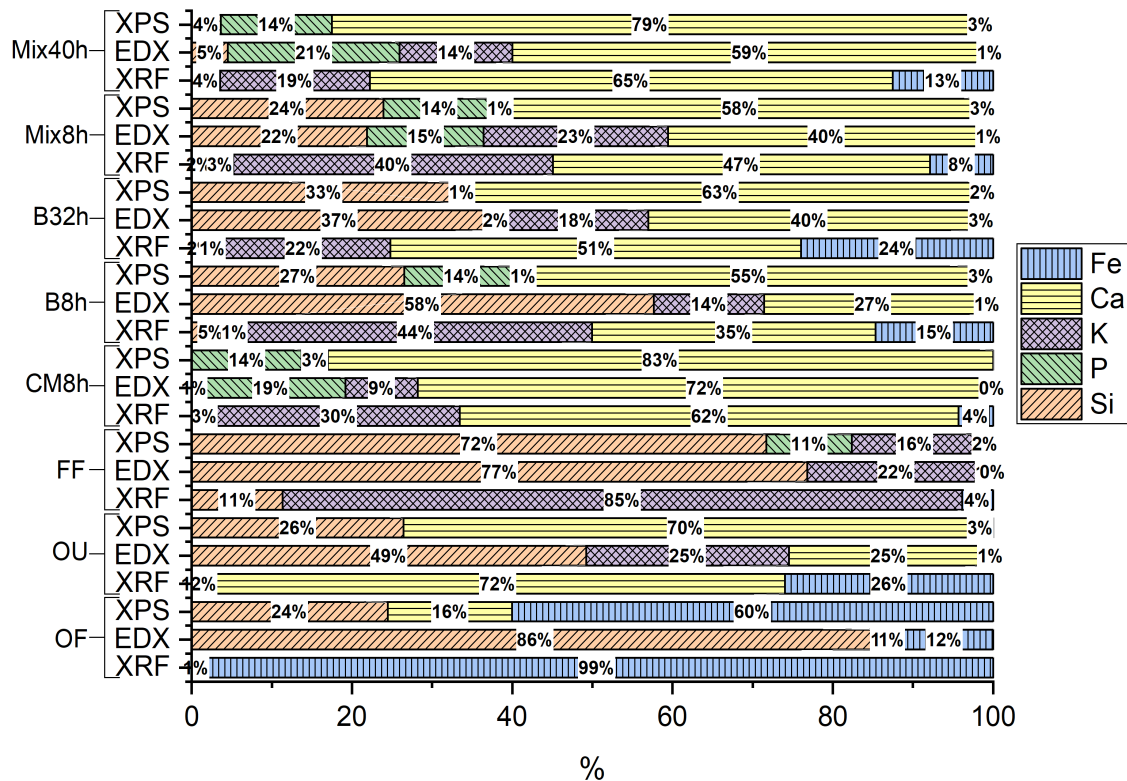


Figure 5.1: Extrapolation of elemental composition derived by XRF, EDX and XPS results for selected elements (*Si*, *P*, *K*, *Ca*, *Fe*)

The *Ca* concentration of Olivine used detected by XPS amounts to 70 % compared to only 25 % estimated by EDX. The increased penetration depth of EDX is substantiated further by samples OU, B8h, B32h and Mix8h where EDX not only registers less calcium but also more silicon compared to XPS. Nonetheless, no difference in *Si* concentration between EDX and XPS was detected in Mix40h and CM8h suggesting that the EDX signal did not penetrate the ash layer.

XRF, on the other hand, reveals a low sensitivity towards silicon shown in Olivine used and Feldspar fresh that results in an iron and potassium concentration out of proportion. It is, however, very sensitive towards calcium. The result of 16 % *Ca* in Olivine fresh by XPS is clearly contradicted by the XRF measurement where < 1 % *Ca* was found. Furthermore striking are iron contents found by XRF in B8h, B32h, Mix8h and Mix40h. Iron amounts to only 5 w% of bark ash but totals > 20 % in B32h. Significant amounts of phosphorus were found by at least two techniques in CM8h, Mix8h and Mix40h due to >25 w% of *P* in the ash of chicken manure.

Having said that, all three techniques were used without the use of internal standards and deduced quantities have to be taken with a grain of salt. Nevertheless, conclusions about the grain's composition can be drawn.

The most interesting elemental information is, however, presented by XPS, cf. Figure 4.10. Besides the highest accuracy of results, the assessment of elemental concentrations in the very surface affects directly the catalytic activity of the bed material. The derived chemical formula (neglecting contaminations of *C*, *Al*, *K* and *Ca*) is calculated as $(Fe_{1.51}, Mg_{0.93})_2Si_{1.16}O_{3.95}$ compared to the Olivine mineral formula $((Fe, Mg)SiO_4)$ in literature [39]. Feldspar fresh on the other hand contains 4 % of potassium, yielding a chemical formula of pure potassium feldspar $K_{0.51}Al_{1.03}Si_{2.31}O_{6.15}$ and when including sodium $(Na_{0.37}K_{0.49})Al_{0.98}Si_{2.22}O_{5.93}$ compared to K-feldspar $(KAlSi_3O_8)$ characterized in literature [76].

Iron concentrations detected by XPS are interesting as the transition metal is catalytically active. With exception of CM8h, all used bed material samples showed *Fe* concentrations in the surface of ~ 1 %. Other known catalytically active compounds are *CaO* and *MgO*. The oxides of calcium and magnesium were already employed in the gasification of heavy oils as a catalytically active supplement. Calcium quantities in the surface layer range between 21 % in CM8h and 14 % in B8h and magnesium ranges between 5 % in OU and 8 % in Mix8h.

In addition to elemental information, XPS yields information about the chemical nature of detected elements. Together with XRD and Raman studies suggestions about the compounds and phases present in the bed material ash layers can be made. Table 5.1 summarizes the results of this analysis.

Table 5.1: Phase analysis of bed material ash layer derived by XPS, XRD and Raman

	XPS	XRD	Raman
OU	$CaO, (CO_3)^{-2}$	$C, MgO, CaO, (Ca, Mg)CO_3,$ $Ca(Fe, Mn)(Si, Al)_2O_6$	Fe_2O_3, CaO
CM8h	$CaO, (CO_3)^{-2},$ $CaHPO_4$	$C, MgO, CaO, Ca_2SiO_4,$ $Ca_{10}(PO_4)_6O,$ $Ca(Fe, Mn)(Si, Al)_2O_6,$ $KNaCa_2(PO_4)_2, K_3(MnO_4)_2$	$CaO, (PO_4)^{-3}$ $K_2SO_4, CaCO_3$
B8h	$CaO, (CO_3)^{-2},$ $(PO_4)^{-3}$	$C, CaCO_3, CaSiO_3$	CaO
B32h	$CaO, (PO_4)^{-3}$	$C, CaCO_3, CaSiO_3,$ $Ca(Fe, Mn)(Si, Al)_2O_6, KO_2$	CaO
Mix8h	$(CO_3)^{-2},$ $CaHPO_4$	$C, CaCO_3, (Ca, Mg)CO_3,$ $Ca(Fe, Mn)(Si, Al)_2O_6,$ $KNaCa_2(PO_4)_2, K_3(MnO_4)_2$	$CaO, (PO_4)^{-3},$ $K_2SO_4, CaCO_3$
Mix40h	$(CO_3)^{-2},$ $CaHPO_4$	$C, CaCO_3, KO_3,$ $CaSiO_3, Ca_2SiO_4,$ $Ca_{10}(PO_4)_6O$	$C - deposit$ $CaO, (PO_4)^{-3}$ K_2SO_4

The presence of calcium as metallic calcium in the ash layer of examined bed materials is not only unlikely due to the known high reactivity of alkali metals but also is suggested otherwise by XPS, XRD and Raman results. The occurrence of *CaO* is indicated by all three techniques for OU and CM8h. However, other *Ca*-rich species are indicated: calcium-carbonate, calciumsilicates and calciumphosphates match with spectroscopic findings.

The prevalence of CaO or $CaCO_3$ in wood ash is depending on the combustion temperature. The burning of wood at $600\text{ }^\circ C$ produces $CaCO_3$ and $CaOH$ and no CaO whereas at $1300\text{ }^\circ C$ predominantly CaO and $CaSiO_4$ is formed [91]. Moreover, the calcination rate of $CaCO_3$ to CaO below $800\text{ }^\circ C$ is very low. For a calcite particle of 1 cm to be calcinated at $800\text{ }^\circ C$ it takes > 3 hours [92].

The bed material Olivine used was taken out after 1200 h of a circulating fluidized bed gasification reactor where temperatures $850\text{-}950\text{ }^\circ C$ prevailed [69]. The Feldspar samples (CM8h, B8h, B32h, Mix8h and Mix40h) stem from a fluidized bed combustion reactor with operating temperatures ranging between $730\text{-}830\text{ }^\circ C$ [70].

The 1s oxygen binding energies in PO_4 , SiO_2 and CO_3 lie in the same range wherefore a distinction between these compounds is not possible with XPS. XRD and Raman data suggest the simultaneous existence of both calciumcarbonate and calciumoxide. Furthermore, is the occurrence of calcium as a phosphate strongly indicated for CM8h, Mix8h and Mix40h.

The high phosphorus content in the ash of chicken manure is, however, not reflected in the ash layer of CM8h, Mix8h and Mix40h. A phosphorus content of 25% was estimated in the ash of chicken manure compared to 2% in bark used in B8h and B32h. The outer most layer of CM8h grains comprise 3% of phosphorus compared to 4% in B8h and also 4% in Mix8h. As a consequence it can be concluded that phosphorus is less capable of forming an ash layer around the bed material. Calcium on the other hand accounts for $26\text{ w}\%$ in chicken manure ash and 12% in bark. The XPS results indicate a Ca content of about 21% in CM8h and 14% in B8h and 15% in B32h. Consequently, it can be assumed that the ash layer is therefore more readily formed by calcium than other elements. The increase of Ca in Mix8h of about 17% to 19% in Mix40h further substantiate this claim.

Potassium amounts to 8% in chicken manure ash and 3% in bark ash and was detected only in CM8h $>1\%$ by XPS. Nevertheless, this little amounts of potassium match with results for K_2SO_4 , $KNaCa_2(PO_4)_2$ in CM8h and Mix8h. Magnesium amounts to 5% in bark ash and even 14% in the ash of chicken manure. Ranging between $5\text{-}9\%$ in the surface of the used bed materials magnesium is a significant component. Thus the concentration in the surface reflects well the amount in the ash. XRD measurements further indicate the presence of magnesium as MgO .

Adsorbed methanol and acetic acid vapor on calcium oxide surface verify the presence and accessibility of both Brønsted basic sites and Lewis acidic sites. In the used DRIFTS equipment no adsorption of methanol nor acetic acid was seen on all samples. It is assumed that low surface areas do not allow to produce sufficient adsorbed species to produce a strong reflected IR signal.

Carbon monoxide forms carbonate groups and formate groups on CaO that might be intermediate products in the Water-Gas-Shift-Reaction. CO adsorption on Olivine used indicates the adsorption of carbon monoxide on iron that either stems probably from the mineral structure as the sample was ground and pressed before the measurement. Moreover, CO reacted with CaO to carbonate and formate.

Since CO adsorbed on iron and CaO two reaction mechanisms of the Water-Gas-Shift-Reaction are thinkable. Kul'kova and Temkin [93] propose a stepwise mechanism over iron oxide displayed in Figure 5.2. Prior to carbon monoxide adsorption iron reacts with water to form a hydroxyl group and changes its oxidation state. On interaction with CO a complex is formed whereby the hydrid ion reduces the oxidation state of iron back from (+3) to (+2). Eventually this carboxylate type complex disintegrates into CO_2 and hydrogen.

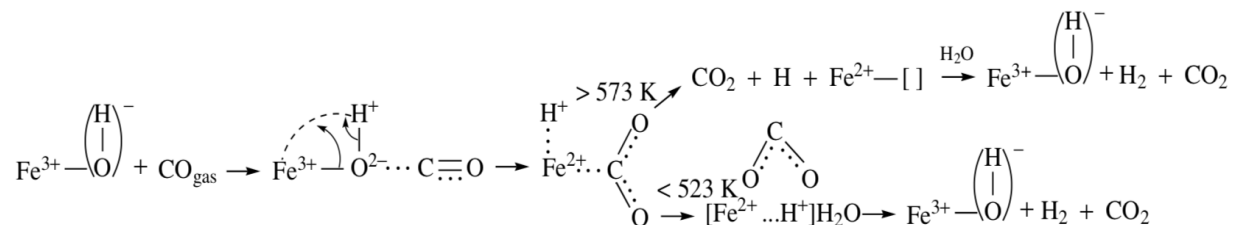


Figure 5.2: WGSR mechanism over a high temperature catalyst: iron oxide [19]

There is not much literature about the WGSR over CaO , however, the chemical similarity of MgO and CaO allow for the subsequent comparison.

Davydov et. al. [94] propose for MgO catalysts a concerted mechanism of the WGSR unlike a stepwise mechanism with iron. IR measurements hereby show the adsorption of water via dissociation with the formation of two types of hydroxyl groups, characterized by bands at 3620 and 3760 cm^{-1} and are displayed in Figure 5.3. Upon reaction with CO gas formate-complexes are formed. Due to the two different types of hydroxyl groups two types of formates was detected with maxima at 1340 and 1390 cm^{-1} (symmetric mode of OCO), 1620 and 1585 cm^{-1} (asymmetric mode of OCO) and 2760 and 2840 cm^{-1} ($C - H$ mode).

At this temperatures the intermediate is formate and the reaction is limited by the decomposition rate of formate into CO_2 and H_2 .

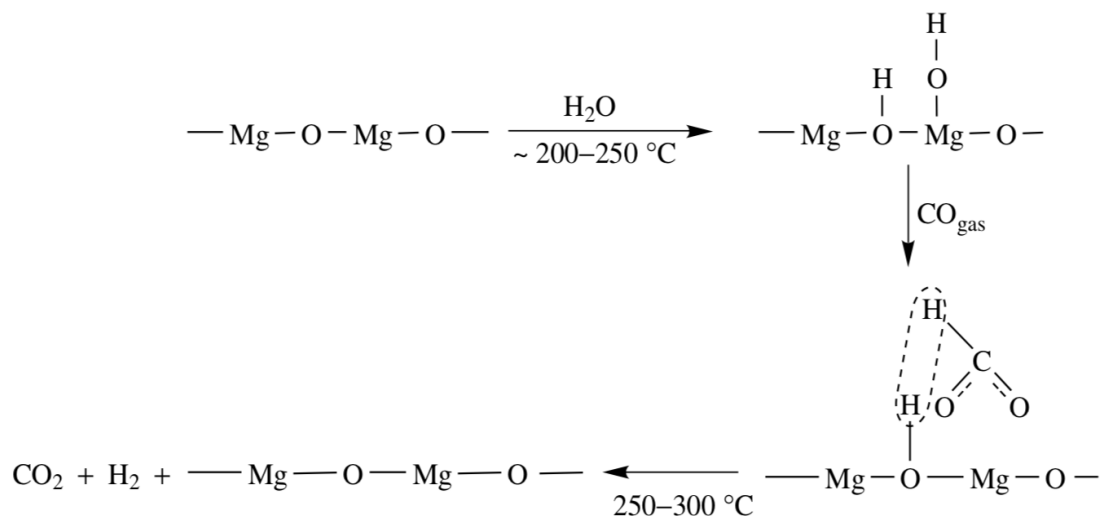


Figure 5.3: WGS mechanism over a middle temperature catalyst: magnesium oxide [19]

Figure 4.18 indicates also as Davydov et. al. two hydroxyl peaks. However, only one peak corresponding to hydroxyl groups is found in *CaO*. The peaks found after *CO* adsorption on Olivine used, Figure 4.25, with maxima at 1595 and 1365 cm^{-1} match perfectly to formate species on *MgO* (considering a slight shift due to adsorption on *CaO* instead of *MgO*).

Since the intermediate species formate was detected by IR measurements on Olivine used the same concerted mechanism of the WGS is presumed to take place (at least at lower temperatures). The reaction behavior at higher temperatures remains, however, unclear. High temperature catalysts such as iron also might play a role in the enhanced product gas qualities of gasification at operating temperatures between 800 - $900\text{ }^\circ\text{C}$.

Conclusion and outlook

BET surface areas were found to be increased of ash layered bed material grains compared to fresh bed material. Further, a clear trend towards higher surface areas with higher reactor residence time was observed. Moreover, grains out of fluidized bed reactors operated with fuels with high ash contents, such as chicken manure, exhibit higher surface areas compared to fuels with a low ash content, such as bark.

Surface analysis discloses similar oxygen (43-53 %), calcium (14-21 %) and magnesium (5-9 %) concentrations in the outer most nanometers in all examined used bed materials: Olivine used 1200 *h* and logging residues, Feldspar chicken manure 8 *h*, Feldspar bark 8 *h*, Feldspar bark 32 *h*, Feldspar chicken manure and bark 8 *h* and 40 *h*. By means of different analysis techniques varied information depths are accessible. However, only XPS yields relatively good accuracy towards elemental distribution as EDX and XRF under- or overestimate certain elements. Internal standards have to be used for these techniques.

Corresponding with high phosphorus concentrations in ash of chicken manure, bed materials taken out of reactors fueled solely or in blends with chicken manure show high *P*-concentrations. The collected data suggests phosphorus occurring as phosphate and as calciumphosphate.

Only calcium and magnesium reflect the ash composition in the outer most ash layer of the bed material suggesting good efficiencies for the formation of an ash layer around Olivine and Feldspar. The composition of the ash layer caused by fuel mixtures roughly represent the mixture. Phase analysis estimates the presence of calcium predominantly as *CaO* and *CaCO₃*. Together with literature indicate the findings the decline of *CaCO₃* quantities towards *CaO* which is believed to be more catalytically active due to increased basicity.

Successful adsorption of both acetic acid and methanol substantiates the presence and accessibility of Brønsted basic sites and Lewis acid sites on *CaO*. The positive adsorption of carbon monoxide on pure *CaO* and Olivine used disclose the formation of formate species on the surface. The formate complex is believed to be an intermediate product in the Water-Gas-Shift-Reaction.

However, further investigations are necessary to uncover the reaction mechanism of the WGSR on ash layered bed material grains. This is to be done by carrying out simultaneous or sequential adsorption of *H₂O* and *CO* and by further analysing active sites by probe molecules such as ammonia or pyridine. Moreover, studies by UV spectroscopy could uncover more details of adsorbed probe molecules. By titration of probe molecules the number of active sites could be determined as the first step to increase its number on low surface areas.

Bibliography

- [1] L. Matsakas, Q. Gao, S. Jansson, U. Rova, and P. Christakopoulos. Green conversion of municipal solid wastes into fuels and chemicals. *Electronic Journal of Biotechnology*, 26(January):69–83, 2017.
- [2] P. Basu. *Biomass gasification and pyrolysis: practical design and theory*, Elsevier Inc. 2010.
- [3] M. Kaltschmitt, H. Hartmann, and H. Hofbauer. *Energie aus Biomasse Grundlagen, Techniken und Verfahren*, volume 53. 2013.
- [4] Fledged.eu. fledged.eu/biomass-to-dme-process/gasification-2/ (accessed may 2019).
- [5] Hermann Hofbauer. Working group Gasification & Gas Cleaning. *Achema*, 2012.
- [6] Jitka Hrbek. Status report on thermal biomass gasification in countries participating - IEA Bioenergy, Task 33. (April):163, 2016.
- [7] Matthias Kuba, Friedrich Kirnbauer, and Hermann Hofbauer. Influence of coated olivine on the conversion of intermediate products from decomposition of biomass tars during gasification. *Biomass Conversion and Biorefinery*, 7(1):11–21, 2017.
- [8] I. Chorkendorff and J. W. Niemantsverdriet. *Concepts of Modern Catalysis and Kinetics*, 2nd edition. 2007.
- [9] White Points and Appendix A Color Matching. Gernot Hoffmann CIE Color Space. 1931.
- [10] Lisbonlx.com. Electron interactions with matter (accessed May 2019).
- [11] Robert Hurt. *Electron Emission Mechanisms*, 2016.
- [12] Matthias Thommes, Katsumi Kaneko, Alexander V. Neimark, James P. Olivier, Francisco Rodriguez-Reinoso, Jean Rouquerol, and Kenneth S.W. Sing. Physisorption of gases, with special reference to the evaluation of surface area and pore size distribution (IUPAC Technical Report). *Pure and Applied Chemistry*, 87(9-10):1051–1069, 2015.
- [13] Helmut Fischer. <https://xrf-spectroscopy.com> (accessed may 2019).
- [14] I. Yut, A. Bernier, and A. Zofka. Development of a compact laboratory aging procedure for asphalt binders. *Asphalt Paving Technology: Association of Asphalt Paving Technologists-Proceedings of the Technical Sessions*, 81(May 2016), 2012.

-
- [15] T. Vankeirsbilck, A. Vercauteren, Willy Baeyens, G. Van der Weken, F. Verpoort, G. Vergote, and J. P. Remon. Applications of Raman spectroscopy in pharmaceutical analysis. *TrAC - Trends in Analytical Chemistry*, 21(12):869–877, 2002.
- [16] Mohammad Javad Jafari. Application of Vibrational Spectroscopy in Organic Electronics. (1884):61, 2017.
- [17] <https://myscope.training/legacy/analysis/introduction> (accessed May 2019). Micro-analysis methods overview, 2016.
- [18] Edoardo Garrone, Adriano Zecchina, and Frank S Stone. CO Adsorption on MgO and CaO. 84(8):2843–2854, 1988.
- [19] Anatoli Davydov. *Molecular spectroscopy of oxide catalyst surfaces*, volume 33. 2003.
- [20] Chundi Cao and Keith L. Hohn. Study of reaction intermediates of methanol decomposition and catalytic partial oxidation on Pt/Al₂O₃. *Applied Catalysis A: General*, 354(1-2):26–32, 2009.
- [21] Ben B. Chastain. Jan Baptista van Helmont. *Encyclopædia Britannica*, 2019.
- [22] Wien.gv.at (accessed May 2019). Historischer Rückblick der Rathauskorrespondenz vom April 1952.
- [23] Ewald Frühwirth. Die Technik im Wiener Gasometer <http://www.gasometer-city.eu/technik.htm> (accessed May 2019).
- [24] B.H. Davis and M.L. Occelli. *Fischer-Tropsch Synthesis, Catalysts and Catalysis*. Elsevier Science, 2006.
- [25] EIA. U.S. Energy Information Administration, International Energy Outlook. 2016.
- [26] B. Lang. Marktanalyse Energieholz Energiebilanz der Holzsortimente. pages 1–12, 2014.
- [27] Friedrich Kirnbauer and Hermann Hofbauer. Investigations on bed material changes in a dual fluidized bed steam gasification plant in Güssing, Austria. *Energy and Fuels*, 25(8):3793–3798, 2011.
- [28] Katharina Wagner, Anna Magdalena Mauerhofer, Matthias Kuba, and Hermann Hofbauer. Suitability of K-feldspar as Alternative Bed Material in Dual Fluidized Bed Steam Gasification in Combination with Ash-Rich Feedstocks. *Proceedings of the 23rd International Conference on FBC*, 2018.
- [29] Peter Atkins and de Paula Julio. *Physical Chemistry*. Oxford University Press, 8th editio edition, 2006.
- [30] IEA Bioenergy Task 33. Gasification of Biomass and Waste. *IEA Bioenergy Fact sheets*, 2018.
- [31] Basu Prabir and A. Sarkat. Agglomeration of coal ash in fluidized beds. *City*, 62:924–926, 1983.

- [32] T a Milne and R J Evans. Biomass gasifier tars: their nature , formation , and conversion; Report NREL/TP-570-25357; National Renewable Energy Laboratory (NREL): Golden, CO, 1998. *Golden Colorado: National Renewable Energy Laboratory*, (November):v, 1998.
- [33] IEA Task 33. *Gasification of waste for energy carriers*. 2018.
- [34] Nath Kaushik and Das Debabrata. *Hydrogen from biomass*. 2018.
- [35] Yoshiro Morita and Ken-ichi Yamamoto. Production of City Gas from Heavy Oil by Catalytic Treatment. *Bulletin of The Japan Petroleum Institute*, 2:19–24, 1960.
- [36] David Sutton, Brian Kelleher, and Julian R H Ross. 2001-SuttonKelleherRoss-Review of literature on catalysts for biomass gasification.pdf. 2001.
- [37] Pekka A. Simell, Jukka K. Leppälähti, and J. B. son Bredenberg. Catalytic purification of tarry fuel gas with carbonate rocks and ferrous materials. *Fuel*, 71(2):211–218, 1992.
- [38] Jesús Delgado, Maria P. Aznar, and José Corella. Calcined dolomite, magnesite, and calcite for cleaning hot gas from a fluidized bed biomass gasifier with steam: Life and usefulness. *Industrial and Engineering Chemistry Research*, 35(10):3637–3643, 1996.
- [39] A. Chopelas. Single crystal Raman spectra of forsterite, fayalite, and monticellite. *American Mineralogist*, 76(7-8):1101–1109, 1991.
- [40] S. Rapagnà, N. Jand, A. Kiennemann, and P. U. Foscolo. Steam-gasification of biomass in a fluidised-bed of olivine particles. *Biomass and Bioenergy*, 19(3):187–197, 2000.
- [41] Friedrich Kirnbauer, Veronika Wilk, Hannes Kitzler, Stefan Kern, and Hermann Hofbauer. The positive effects of bed material coating on tar reduction in a dual fluidized bed gasifier. *Fuel*, 95(2012):553–562, 2012.
- [42] Elisabet Brus, Marcus Öhman, and Anders Nordin. Mechanisms of bed agglomeration during fluidized-bed combustion of biomass fuels. *Energy and Fuels*, 19(3):825–832, 2005.
- [43] R.L. Rudnick and S. Gao. Composition of the continental crust. *Treatise on geochemistry*, Vol 3, 2003.
- [44] Nicolas Berguerand, Jelena Marinkovic, Teresa Berdugo Vilches, and Henrik Thunman. Use of alkali-feldspar as bed material for upgrading a biomass-derived producer gas from a gasifier. *Chemical Engineering Journal*, 295:80–91, 2016.
- [45] Nicolas Berguerand and Teresa Berdugo Vilches. Alkali-Feldspar as a Catalyst for Biomass Gasification in a 2-MW Indirect Gasifier. *Energy and Fuels*, 31(2):1583–1592, 2017.
- [46] K. Wagner, G. Häggström, A. Mauerhofer, M. Kuba, N. Skoglund, M. Öhman, and H. Hofbauer. Layer formation on K-feldspar in fluidized bed combustion and gasification of bark and chicken manure. *Biomass and Bioenergy*, 127(April 2019):105251, 2019.
- [47] Katharina Wagner, Gustav Häggström, and Nils Skoglund. Layer Formation Mechanism of K-feldspar in Bubbling Fluidized Bed Combustion of Phosphorus-lean and Phosphorus-rich Residual Biomass. 2020.

- [48] Marcus Öhman, Linda Pommer, and Anders Nordin. Bed agglomeration characteristics and mechanisms during gasification and combustion of biomass fuels. *Energy and Fuels*, 19(4):1742–1748, 2005.
- [49] Friedrich Kirnbauer and Hermann Hofbauer. The mechanism of bed material coating in dual fluidized bed biomass steam gasification plants and its impact on plant optimization. *Powder Technology*, 245(2013):94–104, 2013.
- [50] Matthias Kuba, Fabian Havlik, Friedrich Kirnbauer, and Hermann Hofbauer. Influence of bed material coatings on the water-gas-shift reaction and steam reforming of toluene as tar model compound of biomass gasification. *Biomass and Bioenergy*, 89(2016):40–49, 2015.
- [51] Christoph Hammerl. Time-dependent catalytic activity of used K-Feldspar for biomass gasification. 2019.
- [52] Nader Padban. *PFB Air Gasification of Biomass: Investigation of product formation and problematic issues related to ammonia, tar and alkali*. PhD thesis, Lund University, 2000.
- [53] Anthony A. Lizzio and Ljubisa R. Radovic. Transient Kinetics Study of Catalytic Char Gasification in Carbon Dioxide. *Industrial and Engineering Chemistry Research*, 30(8):1735–1744, 1991.
- [54] D. W. McKee and D. Chatterji. The catalytic behavior of alkali metal carbonates and oxides in graphite oxidation reactions. *Carbon*, 13(5):381–390, 1975.
- [55] Xianbin Xiao, Xianliang Meng, Duc Dung Le, and Takayuki Takarada. Two-stage steam gasification of waste biomass in fluidized bed at low temperature: Parametric investigations and performance optimization. *Bioresource Technology*, 102(2):1975–1981, 2011.
- [56] C Pfeifer, R Rauch, and H Hofbauer. Hydrogen-Rich Gas Production with a Catalytic Dual Fluidized Bed Biomass gasifier. *Second World Conference and Technology Exhibition on Biomass for Energy, Industry and Climate Protection*, 2004.
- [57] Janos Schanda. *Colorimetry - Understanding the CIE System*. John Wiley & Sons, 2007.
- [58] Henning Bubert, John C Rivi È Re, Wolfgang S M Werner, and Gernot Friedbacher. *Surface and Thin Film Analysis*. Wiley VCH, Weinheim, Germany, 2nd edition, 2011.
- [59] S. Lowell, Joan E. Shields, and J. E. Morral. *Powder Surface Area and Porosity, 2nd Edition*, volume 107. 2009.
- [60] Stephen Brunauer, P.H. Emmet, and E. Teller. Adsorption of Gases in Multimolecular Layers. *Adsorption of Gases in Multimolecular Layers*, 407(1), 1936.
- [61] Alex Klockenkämper and Reinhold Bohlen. *Total-Reflection X-Ray Fluorescence Analysis and Related Methods*. John Wiley & Sons, Inc, 2015.
- [62] H Beckhoff, B Kanngießer, N Langhoff, R Wedell, and H Wolff. *Handbook of Practical X-Ray Fluorescence Analysis*. Springer Vieweg, Berlin Heidelberg, 2006.

- [63] U S Department of Energy National Laboratory Managed by the University of California. http://henke.lbl.gov/optical_constants/atten2.html.
- [64] B. Stuart and Series Preface. *Infrared Spectroscopy: Fundamentals and Applications*, volume 8. 2004.
- [65] G Gauglitz and T Vo-Dinh. *Handbook of Spectroscopy*. Wiley VCH, 2003.
- [66] Mark B. Mitchell. Fundamentals and Applications of Diffuse Reflectance Infrared Fourier Transform (DRIFT) Spectroscopy. pages 351–375, 1993.
- [67] Ewan Smith and Geoffrey Dent. *Review - Modern Raman Spectroscopy: A Practical Approach*, volume 78. 2005.
- [68] C. Bohren and D. Huffman. *Absorption and Scattering of Light by Small Particles*. John Wiley & Sons, Inc, 1983.
- [69] Matthias Kuba, Hanbing He, Friedrich Kirnbauer, Dan Boström, Marcus Öhman, and Hermann Hofbauer. Deposit build-up and ash behavior in dual fluid bed steam gasification of logging residues in an industrial power plant. *Fuel Processing Technology*, 139(2015):33–41, 2015.
- [70] Katharina Wagner, Gustav Häggström, Nils Skoglund, Juraj Priscak, Matthias Kuba, Marcus Öhman, and Hermann Hofbauer. Layer formation mechanism of K-feldspar in bubbling fluidized bed combustion of phosphorus-lean and phosphorus-rich residual biomass. *Applied Energy*, 248(April 2019):545–554, 2019.
- [71] Lopamudra Devi, Menno Craje, Peter Thüne, Krzysztof J. Ptasinski, and Frans J.J.G. Janssen. Olivine as tar removal catalyst for biomass gasifiers: Catalyst characterization. *Applied Catalysis A: General*, 294(1):68–79, 2005.
- [72] I Dubois, S Holgersson, S. Allard, and M.E. Malmstrom. Correlation between particle size and surface area for chlorite and K-feldspar. *Water-Rock Interaction*, pages 717–720, 2010.
- [73] M C Biesinger. www.XPSfitting.com.
- [74] V G Escalab. Curve Fitting and Polymers (accessed June 2019). www.casaxps.com, (Figure 1):1–19, 2011.
- [75] Takashi MOURI and Masaki ENAMI. Raman spectroscopic study of olivine-group minerals. *Journal of Mineralogical and Petrological Sciences*, 103(2):100–104, 2008.
- [76] J Freeman, E Kuebler, L Jolliff, and A Haskin. Characterization of Natural Feldspars By Raman Spectroscopy for Future Planetary Exploration. 46:1477–1500, 2008.
- [77] Victor Zymła and Frederic Honnart. Coke Oven Carbon Deposits Growth and Their Burning Off. *ISIJ International*, 47(10):1422–1431, 2007.
- [78] G. Penel, G. Leroy, C. Rey, and E. Bres. MicroRaman spectral study of the PO₄ and CO₃ vibrational modes in synthetic and biological apatites. *Calcified Tissue International*, 63(6):475–481, 1998.

- [79] Kawther Ben Mabrouk, Thomas H. Kauffmann, Hassen Aroui, and Marc D. Fontana. Raman study of cation effect on sulfate vibration modes in solid state and in aqueous solutions. *Journal of Raman Spectroscopy*, 44(11):1603–1608, 2013.
- [80] Rruff.info. <http://rruff.info/Quartz> (accessed June 2019).
- [81] Konstantin D. Litasov and Nikolay M. Podgornykh. Raman spectroscopy of various phosphate minerals and occurrence of tuite in the Elga IIE iron meteorite. *Journal of Raman Spectroscopy*, 48(11):1518–1527, 2017.
- [82] Miguel Galván-Ruiz, Juan Hernández, Leticia Baños, Joaquín Noriega-Montes, and Mario E. Rodríguez-García. Characterization of Calcium Carbonate, Calcium Oxide, and Calcium Hydroxide as Starting Point to the Improvement of Lime for Their Use in Construction. *Journal of Materials in Civil Engineering*, 21(11):694–698, 2009.
- [83] Liga Berzina-Cimdina and Natalija Borodajenko. Research of Calcium Phosphates Using Fourier Transform Infrared Spectroscopy. *Infrared Spectroscopy - Materials Science, Engineering and Technology*, 2012.
- [84] C G Albuquerque, Inmaculada Jime, Josefa M Me, Antonio Jime, and Pedro Maireles-torres. CaO supported on mesoporous silicas as basic catalysts for transesterification reactions. 334:35–43, 2008.
- [85] Guido Busca. Infrared studies of the reactive adsorption of organic molecules over metal oxides and of the mechanisms of their heterogeneously-catalyzed oxidation. *Catalysis Today*, 27(3-4):457–496, 1996.
- [86] Andreas Haghofer, Davide Ferri, Karin Föttinger, and Günther Rupprechter. Who is doing the job? Unraveling the role of Ga₂O₃ in methanol steam reforming on Pd₂Ga/Ga₂O₃. *ACS Catalysis*, 2(11):2305–2315, 2012.
- [87] George Socrates. *Infrared and Raman Characteristic Group Frequencies Contents*. 2001.
- [88] R Pestman, R M Koster, A Van Duijne, J A Z Pieterse, and V Ponec. Reactions of Carboxylic Acids on Oxides. 272:265–272, 1997.
- [89] Qingxin Ma, Yongchun Liu, Chang Liu, and Hong He. Heterogeneous reaction of acetic acid on MgO, alpha-Al₂O₃, and CaCO₃ and the effect on the hygroscopic behaviour of these particles. *Physical Chemistry Chemical Physics*, 14(23):8403–8409, 2012.
- [90] M J Heal, E C Leisegang, and R G Torrington. Infrared Studies of Carbon Monoxide and Hydrogen Adsorbed on Silica-Supported Iron and Cobalt Catalysts. 325(1978):314–325, 2020.
- [91] Mahendra K. Misra, Kenneth W. Ragland, and Andrew J. Baker. Wood ash composition as a function of furnace temperature. *Biomass and Bioenergy*, 4(2):103–116, 1993.
- [92] C. C. Furnas. The Rate of Calcination of Limestone. *Industrial and Engineering Chemistry*, 23(5):534–538, 1931.
- [93] M. I. Kul'kova, N. V. Temkin. Kinetics of the reaction of the conversion of CO by water vapor, Zh. Fiz. Khim. (in Russian); Russ. J. Phys. Chem. (English translation), 1949.

-
- [94] N. A. Davydov, A. A., Boreskov, G. K., Yurieva, T. M. and Rubene. Associative mechanisms of the water-gas shift reaction of CO. *Dokl. AN SSSR (in Russian); Proc. AN USSR, (English translation)*, pages 1402–1405, 1977.

Appendix

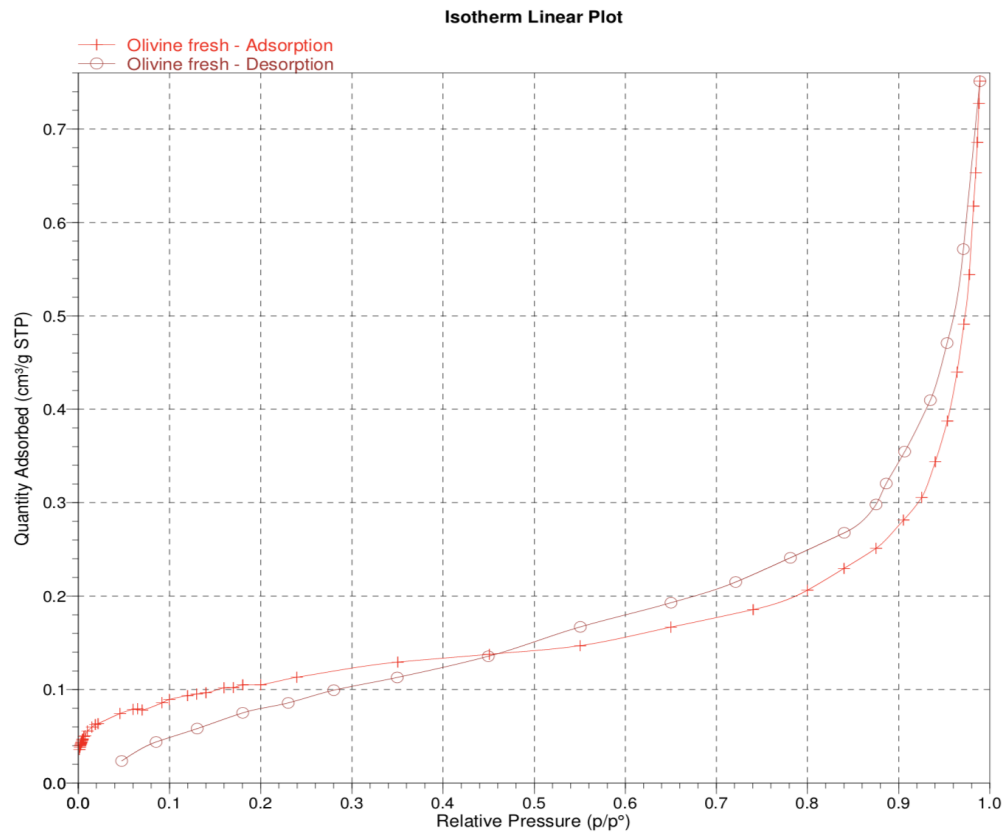


Figure 7.1: Isotherm plot Olivine fresh

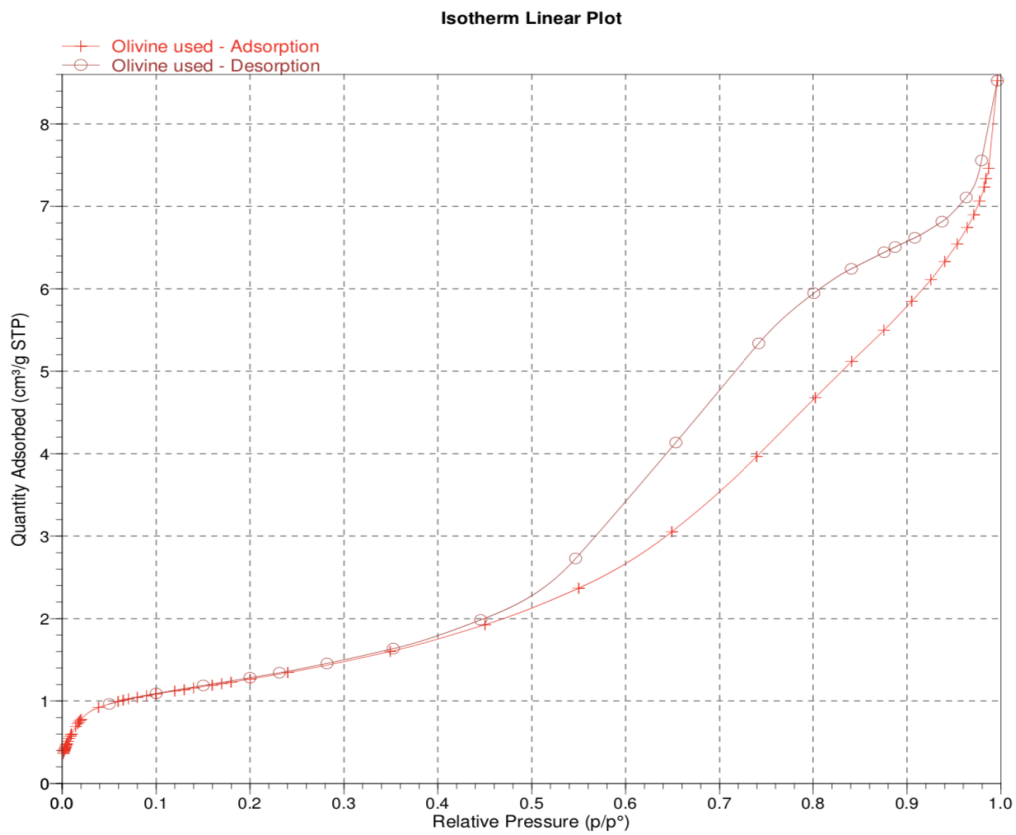


Figure 7.2: Isotherm plot Olivine used

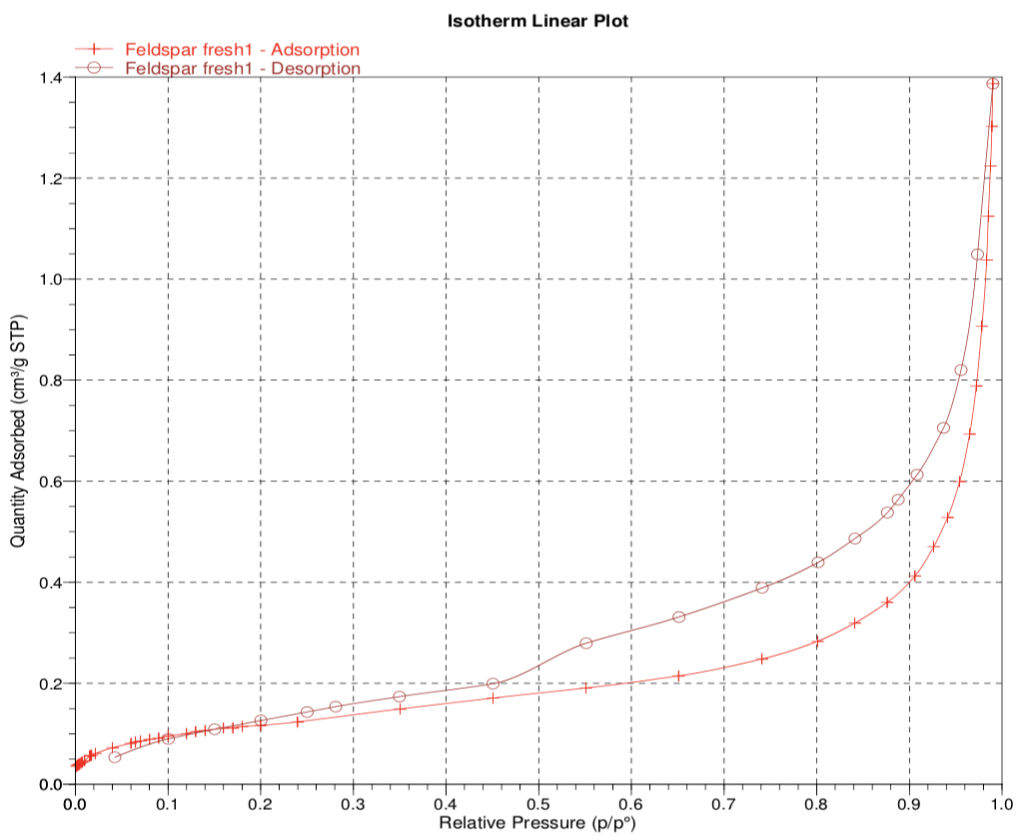


Figure 7.3: Isotherm plot Feldspar fresh

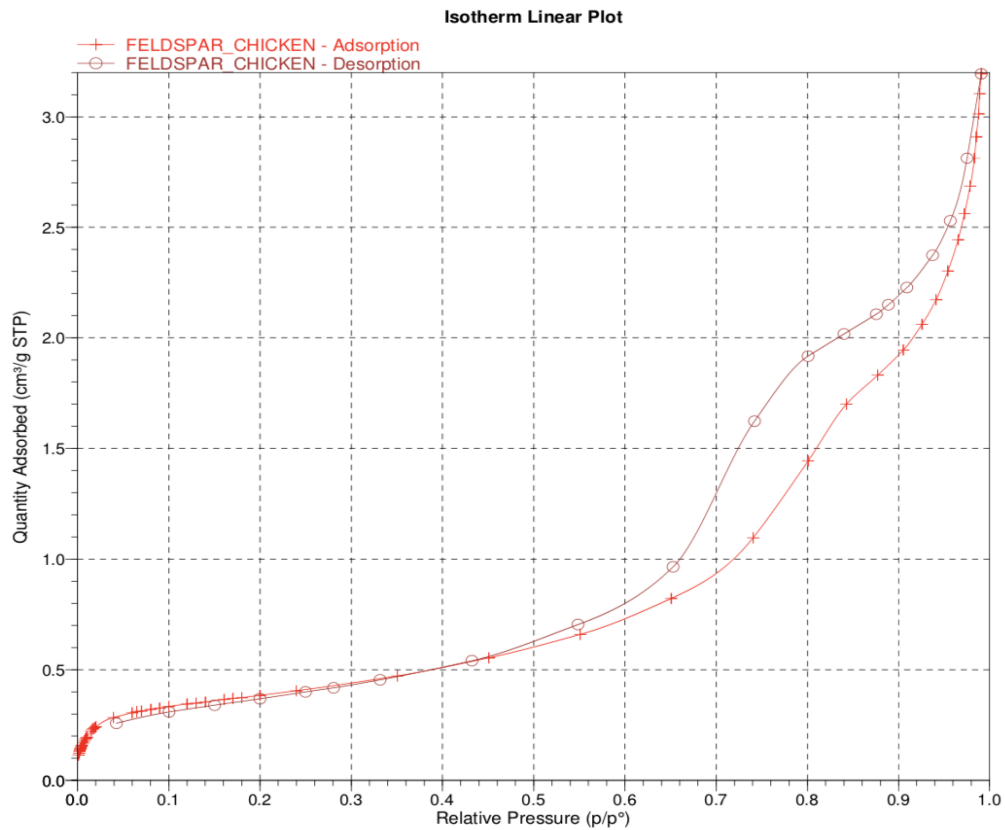


Figure 7.4: Isotherm plot Feldspar CM8h

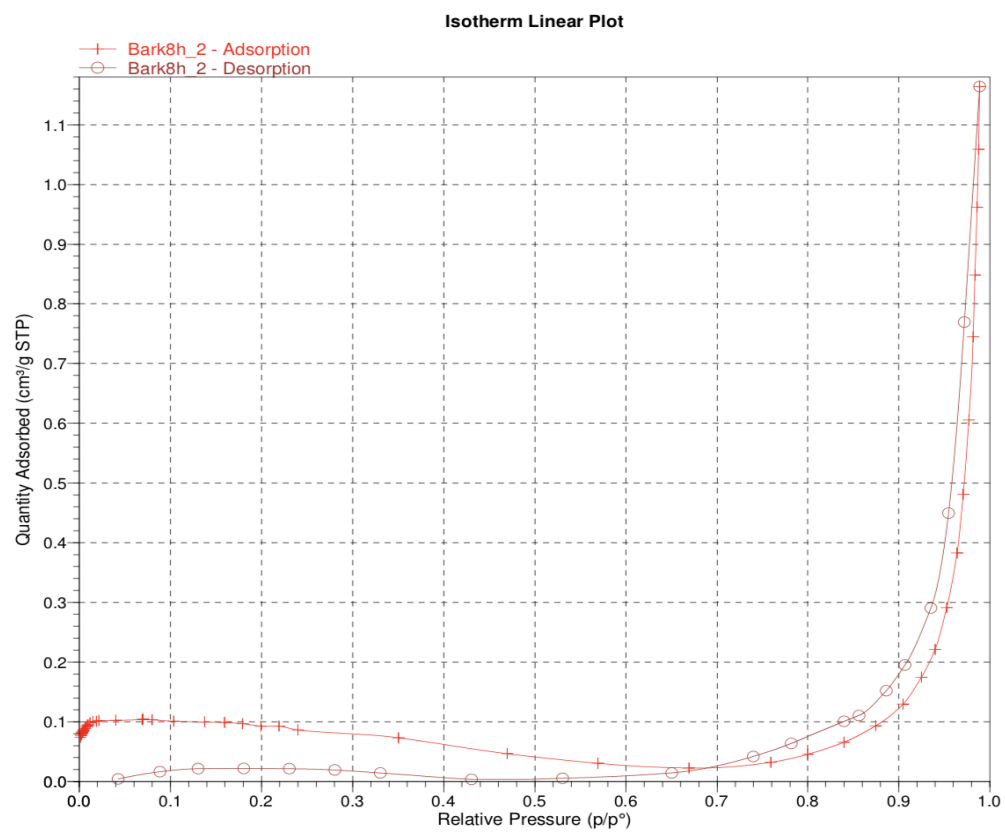


Figure 7.5: Isotherm plot Feldspar B8h

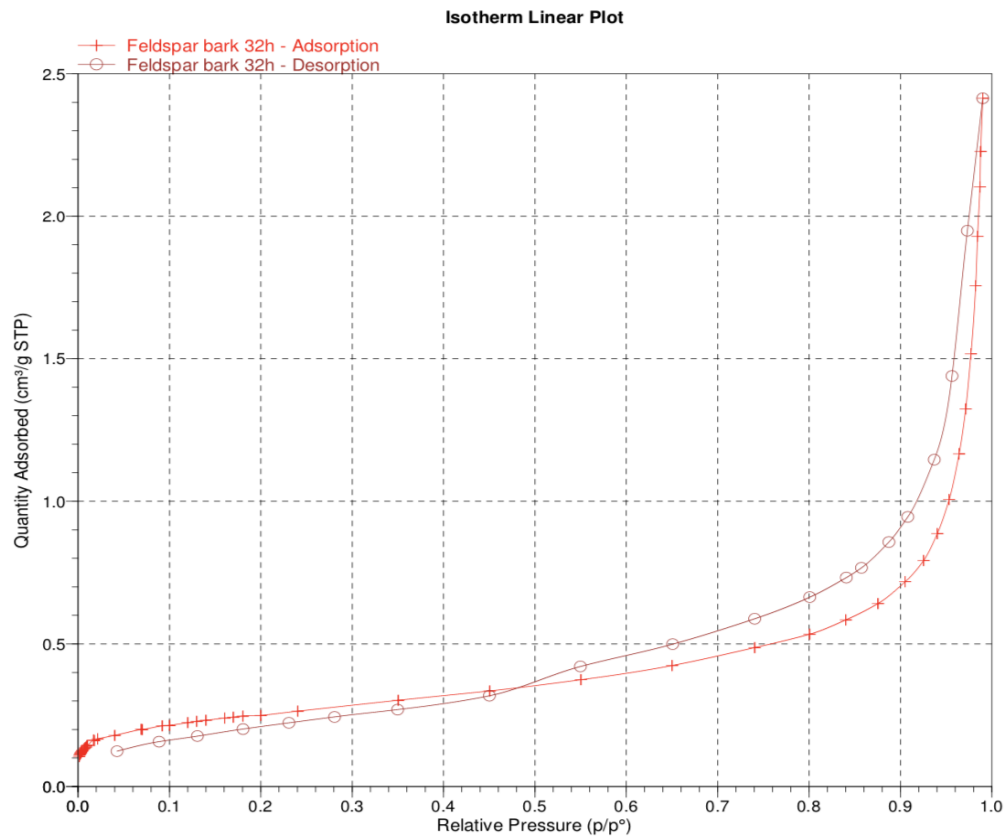


Figure 7.6: Isotherm plot Feldspar B32h

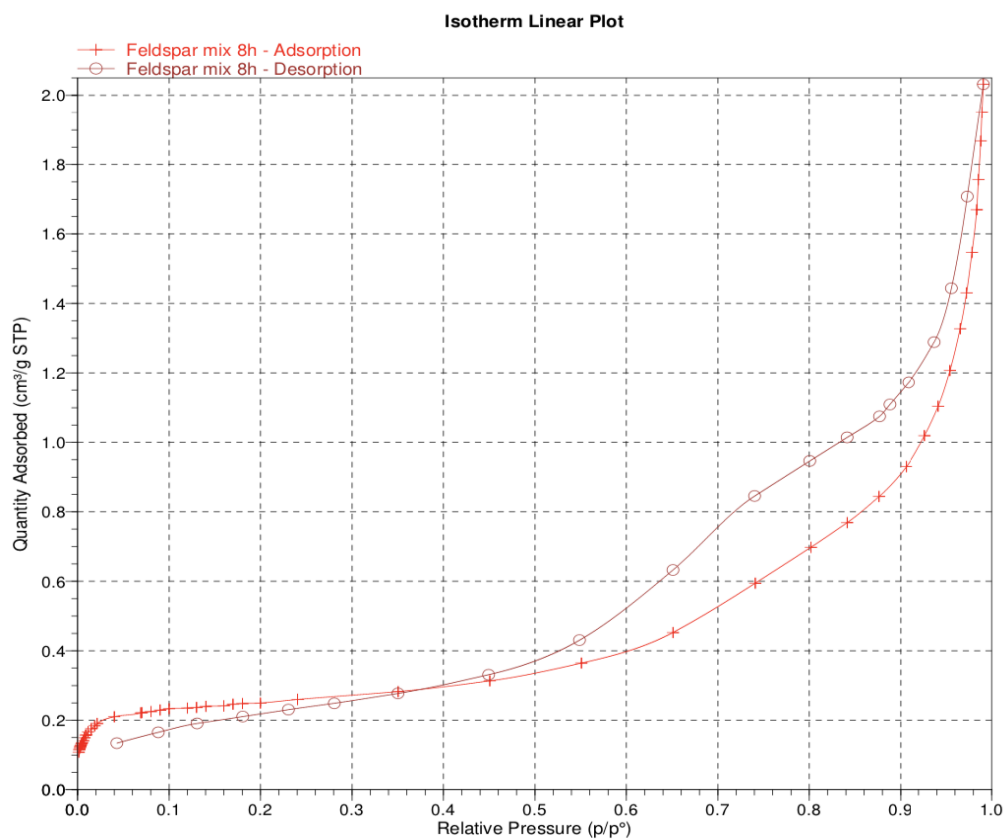


Figure 7.7: Isotherm plot Feldspar Mix8h

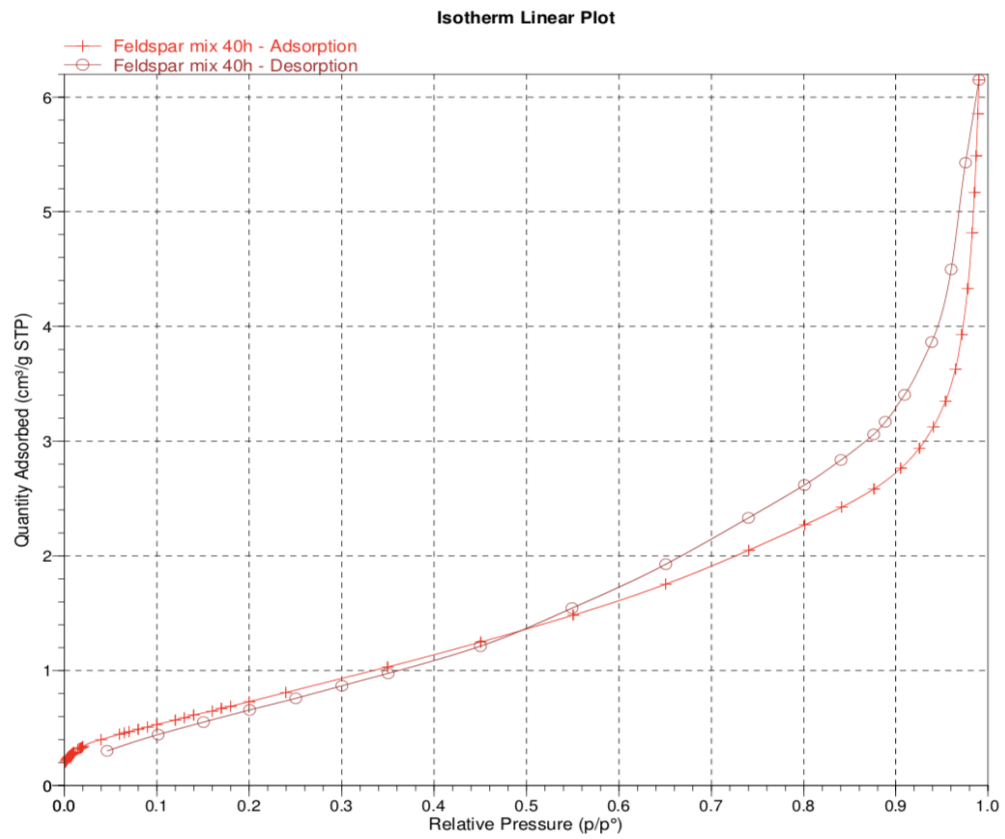


Figure 7.8: Isotherm plot Feldspar Mix40h

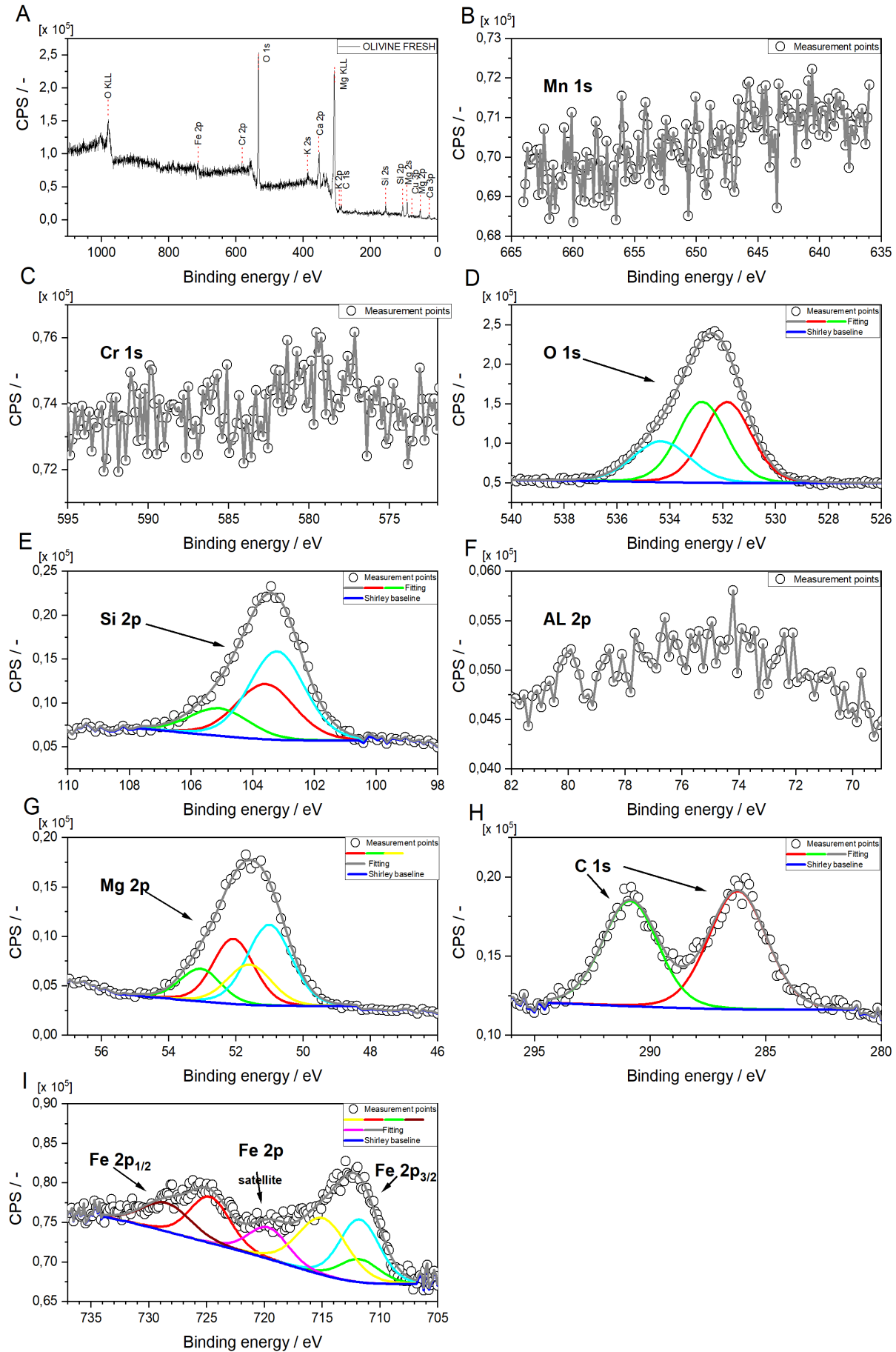


Figure 7.9: Olivine fresh XPS high resolution spectra

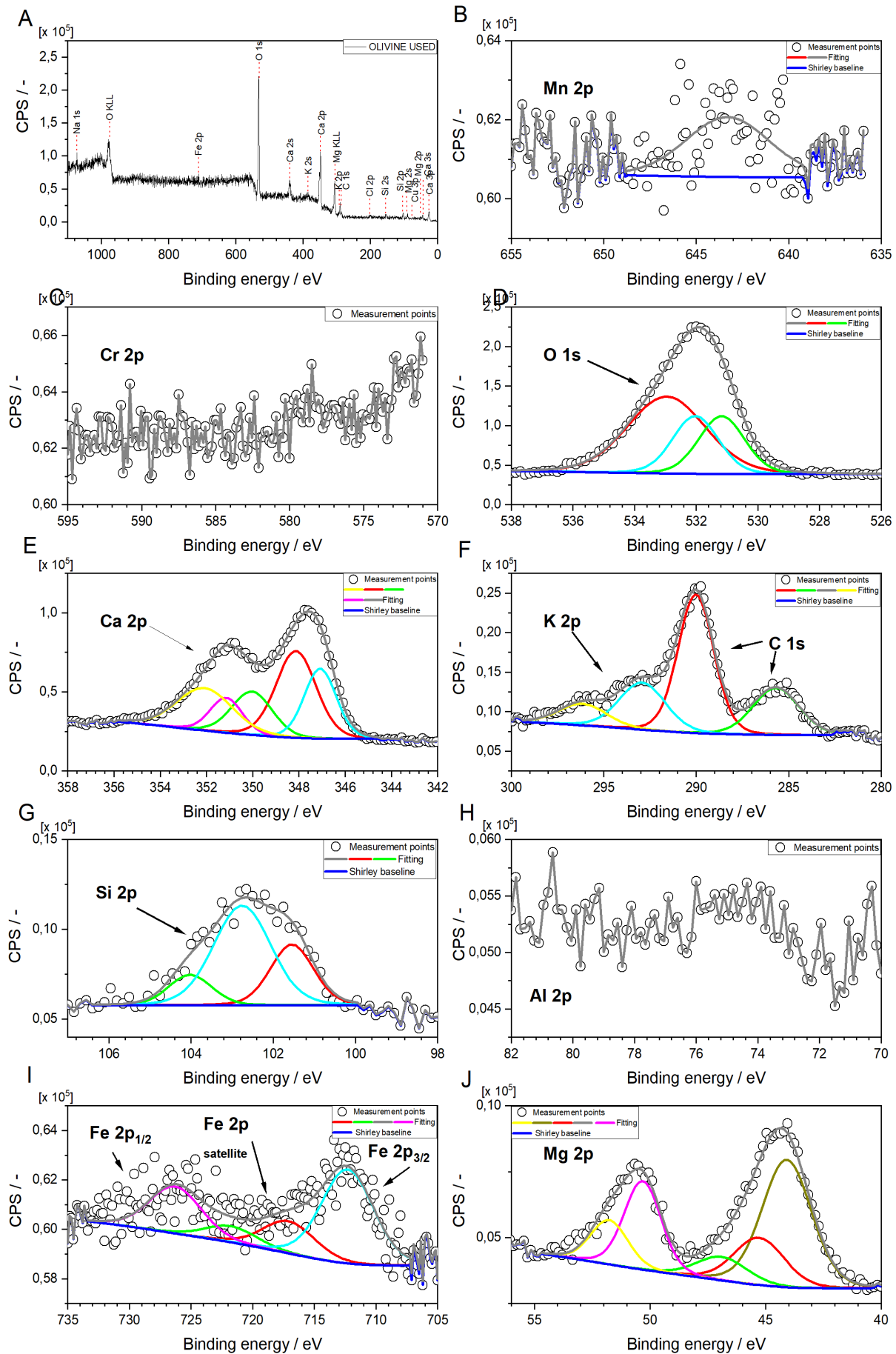


Figure 7.10: Olivine used XPS high resolution spectra

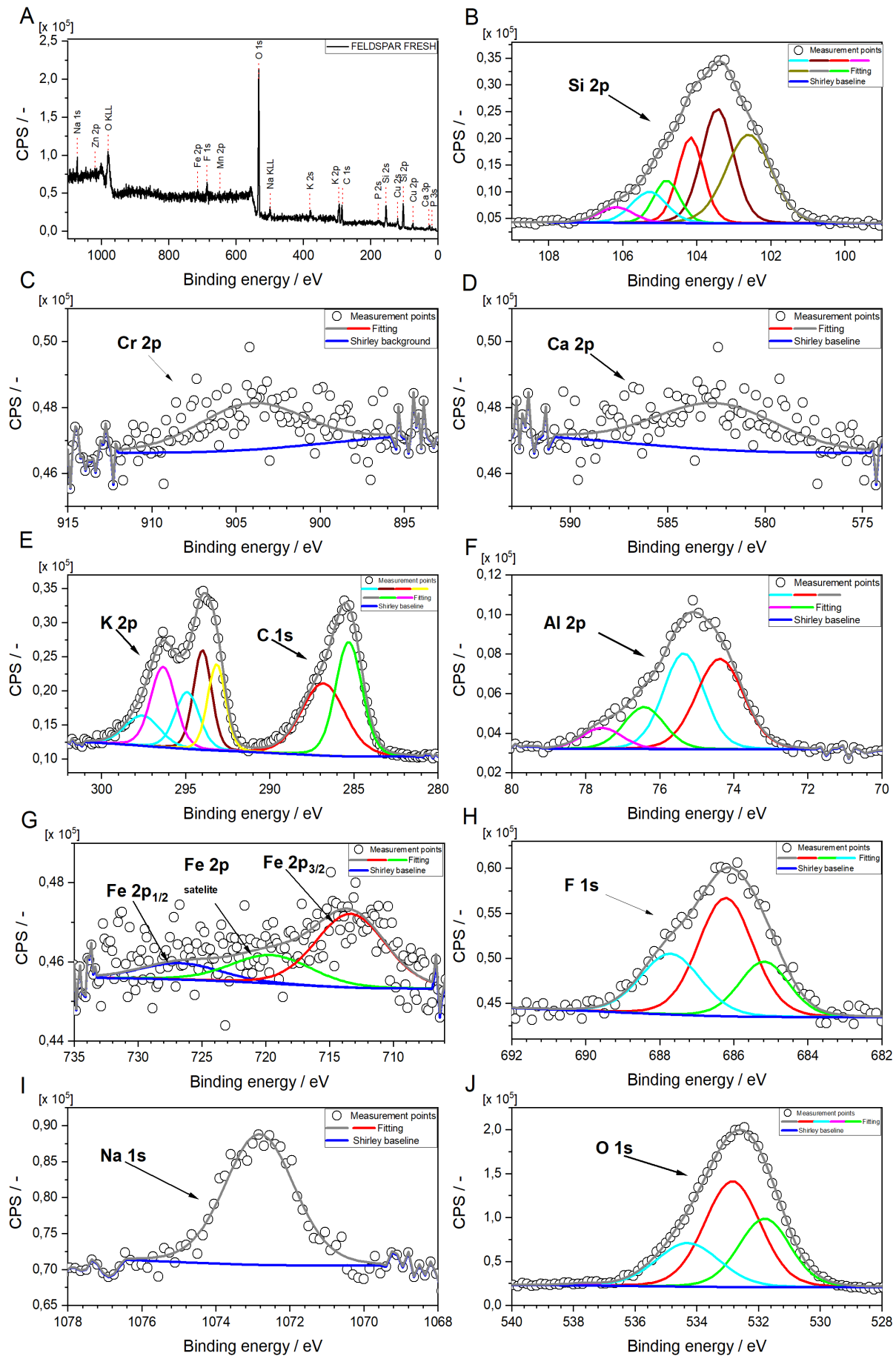


Figure 7.11: Feldspar fresh XPS high resolution spectra

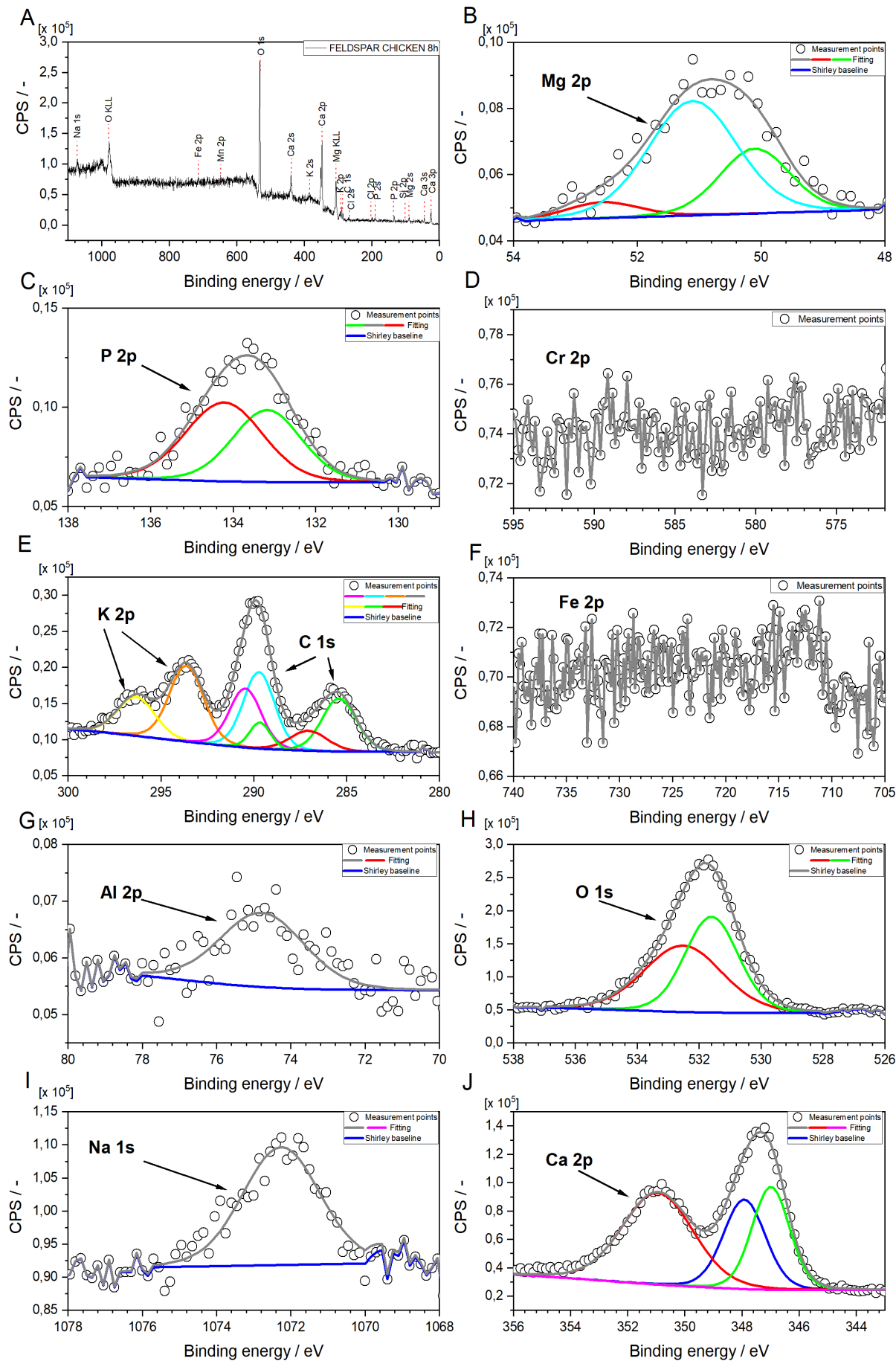


Figure 7.12: Feldspar CM8h XPS high resolution spectra

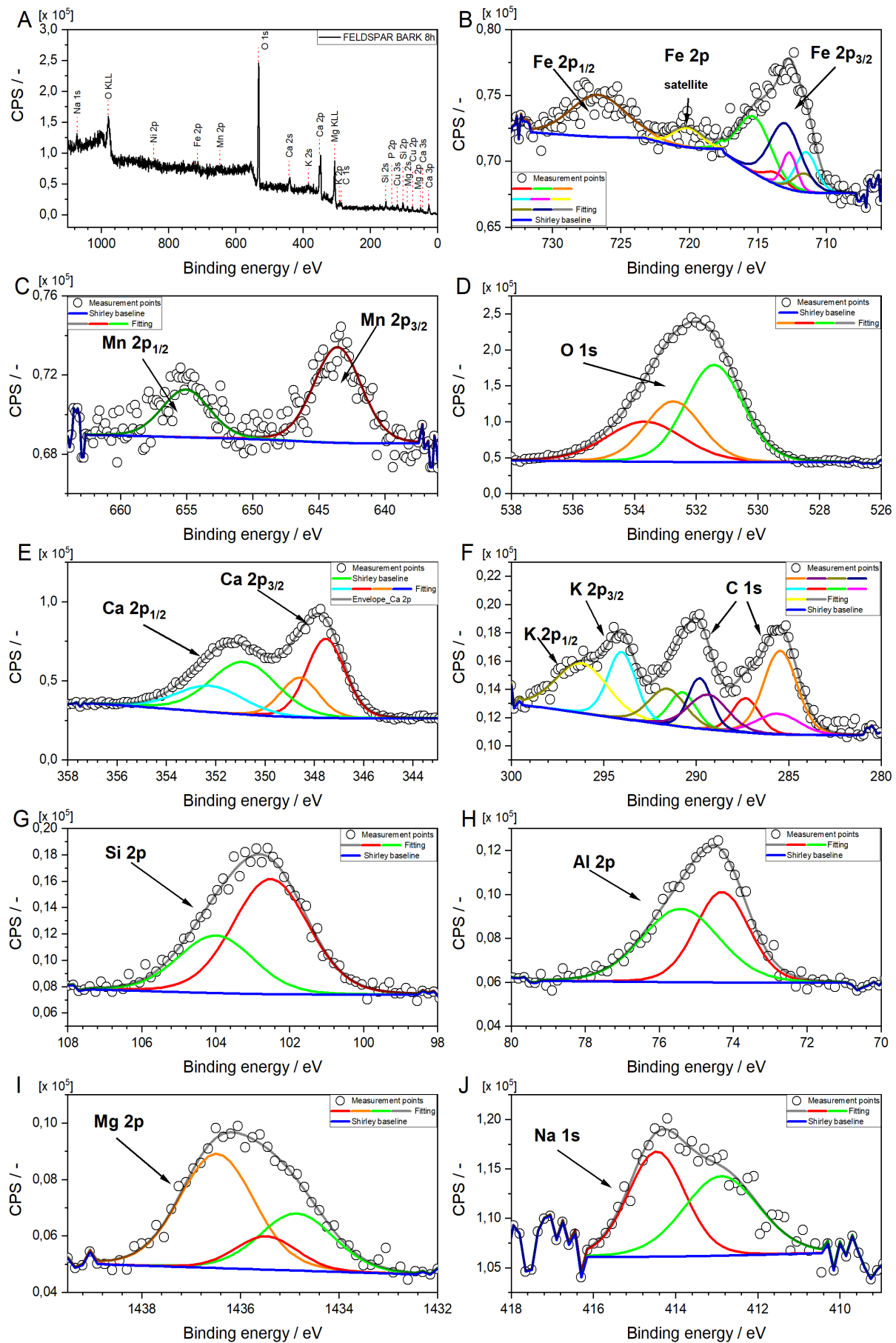


Figure 7.13: Feldspar B8h XPS high resolution spectra

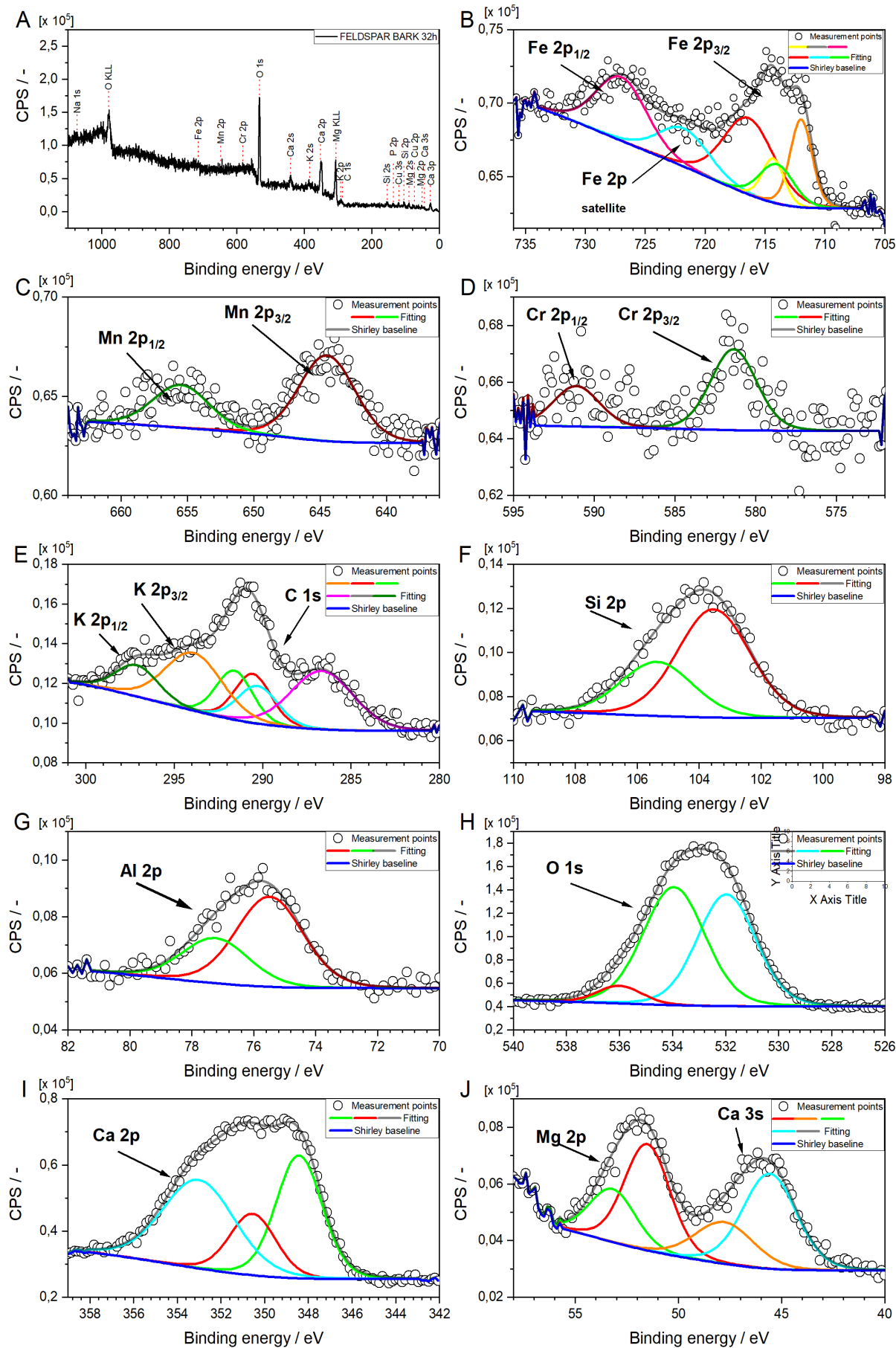


Figure 7.14: Feldspar B32h XPS high resolution spectra

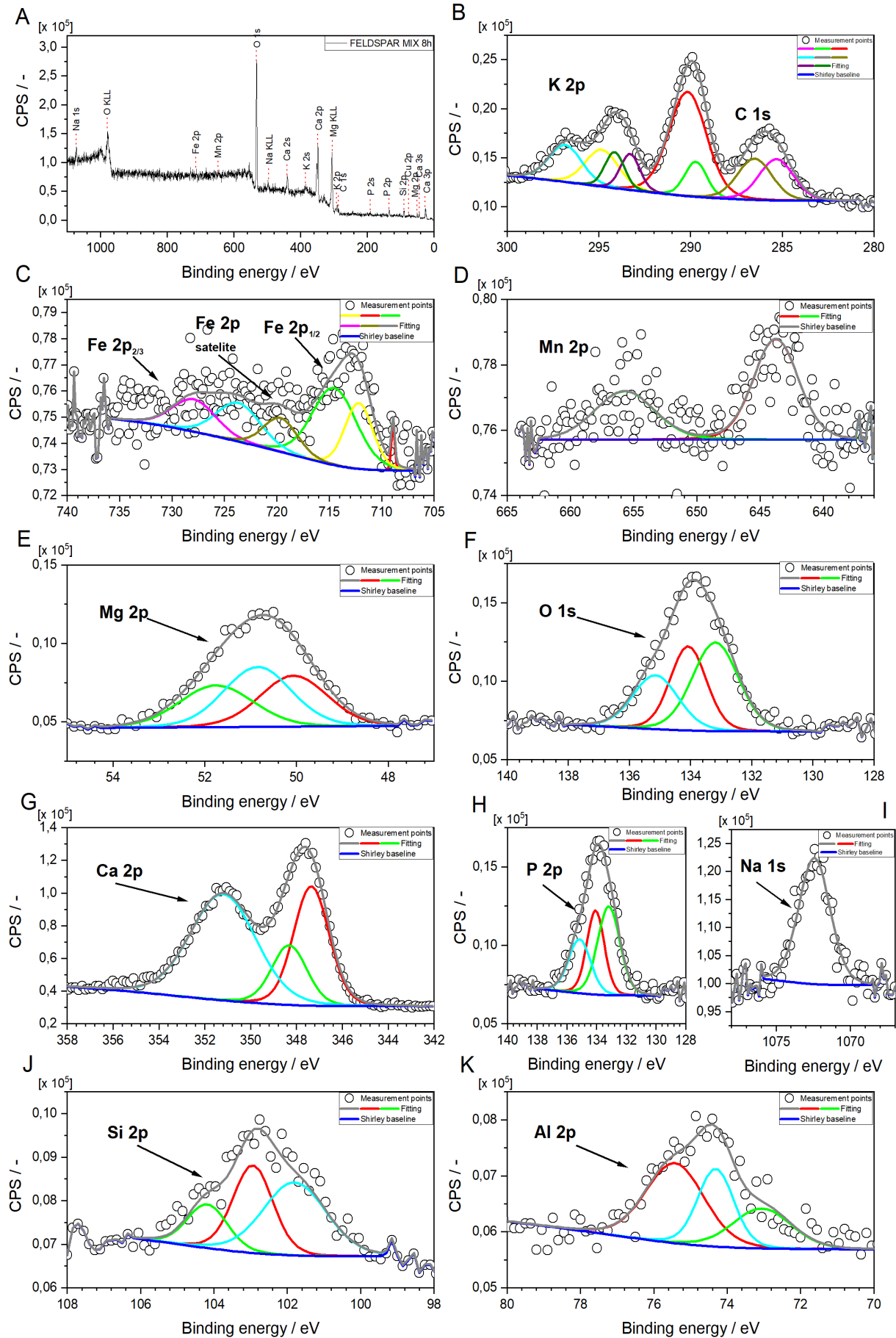


Figure 7.15: Feldspar Mix8h XPS high resolution spectra

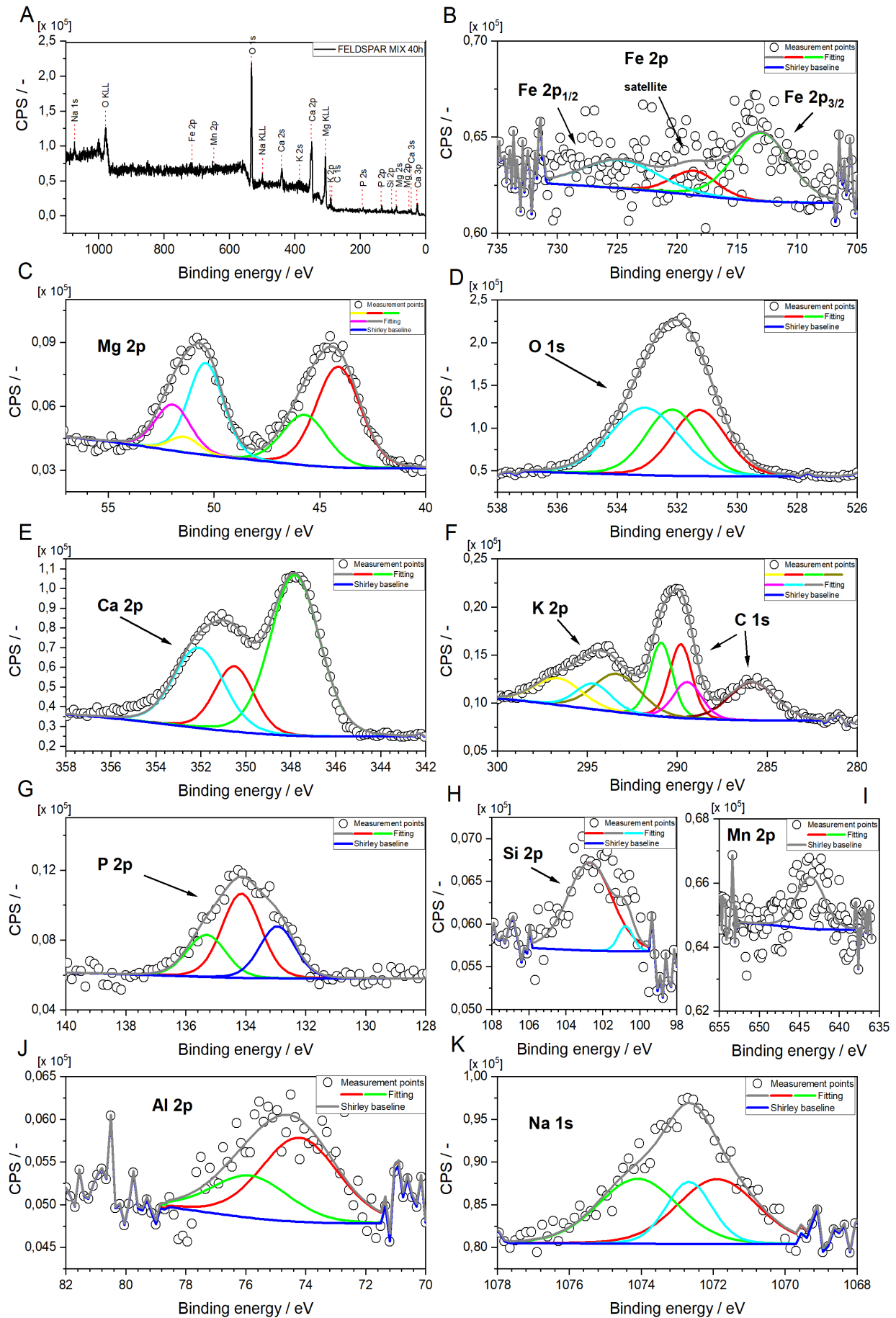


Figure 7.16: Feldspar Mix40h XPS high resolution spectra

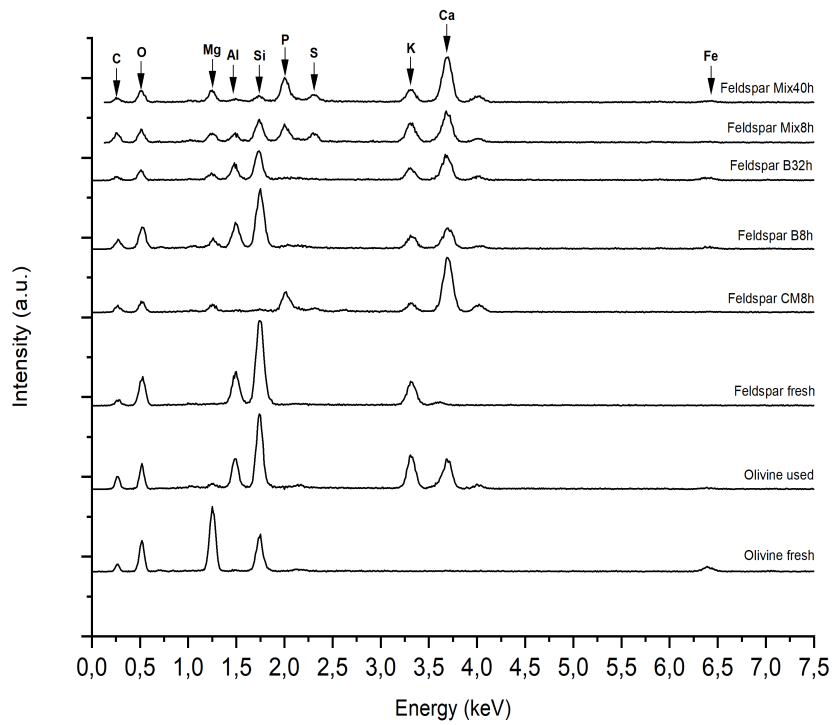


Figure 7.17: Collected EDX spectra

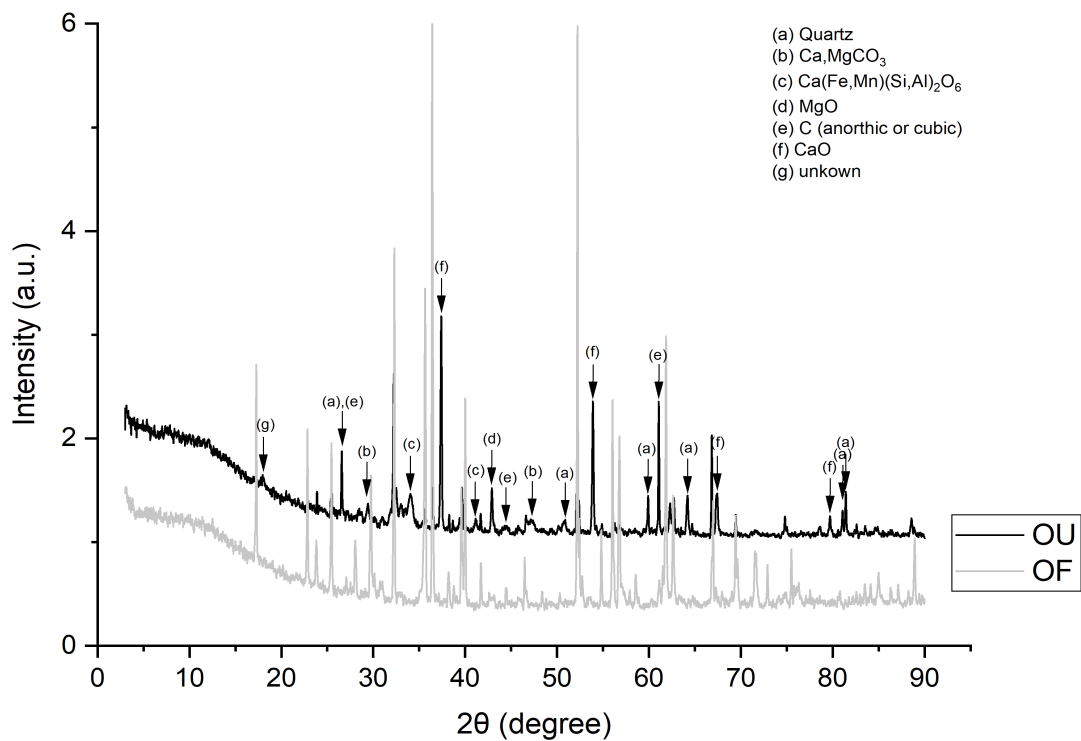


Figure 7.18: Olivine XRD spectra including allocated compounds

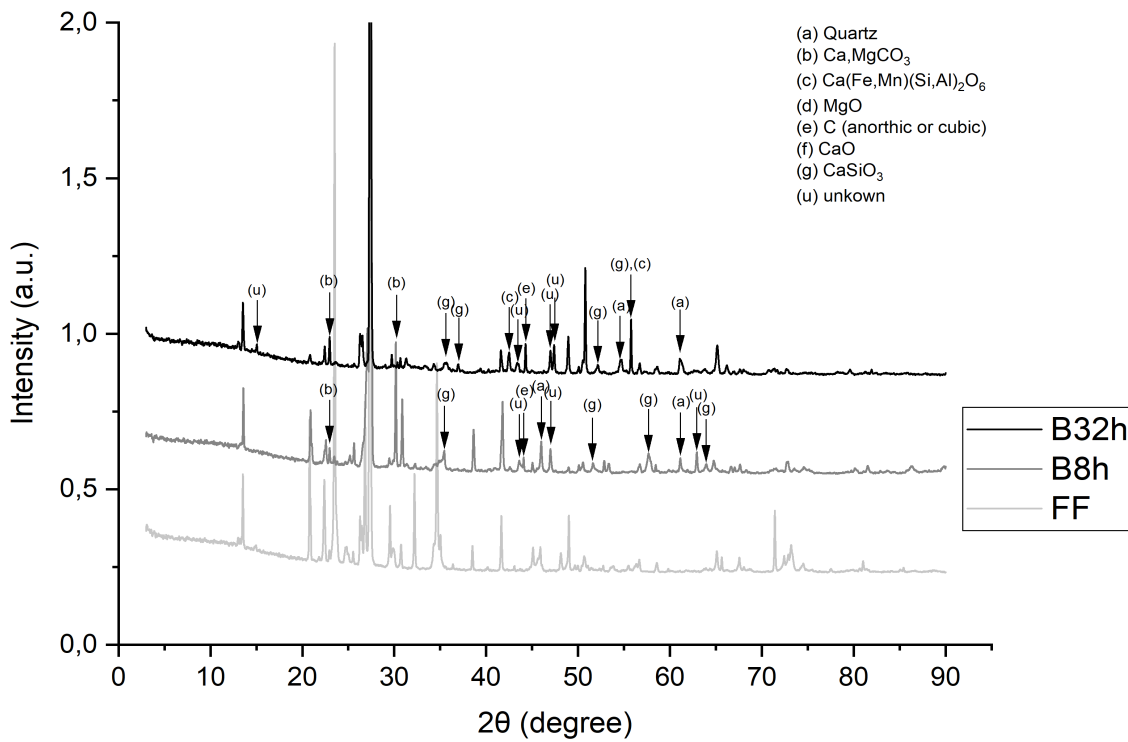


Figure 7.19: Feldspar bark XRD spectra including allocated compounds

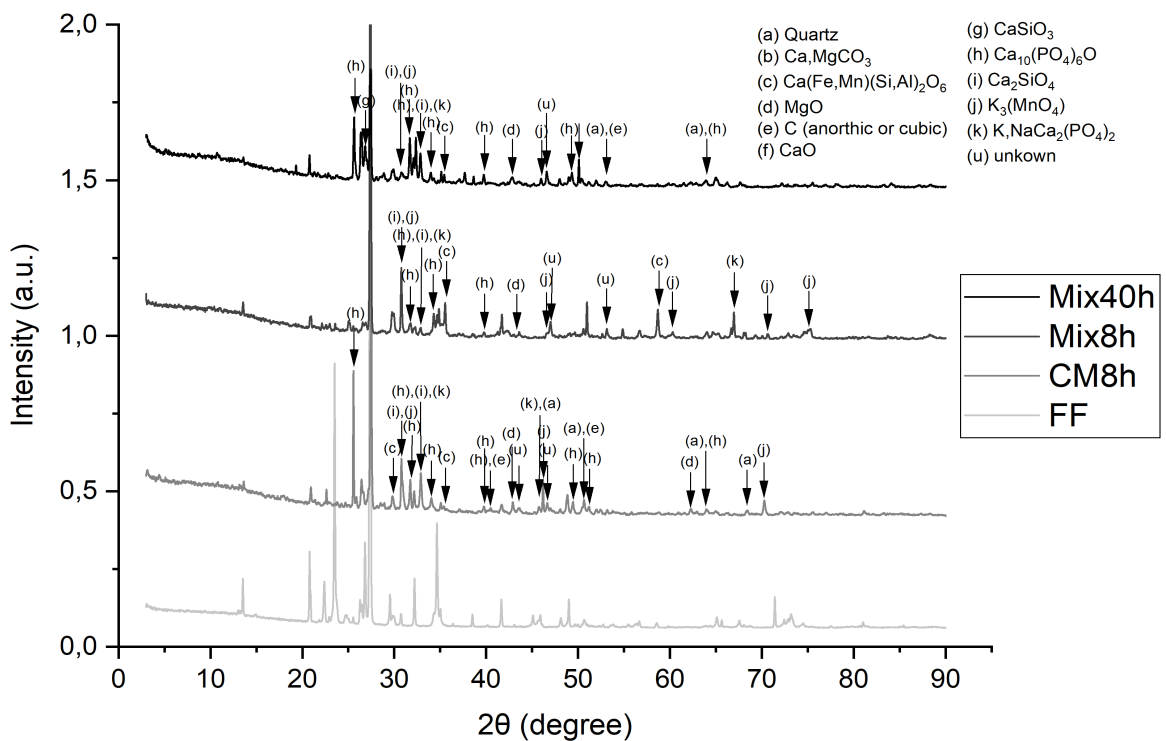


Figure 7.20: Feldspar chicken manure and mix XRD spectra including allocated compounds

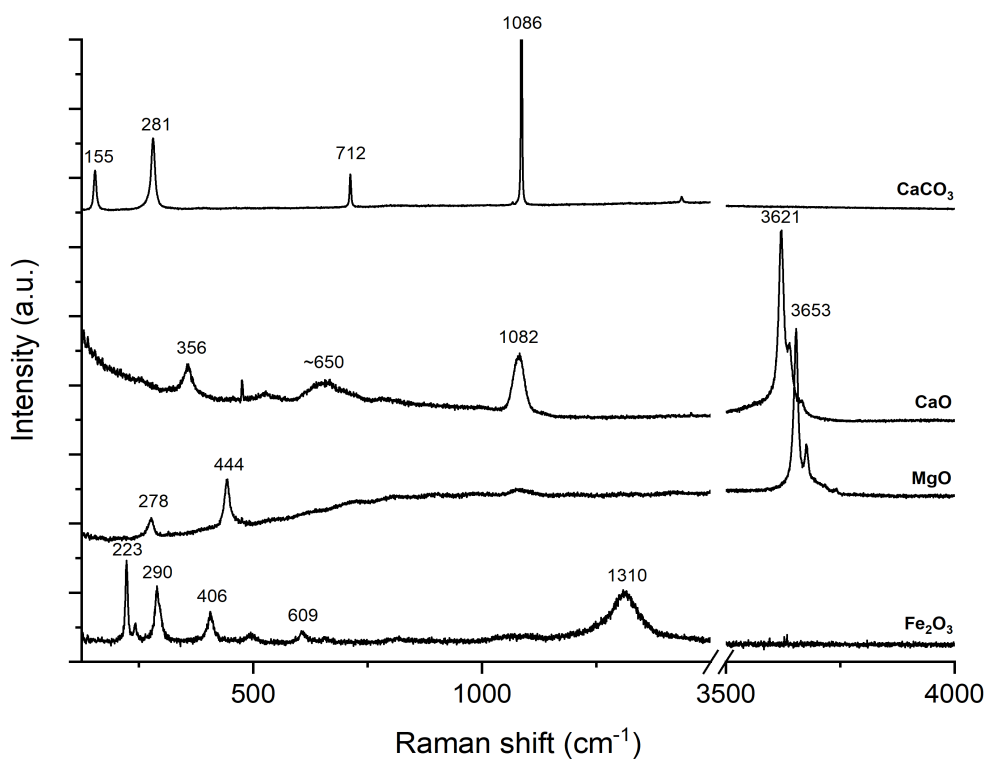


Figure 7.21: Raman spectra of measured reference compounds MgO , CaO and Fe_2O_3

Species	Structures
Bidentate carbonate	
Bidentate formate	
Monodentate carbonate	
Monodentate formate	

Figure 7.22: Structures of adsorbed Carbonate and Formate [20]